Vibration Analysis, Control and Optimal Placement of MFC Actuators and Sensors on Rotating Thin-Walled Composite Cantilever Beams

A Thesis Submitted in

Partial Fulfillment of the Requirements

for the Degree of

DOCTOR OF PHILOSOPHY

By

Vadiraja D N

(Roll No. 03610309)

DEPARTMENT OF MECHANICAL ENGINEERING

INDIAN INSTITUTE OF TECHNOLOGY GUWAHATI

August, 2008

Vibration Analysis, Control and Optimal Placement of MFC Actuators and Sensors on Rotating Thin-Walled Composite Cantilever Beams

A Thesis Submitted in

Partial Fulfillment of the Requirements

for the Degree of

DOCTOR OF PHILOSOPHY

By

Vadiraja D N

(Roll No. 03610309)

DEPARTMENT OF MECHANICAL ENGINEERING

INDIAN INSTITUTE OF TECHNOLOGY GUWAHATI

August, 2008

MECHANICAL ENGINEERING DEPARTMENT
INDIAN INSTITUTE OF TECHNOLOGY GUWAHATI
GUWAHATI-781039

CERTIFICATE

It is certified that the work contained in the Thesis entitled **"Vibration Analysis, Control and Optimal Placement of MFC Actuators and Sensors on Rotating Thin-Walled Composite Cantilever Beams"** submitted by **Mr. Vadiraja D. N.** to the Indian Institute of Technology Guwahati for the award of the degree of Doctor of Philosophy has been carried out under my supervision in the Department of Mechanical Engineering, Indian Institute of Technology Guwahati. This work has not been submitted elsewhere for the award of any other degree or diploma.

1st August 2008

(Prof. A. D. Sahasrabudhe)
Department of Mechanical Engineering,
Indian Institute of Technology Guwahati,
Guwahati – 781 039

Dedicated to
My father Nagaraja and mother Radha

ACKNOWLEDGEMENTS

The joy and satisfaction that accompany the successful completion of any task would be incomplete without mentioning those who made it possible.

I would like to express my sincere appreciation to ***Prof. A. D. Sahasrabudhe****, my advisor, mentor, and friend, who has been a role model to me for the last 4 years. His perpetual optimism is contagious, and he gave me the confidence to undertake and conquer the Ph.D. process. The persistent patience and friendliness in the moments of difficulties has always been remembered.*

I am also grateful to members of my doctoral committee, ***Prof. Debabrata Chakraborty, Prof. Rajiv Tiwari*** *and* ***Dr. H. B. Nemade,*** *all of whom have shown interest in this work and provided countless advice, insightful comments and discussion. I am equally thankful to my administrative guide* ***Prof. S. K. Kakoty*** *for his help during my research work at IIT Guwahati.*

I thank ***Prof. Uday Shankar Dixit,*** *Head, Dept of Mechanical Engineering for extending all the help during the research work.*

With immense pleasure, I express special thanks to ***Prof. Naresh K. Chandiramani,*** *Associate Professor, Indian Institute of Technology, Bombay, who is probably the best teacher I have had as a doctoral student. He has the ability to present complicated topics in a clear, straightforward manner which I found best suits to my learning style.*

The financial support for this research, which is provided by the Department of Mechanical Engineering, Indian Institute of Technology Guwahati, is gratefully acknowledged.

The most important support for this work came from my parents, ***Shri. Nagaraja Deshpande*** *and* ***Sou. K.V.Radha,*** *for encouraging me to go further. I would like to thank my parents for all of their love and support through the years, especially at peak of the economy encouraged me to pursue Ph.D on a modest stipend. I wish to thank my wife,* ***Sowmya****, for her patience and help during the years. I would like to thanks* ***Prof. Jois*** *and* ***Mrs. Jois, Mrs. Sahasrabudhe, Prof. Pradeep Yammiyavar*** *and* ***Mrs. Yammiyavar*** *other family friends for their support during my stay in IIT Guwahati.*

Last but certainly not least, I would like to express my wholehearted gratitude to ***Prashant Gudur, Krishna Kumar Singh, Aditya Singh Bhaduria and Sachin Kumar Singh,*** *classmates and every individual who are associated with Ph.D course for their support during my work.*

Above all, I am thankful to the almighty.

ABSTRACT

In the present thesis, equations of motion are derived using dynamic modelling method for rotating thin-walled composite beams. Coupled equations of motion are derived for arbitrary beam configuration using Hamilton's principle for higher order shear deformable beam. A non-Cartesian deformation variable representing axial stretch, along with two Cartesian variables representing bending motions are used. Due to this transformation, centrifugal stiffening and gyroscopic coupling effects can be captured in linear potential and kinetic energy equations. This makes the formulation less cumbersome compared to geometrically nonlinear modelling method. Moreover, this method provides the advantage of inclusion of gyroscopic coupling. The effect of gyroscopic coupling makes the structural model more realistic and it has been demonstrated that the gyroscopic coupling cannot be neglected. The mathematical model also includes non-classical effects generally exhibited by rotating composite beams such as anisotropy, heterogeneity, warping and transverse shear. The approximate solutions of equations of motion are obtained using the extended Galerkin's method. To validate the developed code, the results from the present method are compared with the experimental and theoretical results available in the literature. The predicted results are in good agreement with the results available in the literature. Numerical solutions for rotating composite cantilever beams are illustrated for a composite box beam configuration. Effects of taper, pretwist, presetting and gyroscopic coupling on free and forced vibration of rotating beams are studied. Numerical results reveal that gyroscopic coupling between lagging-extension modes has considerable effect on the system natural frequency, mode shape, forced response and hence cannot be neglected.

The structural modelling of rotating composite thin walled beams is extended to include embedded MFC actuators and sensors. The actuators and sensors are considered as distributed over the top and bottom surface of the beam, respectively. The governing coupled equations of motion are derived from the Hamilton's principle and approximate solution is obtained using extended Galerkin's method.

The reduced order model is formulated with the assumption that the lower order modes have lower energy associated and consequently are the most easily excitable ones. The number of modes in a reduced order model are selected by analyzing convergence of tip displacement and actuator voltage. Thereafter the reduced order model is converted to a state space form for the purpose of controller design. Optimal control algorithms such as linear quadratic regulator (LQR) and linear quadratic Gaussian (LQG) are used to estimate feedback gain. Comparison between bending vibration control performance of monolithic piezoelectric and fibre based piezoelectric actuators/sensors are studied. Distributed piezoelectric model available in the literature is used for monolithic piezoelectric actuators and sensors. It is observed that control effort by using MFC actuators and sensors is significantly less compared to that of monolithic piezoelectric actuators and sensors. Passive effect of monolithic and fibre based piezoelectric actuators on system natural frequencies are studied in numerical experiments. Optimal control performance of monolithic and fibre based piezoelectric actuators and sensors on rotating beams is investigated. Performance of MFC actuators for bending vibration suppression of rotating beams for various pretwist, taper and presetting angles is investigated.

Optimal locations of MFC sensors and actuators are achieved by minimizing the trace identity of filter Riccati and algebraic Riccati equations, respectively. Positions of actuators and sensors are optimized using genetic algorithm. Converged locations of sensors and actuators from genetic algorithm are set as initial conditions for solving by sequential quadratic programming method. Importance of placement of sensors and actuators on tip displacement and control effort is highlighted. It is observed that, poles of correctly placed sensors and actuators shift deep inside the left half plane. Settling time, tip displacement and control effort are found to reduce by optimal locations of sensors and actuators. Variation of optimal location of sensors and actuators with respect to ply angle orientation, rotational speed, pretwist angle and taper parameters is studied. It is found that, with the increase in rotational speed, optimal location of sensors and actuators shifts towards the root.

CONTENTS

List of Figures

List of Tables

Nomenclature

a_{ij}	Stiffness coefficients characterizing symmetric (7 X 7) matrix of the anisotropic composite beam
$\tilde{a}_i$	Stiffness coefficients arising due to higher shear deformable beam model
$\tilde{a}_i^p$	Global 1-D stiffness coefficients for a piezoelectric material
br, bt	Breadth at root and tip of the beam respectively (Eq. 2.39)
C	Elastic constant of piezoelectric material
C_d	Modal damping matrix
$cr,\ ct$	Chord at root and tip of the beam respectively (Eq. 2.39)
D	Electric displacement
d	Piezoelectric strain constant (Eq. 4.9)
E	Electric field
e	Piezoelectric constant
$\bar{e}_{ij}$	Transformed reduced piezoelectric constant
h	Wall thickness
I_i	Inertial quantities
$i(t)$	Current on the surface of a sensor
$K = R^{-1}B^{\mathrm{T}}P$	LQR gain (Eq. 5.10)
L	Length of the beam (Figure 2.1)
$L = SC^{\mathrm{T}}V^{-1}$	Kalman gain (Eq. 5.20)
$\bar{Q}_{ij}$	Transformed reduced stiffness coefficients
q_i	Generalized coordinates
$q_s(t)$	Total charge on the sensor surface
R_{o}	Hub radius (Figure 2.1)
$R(z)$	Geometric quantity (Eq. 2.22)
(s, n, z)	Local coordinates for the cross section (Figure 2.1)

$\hat{s}$	Axial stretch deformation variable
T	Kinetic energy (Eq. 2.16)
(u_0, v_0, w_0)	Rigid body translations in x, y, z axes, respectively
$u(t)$	Optimal control
V	Potential energy (Eq. 2.15)
W	Work done by external forces (Eq. 4.16)
X	State vector
(X, Y, Z)	Cartesian inertial frame (Figure 2.1)
(x, y, z)	Beam coordinate system (Figure 2.1)
(x^p, y^p, z^p)	Local beam coordinate system (Figure 2.2)

Greek

$\beta(z)$	Pretwist angle (Figure 2.2)
η	Taper parameter (Eq. 2.39)
Ω	Rotational speed
$(\theta_x, \theta_y, \phi)$	Rotation of the cross section along x, y, z axes, respectively
σ_{ij}	Stress components
ε_{ij}	Strain components
$\in$	Permittivity coefficient
θ	Ply angle orientation (Figure 2.1)
$\bar{\in}_{ij}$	Transformed reduced permittivity coefficient
φ_i	Trial functions
ξ_i	Modal damping ratio
δ	Variational operator
ω_i	Natural frequency of i^{th} mode
$\oint$, $\int_0^L$	Integral along the cross section and the span, respectively

Superscripts

u_o^T	Transpose of the matrix or vector u_o
$\ddot{u}_o$	$\frac{\partial^2 u_o}{\partial t^2}$
(u_o', u_o'')	$\left(\frac{\partial u_o}{\partial y}, \frac{\partial^2 u_o}{\partial y^2}\right)$

Abbreviations

AFC	Active fiber composites
GA	Genetic algorithm
HSDT	Higher shear deformation theory
LQG	Linear quadratic Gaussian
LQR	Linear quadratic regulator
MFC	Macro fiber composites
PVDF	Poly vinylidene fluoride
PZT	Lead zirconate titanate
SQP	Sequential quadratic programming

Chapter 1

Introduction and literature review

1.1 Introduction

Rotating blades are flexible structures that have practical applications in turbo machines, helicopter blades, robot manipulators, compressor blades, windmill turbine blades, spinning space structures, propeller blades and henceforth. These engineering structures can be idealized as rotating cantilever beams. The need for weight reduction is of prime concern in the design of complex aerospace structures. In the recent past, use of thin walled composite materials in the aerospace structures has increased to a large extent. The thin walled composite materials offer many advantages. Among them, substantial reduction in weight, increased load carrying capacities, superior fatigue characteristics and facilitate structural tailoring by changing fibre angle orientation to alter system responses. They also facilitate improved performance at higher loads and at higher temperatures from the design point of view.

Vibration of rotating beams results from various sources, such as impact, unbalance, eccentricity in assembly and forces transmitted from the rotor. Vibration in these structures results in crew and passenger discomfort and/or catastrophic failure. However, it is not possible to eliminate the causes of vibration altogether. Hence, the vibration characteristics of these structures need to be identified accurately so that one can properly design or control the system to minimize the effect of vibration. The vibration characteristics of rotating beams differ from that of non-rotating beams in terms of gyroscopic coupling, centrifugal force and centrifugal stiffening. On a beam, Coriolis forces appear whenever there is a radial lengthening or shortening of the beam about the rotational axis as a result of beam

extension. Centrifugal stiffening increases the system natural frequencies and varies the mode shape with the increase in beam rotational speed.

Vibrations can be reduced by a number of methods such as reduction of vibration at source, properly designing the system to have operating speed away from the system natural frequency, including passive damping elements, or by including smart materials in the system. At all the times, it is not possible to reduce vibration by the first two methods mentioned above. The inclusion of passive damping material increases the weight of the system, which is not desirable. In recent years, active vibration control using smart structures such as piezoelectric materials is being extensively used for vibration suppression of flexible structures. In active vibration control, the piezoelectric materials embedded on the surface of the host structure act as sensors and actuators. Piezoelectric sensors measure displacements or velocities in the form of electric charge. Actuating voltage is applied to the actuator which is proportional to the measured electric charge. This applied voltage on the actuators induces force on the host structure. Usually, embedded piezoelectric sensors and actuators are distributed over the surface of the beam. The actuators and sensors positioned near the nodal points of the modes lead to increase in the control effort. Hence, piezoelectric sensors and actuators need to be placed properly to ensure the optimal effectiveness of the control.

1.2 Literature review

The experimental investigation and mathematical modeling in the field of vibration and control is several decades old. In the following three sub-sections, a brief literature survey is presented. In the first section, the research carried out by various researchers and academicians on vibration analysis in the field of composite materials, thin-walled beams and rotating beams is presented. Second section comprises of literature on vibration suppression utilizing piezoelectric sensors and actuators. The last section presents a review on optimal placement of sensors and actuators.

1.2.1 Vibration analysis of rotating beams

Rosen (1991) has carried out an excellent literature review on structural and vibration behavior of pretwisted beams. The review addresses the static, dynamic and stability aspects of pretwisted beams. It also deals with different types of mathematical models, their analysis and approximate solution methods. Bielawa (1992) presented a review of several solution techniques applied to bending vibration of rotating beams. Different approximate methods such as the Galerkin's method, Rayleigh Ritz method, finite element method and henceforth are studied in his review.

1.2.1.1 Rotating untwisted beams

Hodges and Rutkowski (1981) presented a variable order finite element formulation for rotating non-uniform beams. McGee (1987) discussed applications of the finite element technique to rotating blade structures. He has presented a finite element formulation to approximate the static and dynamic behaviour of flexible, rotating blades and effects of centrifugal stiffening and softening forces are demonstrated in his analysis. Yokoyama (1988) derived finite element formulation for rotating Timoshenko beams and analyzed in-plane and out of plane free vibration characteristics. The author included the effects of hub radius, setting angle, shear deformation and rotary inertia on bending frequencies of a rotating beam in his analysis. Further, the author noticed that the effect of shear deformation on the natural frequencies is generally more pronounced than that of rotary inertia for non-rotating beams; whereas in rotating beams due to the presence of centrifugal stiffening effect, increase in rotational speed increases the effect of rotary inertia.

1.2.1.2 Pretwisted beams

Carnegie and Thomas (1972) examined the effect of shear deformation and rotary inertia on the lateral frequencies of pretwisted and non-uniform cantilever beams. They used the Galerkin's method to determine the natural frequencies. Swaminathan and Rao (1977) derived equations for rotating pretwisted and tapered cantilever beams with rectangular cross-section. They derived the equations using Lagrangian functions and obtained approximate solutions using Ritz method. They

noticed that pretwist, rotation and taper are having considerable influence on the flexural frequencies of rotating beams.

Subrahmanyam (1982) presented coupled bending-bending vibrations of pretwisted rotating beams using Reissner method. The effect of breadth taper, depth taper shear deflection and rotary inertia on vibration characteristics are discussed in his analysis. It was extended by Subrahmanyam and Kaza (1985) to include the effects of warping, pretwist, tension-torsion coupling and tennis racket in rotating pretwisted beams. The relative importance of these terms is pointed out in their analysis. The authors used finite difference procedure with first order central differences and observed that accurate lower bound solutions can be obtained by the finite difference method.

Sabuncu (1985) presented a finite element model for the coupled vibration analysis of rotating pretwisted blades with cubic polynomial approximation of the displacements. He illustrated that small number of elements are sufficient for convergence of natural frequencies and mode shapes. The analysis was extended to linear and non-linear variation of pretwist angle along the beam length. Rao and Gupta (1987) studied free vibration characteristics of rotating pretwisted blades using classical bending theory of thin shells. Their study included the effect of pretwist, aspect ratio, rotational speed, hub radius and stagger angle on rotating beam free vibration characteristics of rotating beams. Kar and Neogy (1989) derived the coupled equations of motion for small flexural deformations of a uniformly rotating, linearly pre-twisted and tapered cantilever beam. They investigated the effects of tangency coefficient, thermal gradient, rotational speed, tip mass and pre-twist on the stability of a cantilever beam.

1.2.1.3 Thin – walled composite beams

Stemple and Lee (1988) developed a refined finite element model for thin walled composite beams including the effect of non-uniformity and twist. They presented a model for arbitrary cross-section capable of handling the combined bending, torsional and extensional behavior of the composite thin-walled beams.

They used a shear flexible beam element with warping displacements parallel to the deformed beam axis superimposed over the cross-section.

Rehfield *et al.* (1990) reported the non-classical effects such as elastic bending, shear coupling and restrained torsional warping in the behavior of thin-walled composite beams. They found that bending – shear coupling is important in the analysis of composite beams. It is found from their analysis that the results obtained by ignoring this coupling results in wrong estimation of lateral deflections. They concluded that transverse shear must be included in the kinematics so that its coupling with bending gets incorporated in the elastic constants. They have also shown that torsional warping rigidity is important for closed cross-section thin walled composite beams.

Chandra *et al.* (1990) experimentally investigated the effect of bending, torsion and extensional loads on thin-walled composite beams. They have correlated the experimental results with the available predicted values from the finite element method. Chandra and Chopra (1992) have theoretically and experimentally investigated vibration characteristics of thin-walled composite box beams and coupled composite I-beams with bending-twist and extension-twist coupling under rotating conditions. Smith and Chopra (1993) studied the aeroelastic response, loads and stability of a composite thin-walled beam.

Wu and Sun (1992) presented the governing dynamic equations of motion for composite thin-walled beams. The system of equations consist of four coupled ordinary differential equations which govern the shear deformation of the middle surface and can be applied for either open or closed cross-section.

Du *et al.* (1994) researched on developing analytical solutions for rotating Timoshenko beam. Their model included the effects of rotary inertia and shear deformation. They presented a power series solution for rotating beams. Lee and Lin (1994) studied bending vibrations of rotating tapered Timoshenko beams with elastically restrained root by neglecting Coriolis coupling. They have shown the

influence of coupling effect of rotating speed, inertia, setting angle and taper ratio on the natural frequencies in their study.

Higher order shear deformation theory (HSDT) for thin-walled composite beams was presented by Suresh and Nagaraj (1996). The method is applicable to both open and closed cross-section beams. Warping is considered in the mathematical model. They have discussed the importance of higher order theory vis-a-vis other theoretical methods. They have shown that, HSDT is required for obtaining good correlation for stresses. The importance of warping on vibration characteristics of thin-walled composite beams is highlighted in their study.

Ekel'chik and Ryabov (1996) analyzed free vibration studies of rectangular composite cantilever plates based on classical lamination theory. Harmonic response of tapered composite beams was examined using the finite element analysis based higher order shear deformation theory by Rao and Ganesan (1997). They included the effects of in-plane inertia and rotary inertia in their model. Influence of taper parameter and taper profile was discussed in the numerical examples. The review comprising modeling of thin and thick walled rotating composite beams was presented by Jung *et al.* (1999). They highlighted the influence of in-plane warping, out of plane warping, non-uniformity, large deformations, transverse shear and aeroelastic stability in their study.

A finite element model for free vibration analysis of composite beams based on higher order beam theory was presented by Shi and Lam (1999). They noticed that the higher order theory has significant influence on flexural vibration. Alkahe and Rand (2000) studied the effect of beamwise bending-twist coupling and chordwise bending-twist coupling on composite blades. Yildirim and Kiral (2000) applied transfer matrix method to study the effects of rotary inertia and shear deformation on the out-of-plane bending and torsional natural frequencies of composite beams.

A rotating composite beam formulation based on mixed variational approach was developed by Jung *et al.* (2001). They considered the effects of elastic coupling, shell-wall thickness, warping and transverse shear deformations in their model. The influence of wall thickness and transverse shear on the free vibration characteristics of composite beams with either bending-torsion or extension-torsion coupling were also investigated in their study. Li *et al.* (2004) presented dynamic response of axially loaded Timoshenko thin-walled beam with bending-torsion coupling. They studied the effects of bending-torsion coupling, axial force, shear deformation and rotary inertia on the dynamic behavior of thin walled composite beam. Cai *et al.* (2005) investigated the accuracy problem of traditional method by considering the second order coupling quantity of the axial displacement caused by transverse displacement of the beam. They derived equations of motion in the inertial and non-inertial frames.

A finite element formulation for thin walled composite beam with first order shear deformation that is free from shear locking was presented by Chakraborty *et al.* (2002), Mitra *et al.* (2004a) and Mitra and Gopalakrishnan (2006). The developed super convergent finite element has a static stiffness matrix that is obtained by exactly solving the axial-flexural-shear coupled equations. This beam element has super convergent property and was used for wave propagation analysis. Vinod *et al.* (2006; 2007) presented a spectral finite element analysis of rotating isotropic Euler-Bernoulli beam. Ganesan and Zabihollah (2007) presented a higher order tapered composite beam finite element formulation.

Song and Librescu (1997) studied free vibration characteristics of rotating thin walled composite blades with closed cross-section. The non-classical effects, generally exhibited by rotating thin-walled composite beams such as anisotropy, heterogeneity, transverse shear, warping and centrifugal effects were considered in their model. A procedure to include tennis-racket effect in rotating beams was suggested in their work. The effect of fiber orientation on free vibration characteristics of rotating composite beam for a box cross-section was presented in their work. It was extended by Song *et al.* (2001) to study the vibration

characteristics of pretwisted rotating thin-walled composite rotating beams. Song *et al.* (2000) studied the vibration and stability of pretwisted spinning composite beams. Effects of taper on vibration and stability of spinning composite beams was studied by Na *et al.* (2006). Song *et al.* (2001) extended the model to spinning composite thin–walled beams with tip rotor. The combined effect of gyroscopic coupling of tip rotor and conservative force on free vibration and stability were investigated in their study. Effects of pretwist and presetting on bending vibration of rotating composite beams were studied by Oh *et al.* (2003). Chandiramani *et al.* (2002) presented the higher shear deformation theory model for rotating composite thin-walled beams. Centrifugal and gyroscopic couplings were considered in the mathematical model. However, the model derived was non-linear in nature. Linearization was possible only after discarding the gyroscopic coupling. Hence, in the vibration studies, they neglected the gyroscopic coupling effects. The study was extended to pretwisted rotating composite blades by Chandiramani *et al.* (2003).

1.2.1.4 Gyroscopic coupling

Several authors have illustrated the effect of gyroscopic coupling in rotating blades. Kane *et al.* (1987) investigated a flexible cantilever beam performing rotation and translation motion. The model developed by them automatically accommodates the effects such as centrifugal stiffening and gyroscopic coupling. In the discussion they highlighted that traditional Cartesian coordinate model fails to describe the dynamic behavior of the beam when beam undergoes large overall motion. Kar and Sujata (1992) presented the parametric instability of a rotating, pretwisted and preconed cantilever beam under a pulsating axial excitation including the effects of Coriolis force and setting angle. The static buckling loads as well as the instability regions of simple and combination resonance, and those of rotational speed, thickness ratio and Coriolis force on the resonance zones were emphasized. Brons *et al.* (1996) studied the influence of gyroscopic coupling on a rotating elastic structure with a mass at the free end using Poincare-Lindstedt series. A dynamic finite element vibration analysis of rotating assemblages composed of beams with gyroscopic coupling was presented by Hashemi and Richard (2001). The influence of gyroscopic coupling on natural frequencies of cantilever rotating beams was

demonstrated in their numerical results. Chen and Kareem (2003) studied the curve veering of cable stayed and suspension bridge. Vidoli and Vestroni (2005) studied dynamical implications of the veering between two eigenvalue curves considering elastic, inertial and gyroscopic coupling in a two-degree of freedom system. In the analytical study, veering regions were measured. Veering phenomena are interesting since they involve relevant energetic exchanges between the eigen modes and strongly affect the undamped forced response of the system. Yoo *et al.* (1995) showed that for rotating beams the gyroscopic coupling between stretching and bending modes results in veering of eigen root loci.

Yoo *et al.* (1995) used dynamic modeling method to study the vibration characteristics of rotating beams. Dynamic modeling method employs a non-Cartesian variable along with two Cartesian variables to describe the deformations. This method automatically accommodates for the gyroscopic coupling and centrifugal stiffening. They showed that this transformation is equivalent to considering von Kármán strain measures for the beam. They obtained approximate solutions using Rayleigh-Ritz method. In the numerical analysis, they considered the effect of gyroscopic coupling, observed eigen value loci veering and abrupt mode shape variation in the veering region. The hybrid set of deformation variables considered in dynamic modeling method consist of arc length stretch, flapwise deformation and lagwise deformation. Yoo *et al.* (2001b) extended dynamic modeling method to include pretwist in rotating beams. Vibration analysis of rotating pretwisted beams with concentrated tip mass was presented by Yoo *et al.* (2001a). Chung and Yoo (2002) developed finite element formulation for the rotating beam using dynamic modeling method. Recently, flapwise bending free vibration studies of composite cantilever beam using dynamic modeling was presented by Yoo *et al.* (2005).

1.2.2 Active vibration control

Piezoelectric effect was discovered by the French mineralogist Rene Just Hauy in 1817. It is described by the presence of electric charges on the surface of a

stressed tourmaline crystal. Piezoelectric effect was first demonstrated experimentally by Pierre and Jacques Curie in 1881. The direct piezoelectric effect consists of the ability of certain crystalline materials (i.e. ceramics) to generate an electrical charge in proportion to an externally applied force. The direct piezoelectric effect has been widely used in the transducer design. According to the inverse piezoelectric effect, an electric field induces a deformation in the piezoelectric material. The inverse piezoelectric effect has been applied in the actuator design. The piezoelectric materials can be used as actuators as well as sensors. In the past three decades, a lot of research has been carried out for vibration suppression. In recent years, piezoelectric material is being extensively used for vibration suppression of flexible structures. In the following sections summary of literature in the area of vibration suppression is presented.

1.2.2.1 Monolithic piezoelectric materials

Several researchers and academicians including Reddy (1999), Rao and Sunar (1999), Benjeddou (2000) have carried out critical reviews with a focus on smart structures and piezoelectric control actuation. A recent detailed paper by Reddy (1999) gives a brief review of smart structural systems and also deals with the theoretical formulations. It describes the Navier solutions and finite element models based on the classical first order and third order theory, accounting for the stiffness of the actuator and sensor layers, electro-thermo-mechanical coupling, time dependency and the von Kármán geometric nonlinearities.

Bailey and Hubbard (1985) demonstrated vibration suppression of cantilever beam using distributed piezoelectric polymer actuators. Baz and Poh(1988) demonstrated piezoelectric actuation in controlling the structural vibrations of flexible beams. In their study a modified independent modal space method is used to select optimal location, control gain and excitation voltage of the piezoelectric actuators. Choi (1994) utilized piezofilm actuator and sensor to control the static and elastodynamic responses in flexible beam. Denoyer and Kawk (1996) carried out experiments to demonstrate vibration suppression of a slewing structure using piezoelectric sensors and actuators. They have also developed an approximate

analytical model of slewing flexible body with surface bonded piezoelectric sensors and actuators in their work. Bai and Lin (1996) proposed LQG algorithm for suppressing the small amplitude random vibrations in flexible beams using PZT actuator and PVDF sensor.

Lam *et al.* (1997) presented a finite element model for piezoelectric composite laminates based on classical lamination plate theory to control a composite plate. The formulation is derived from the variational principle and passive effects of embedded sensors and actuators are taken into account. Ray (1998) proposed output feedback optimal control algorithm to suppress the vibration of simply supported symmetric thin laminated plate integrated with piezoelectric layers. Na and Librescu (2000) presented an optimal LQR algorithm to control the vibration of thin walled anisotropic cantilever beams exposed to blast loadings. It was extended by Librescu and Na (2001) to active vibration control of doubly tapered thin walled beams using embedded piezoelectric actuators and sensors. Trindade *et al.* (2001) studied active and passive vibration control of damped sandwich beams using piezoelectric actuators. They considered an additional electrical degree of freedom to account for direct and converse effect of piezoelectric sensors and actuators. The active control was achieved using LQR, LQG and derivative control algorithms.

Ang *et al.* (2002) studied the selection of weighting matrices in LQR control algorithm. They proposed the use of total weighted energy method to select the weighting matrices and demonstrated the control performance by selecting various weighting matrices. Wang and Huang (2002) studied vibration control of flexible beam by using feed forward and feed back control loops. They constructed disturbance force observer to observe the disturbance modal forces. Finite element modeling of flexible structures with distributed sensors and actuators was presented by Narayanan and Balamurugan (2003). They considered beam, plate and shell structures in their finite element model. Na *et al.* (2003) presented the structural model of tapered rotating blades with embedded sensors and actuators. Lee *et al.* (2004) studied transient response of laminated composite plates with embedded

distributed piezoelectric sensors and actuators. They used third order plate theory. The transient vibration control was achieved by using velocity feedback control algorithm. Vibration control of thin walled beam using acceleration feedback was presented by Mitra, Gopalakrishnan and Bhat (2004b). Bending vibration control of a rotating beam attached to a rigid hub is studied by Yang *et al.* (2004). To simplify the model, they neglected axial stretch motion in the model. Positive feedback and momentum exchange feed back control laws were used in suppression of rotating beam. Hwu *et al.* (2004) studied forced vibration suppression of composite sandwich beams with embedded piezoelectric sensors and actuators using an observer state feedback control. Karagulle *et al.* (2004) demonstrated that ANSYS /Multiphysics capabilities can be used to study the vibration control of a circular disc. Librescu and Na (2005) presented the vibration control methodologies for thin-walled composite beams using distributed piezoactuators. Na *et al.* (2005) extended the work of Librescu and Na (2005) to rotating composite cantilever beams. Chandiramani *et al.* (2004a; 2004b) studied the vibration control of rotating composite cantilever beams with embedded PZT sensors and actuators. They designed the controller based on LQR control algorithm. It was extended by Shete *et al.* (2007) for pretwisted higher shear deformable rotating composite thin-walled beams. Hu and Ma (2005) studied vibration suppression of flexible spacecraft in the presence of disturbances. Vasques and Rodrigues (2006) investigated the effectiveness of performance of different control strategies in smart active piezoelectric beam.

1.2.2.2 Macro fiber composites (MFC)

In all the above work, researchers considered monolithic piezoelectric sensors and actuators. Conventional monolithic piezoelectric materials such as PZT, PVDF and piezoceramic patches used for vibration suppression are brittle in nature. Recently, interest of researchers has shifted to piezoelectric fiber based sensors and actuators. Different kinds of piezoelectric fiber composites developed in recent years are active fiber composites (AFC), macro fiber composites (MFC) [Wilkie and Park (1996), Wilkie *et al.* (1996)] and piezoelectric fiber reinforced composite (PFRC)

[Mallik and Ray (2004)]. MFC sensors and actuators have numerous advantages.Two of the most important advantages are

(1) MFCs conform to curved surfaces.

(2) Piezoelectric strain constant is high.

Active fiber composite actuator, developed by MIT [Hagood and Bent (1993); Bent *et al.* (1995), Bent (1997)] uses circular cross-section piezoceramic fiber in epoxy matrix; whereas, MFC actuators developed by NASA Langley Center [Wilkie and Park (1996), Wilkie *et al.* (1996), Jha (2002)] uses rectangular cross-section piezofilm fibers in epoxy matrix. The research activities on the analytical modeling of AFC/MFC actuation have been very limited.

Wilkie *et al.* (1996) applied directional properties of the composite actuator for the twist control of a helicopter rotor blade. MFC sensors and actuators with numerous advantages over monolithic piezoelectric materials are discussed by Park and Kim (2004) in detail. They extended their work to study the behavior of composite panel vibration suppression with embedded AFC and MFC actuators [Park and Kim (2005)]. Henry *et al.* (2004) experimentally investigated the performance of MFC for sensing applications in inflated torus. Cesnik and Morales (2001) used AFC actuators to control the vibrations of pretwisted and curved composite beams. Azzouz *et al.* (2001) studied performance of MFC actuators for active vibration and acoustic control. Nguyen and Kornmann (2006) experimentally compared the actuation performance of MFC and monolithic PZT patches. Their analysis shows that the MFC actuators have a direction free strain twice as high as PZT patches. Brockmann and Lammering (2006) formulated beam element for rotating thin walled composite beams and studied vibration characteristics. Choi *et al.* (2006 and 2007) modelled first order shear deformation theory of rotating thin walled beams using MFC actuators and monolithic piezoelectric sensors. In their study, the negative velocity feedback control algorithm is used to suppress the vibration. They carried out analysis of damping performance by placing sensors and actuators on inner, central and outer surface of the box beam.

1.2.3 Optimal placement of actuators and sensors

Yang and Lee (1993) presented a model for simultaneous optimization of sensor/actuator placement and feed back control gain for systems with collocated sensor/actuator. Their results show that in active control, the optimal sensor/actuator location is not at the root of a cantilever beam. Lammering *et al.* (1994) studied the piezoelectric actuator placement in truss structure. Lee *et al.* (1996) proposed a method which allows integrated determination of sensor/actuator location and feedback gain by minimizing the sum of integral flexible system and control energy. The optimal geometry of piezoelectric actuators was determined for active flutter suppression by minimizing the control performance index by Nam *et al.* (1996). Han and Lee (1999) showed that optimal locations of sensors and actuators can be determined by considering observability and controllability grammian for vibration suppression of composite plate. They used genetic algorithms as an optimization tool. Wang and Wang (2000) presented optimal design of collocated pair of piezoelectric patches on beams. The optimal placement and size of piezoelectric patches was attained by maximizing the controllability index. Demetriou (2000) proposed optimal placement of sensors and actuators by minimizing the optimal cost of the performance index. Hiramoto *et al.* (2000) studied the optimal placement of sensors and actuators for active vibration control of flexible structures using explicit solution of algebraic Riccati equation. Recently, genetic algorithms (GAs) as an optimization technique have been applied to these kind of optimization problems [Ning (2004), Liu *et al.* (2003), Mota *et al.* (2004), Liu *et al.* (2006), Yang *et al.* (2005) and Rao *et al.* (2006)].

1.3 Summary of literature review

Based on the literature survey carried out, it is observed that most widely used modelling methods for vibration of rotating blades can be divided into linear modelling method [Yokoyama (1988)], geometrically non-linear modelling method [Song and Librescu (1997), Song, *et al.* (2001)] and dynamic modelling method [Yoo *et al.* (1995) and Yoo *et al.* (2001b)]. First type of method employs Cartesian deformation variables and linear Cauchy strain measures. However, this approach

displays critical flaw when structures undergo large motions and it produces erroneous results [Kane *et al.* (1987)]. Geometric modeling method uses large deformation and von Kármán strain measures, which has demerits such as cumbersome formulation procedure and the derived equations of motions are non-linear. Linearization is possible only after discarding the gyroscopic coupling. The equations of motion derived using dynamic modelling method are linear and can capture effect of centrifugal stiffening and gyroscopic coupling [Yoo *et al.* (1995) and Yoo *et al.* (2001b)]. Literature in higher shear deformation theory (HSDT) for rotating composite beams using dynamic modeling method is not adequate. MFCs are comparatively new materials for sensing/actuating. Literature in structural model with HSDT effect and optimal control design in rotating composite thin walled beams is scanty.

1.4 Scope of the present work

In the present work structural modelling of rotating composite thin walled beams with HSDT effect using dynamic modeling method is presented. The developed model using dynamic modeling method automatically accommodates the gyroscopic coupling and centrifugal stiffening effect. The model also includes non-classical effects generally exhibited by rotating composite beams such as anisotropy, heterogeneity, warping and transverse shear. The mathematical model is extended to include embedded MFC sensors and actuators. The piezoelectric mass and stiffness are taken into account in the model. Optimal control algorithms viz, LQR and LQG are used to control the dynamic response of rotating composite beams. The optimal locations of MFC sensors and actuators are obtained by minimizing the trace identity of filter Riccati and algebraic Riccati equations, respectively. The locations of sensors and actuators are optimized using a combination of genetic algorithm and sequential quadratic programming algorithms.

1.5 Outline of the thesis

Chapter 1 introduces the work done by previous researchers in the topics associated with this thesis. The literature survey related to vibration studies of

rotating beams, active vibration control using piezoelectric material and optimal placement are outlined. The objectives and contributions of the present research work are also summarized.

In Chapter 2, the equations of motion for rotating composite cantilever beams using dynamic modeling method are derived. First, the equations of motion for untwisted beam are derived and in the later section, these are extended to pretwisted beam configuration.

Chapter 3 presents the free and forced vibration analysis of rotating composite beams. The mathematical model presented in Chapter 2, is used for obtaining approximate solutions by the extended Galerkin's method. The results obtained are compared with the available theoretical and experimental results. The effects of centrifugal stiffening, gyroscopic coupling, pretwist and presetting in rotating beams are investigated.

In Chapter 4, a mathematical model for rotating composite beams with embedded macro fiber composite sensors and actuators is presented. The derived mathematical model includes the effect of higher shear deformation theory (HSDT). The embedded sensors and actuators change the system mass and stiffness. This passive effect of sensors and actuators is included in the mathematical model.

Chapter 5 presents the vibration suppression of rotating beams using macro fibre composite sensors and actuators. The equations of motion derived in Chapter 4 are used for obtaining approximate solutions by the extended Galerkin's method. Passive effects of macro fibre composite and monolithic piezoelectric materials embedded in rotating composite beams are discussed. A controller is designed using LQR and LQG algorithms. The vibration reduction of the beam responses using designed controller are shown.

Chapter 6 deals with the optimal placement of sensors and actuators embedded in rotating beams. Initial approximate locations of sensors and actuators

are obtained using genetic algorithm. By setting the results obtained from the genetic algorithm as initial condition to sequential quadratic programming algorithm, optimal location of sensors and actuators is determined.

Chapter 7 presents the conclusions based on the present work. It also discusses the scope for possible future work.

Chapter 2

Structural modeling of rotating beams

2.1 Introduction

In this chapter, the governing equations of motion describing the vibration characteristics of a thin walled rotating composite beam are derived. Higher shear deformation effect is included. First, potential and kinetic energy equations describing dynamics of un-twisted rotating beam are derived using dynamic modelling method. The equations of motion are obtained by substituting potential and kinetic energy equations in Hamilton's principle. The equations of motion are then extended to include the effect of pretwist, preset and taper in rotating beams.

2.2 Untwisted rotating beam

2.2.1 Coordinate systems

A composite beam of length L and hub radius R_o, rotating with constant angular velocity Ω is considered. The Cartesian inertial frame of reference (X, Y, Z) has its origin at the centre of the hub. The beam coordinate system (x, y, z) is located at offset R_o from the origin O. Further, (i, j, k) and (I, J, K) represent unit vectors in (x, y, z) and (X, Y, Z) coordinate systems respectively (Figures 2.1(a) – (c)). The beam rotates about Y -axis with constant angular velocity $\Omega(\equiv \Omega \mathrm{J} \equiv \Omega \mathrm{j})$. In addition to the above, a local coordinate system (s, n, z) associated with the beam is considered which is shown in Figure 2.1(b).

Instead of w, a non-Cartesian variable $\hat{s}$ denoting axial stretch is used in the present study. u, v and $\hat{s}$ represent displacements along (x, y, z) axes respectively and θ_x, θ_y, ϕ represent rotations about (x, y, z) axes respectively. The displacement variables $\hat{s}$ and w are related by [Yoo, et al. (1995)],

$$\hat{s} = w + \frac{1}{2}\int_0^z \left[\left(\frac{\partial u}{\partial \sigma}\right)^2 + \left(\frac{\partial v}{\partial \sigma}\right)^2\right] d\sigma \tag{2.1}$$

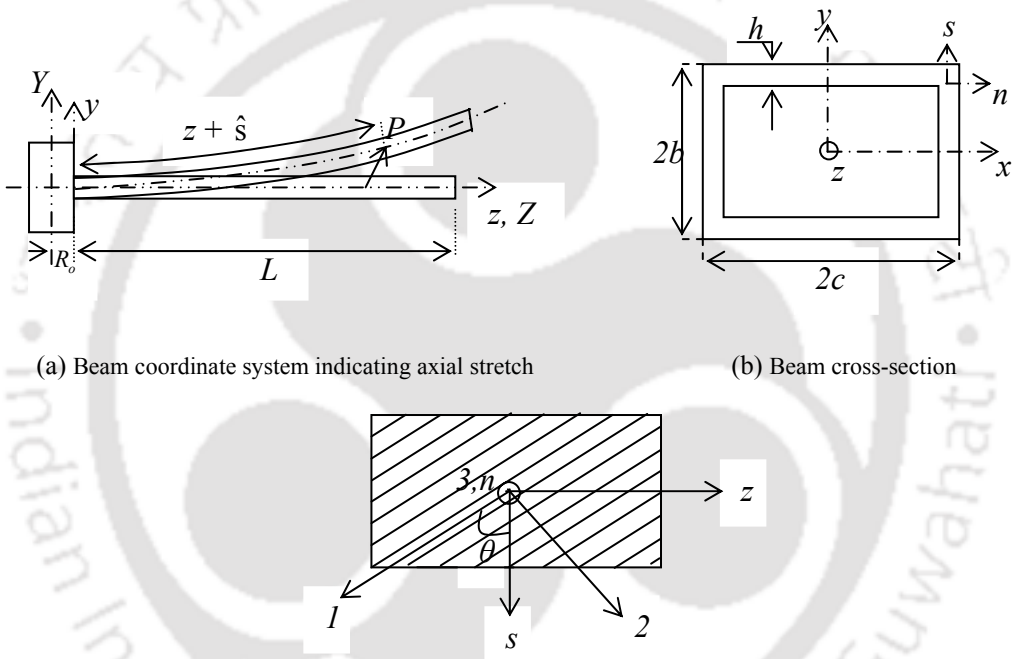

(a) Beam coordinate system indicating axial stretch

(b) Beam cross-section

(c) Fiber angle orientation

Figure 2.1 Untwisted beam configuration and coordinate system

2.2.2 Displacement fields

Linear displacements u, v and w representing lag, flap and extensional motion respectively, for shearable beam can be written as [Song and Librescu (1997)],

$$u = u_o + z\phi \tag{2.2}$$

$$v = v_o - x\phi \tag{2.3}$$

$$w = w_o + \left[\bar{y} + nm\right]\theta_x - \left[\bar{x} + nl\right]\theta_y - \left[F_w + na\right]\phi' + \frac{4n^3}{3h^2}\left[l\left(\theta_y - u_o'\right) - m\left(\theta_x + v_o'\right)\right] \tag{2.4}$$

From Eqs. (2.1) and (2.4), the axial displacement component in arc length stretch coordinate system is

$$\hat{s} = w_o + \left[\bar{y} + nm\right]\theta_x - \left[\bar{x} + nl\right]\theta_y - \left[F_w + na\right]\phi' + \frac{4n^3}{3h^2}\left[l\left(\theta_y - u_o'\right) - m\left(\theta_x + v_o'\right)\right] + \frac{1}{2}\int_0^z \left[\left(\frac{\partial u}{\partial \eta}\right)^2 + \left(\frac{\partial v}{\partial \eta}\right)^2\right] \mathrm{d}\eta \tag{2.5}$$

where, $l = \frac{\mathrm{d}\bar{y}}{\mathrm{d}s}$; $m = -\frac{\mathrm{d}\bar{x}}{\mathrm{d}s}$; $a = m\bar{x} - l\bar{y}$ and $r_n = l\bar{x} + m\bar{y}$;

$F_w = \int_0^s (r_n - \frac{2A_c}{\beta})\mathrm{d}s$ and na represents primary and secondary warping functions respectively;

$\theta_x = \gamma_{yz} - v_o'$ and $\theta_y = \gamma_{xz} - u_o'$ represents rotations about x and y axes respectively and A_c and β are the cross-sectional area and total length of mid line contour respectively.

2.2.3 Stress strain relation

The constitutive stress strain relations for orthotropic material in local coordinate system can be written as,

$$\begin{Bmatrix} \sigma_{ss} \\ \sigma_{zz} \\ \sigma_{nn} \\ \sigma_{nz} \\ \sigma_{ns} \\ \sigma_{sz} \end{Bmatrix} = \begin{bmatrix} \bar{Q}_{11} & \bar{Q}_{12} & \bar{Q}_{13} & 0 & 0 & \bar{Q}_{16} \\ \bar{Q}_{12} & \bar{Q}_{22} & \bar{Q}_{23} & 0 & 0 & \bar{Q}_{26} \\ \bar{Q}_{13} & \bar{Q}_{23} & \bar{Q}_{33} & 0 & 0 & \bar{Q}_{36} \\ 0 & 0 & 0 & \bar{Q}_{44} & \bar{Q}_{45} & 0 \\ 0 & 0 & 0 & \bar{Q}_{45} & \bar{Q}_{55} & 0 \\ \bar{Q}_{16} & \bar{Q}_{26} & \bar{Q}_{36} & 0 & 0 & Q_{66} \end{bmatrix} \begin{Bmatrix} \varepsilon_{ss} \\ \varepsilon_{zz} \\ \varepsilon_{nn} \\ \gamma_{nz} \\ \gamma_{ns} \\ \gamma_{sz} \end{Bmatrix} \tag{2.6}$$

The 3-D composite constitutive Eq. (2.6) is reduced to equivalent 1- D equations by integrating through the thickness and along the mid contour.

2.2.4 Strain displacement relations

The strain field in terms of equivalent 2 – D displacement measures for rotating beam using higher shear deformation theory can be written as [Song and Librescu (1997)]

$$\varepsilon_{zz} = \hat{s}_{,z} \tag{2.7}$$

$$\gamma_{sz} = l\gamma_{yz} - m\gamma_{xz} + (\psi + 2n)\phi' = l\left[\left(1 - \frac{4n^2}{h^2}\right)\bar{\gamma}_{yz}\right] - m\left[\left(1 - \frac{4n^2}{h^2}\right)\bar{\gamma}_{xz}\right] + \psi\phi' \tag{2.8}$$

$$\gamma_{nz} = l\gamma_{xz} + m\gamma_{yz} = l\left[\left(1 - \frac{4n^2}{h^2}\right)\bar{\gamma}_{xz}\right] + m\left[\left(1 - \frac{4n^2}{h^2}\right)\bar{\gamma}_{yz}\right] \tag{2.9}$$

Substituting Eqs. (2.2) – (2.3) and (2.5) in Eq. (2.7) – (2.9) spanwise strain, tangential shear strain and transverse shear strain can be obtained as,

$$\begin{aligned}
&\varepsilon_{zz} = w_o' + [\bar{y} + nm]\theta_x' - [\bar{x} + nl]\theta_y' - [F_w + na]\phi'' \\
&+ \frac{4n^3}{3h^2}\left[l\left(\theta_y' - u_o''\right) - m\left(\theta_x' + v_o''\right)\right] \\
&+ \frac{1}{2}\int_0^z \left[\begin{aligned}
&\frac{\partial u_o}{\partial \eta}\frac{\partial u_o'}{\partial \eta} + \frac{\partial v_o}{\partial \eta}\frac{\partial v_o'}{\partial \eta} - \left(\frac{\partial u_o}{\partial \eta}\frac{\partial \phi'}{\partial \eta} + \frac{\partial \phi}{\partial \eta}\frac{\partial u_o'}{\partial \eta}\right)(\bar{y} + nm) \\
&+ \left(\frac{\partial v_o}{\partial \eta}\frac{\partial \phi'}{\partial \eta} + \frac{\partial \phi}{\partial \eta}\frac{\partial v_o'}{\partial \eta}\right)(\bar{x} + nl) + \left\{(\bar{x} + nl)^2 + (\bar{y} + nm)^2\right\}\frac{\partial \phi}{\partial \eta}\frac{\partial \phi'}{\partial \eta}
\end{aligned}\right] \mathrm{d}\eta \\
&= \varepsilon_{zz}^{(0)} + n\varepsilon_{zz}^{(1)} + n^3\varepsilon_{zz}^{(3)}
\end{aligned} \tag{2.10}$$

$$\begin{aligned}
\gamma_{sz} &= \left(1 - \frac{4n^3}{h^2}\right)l\left(\theta_x + v_o'\right) + m\left(\theta_y - u_o'\right) + \psi\phi' \\
&= \gamma_{sz}^{(0)} + n^2\gamma_{sz}^{(2)}
\end{aligned} \tag{2.11}$$

$$\begin{aligned}
\gamma_{nz} &= \left(1 - \frac{4n^3}{h^2}\right)\left[m\left(\theta_x + v_o'\right) - l\left(\theta_y - u_o'\right)\right] \\
&= \gamma_{nz}^{(0)} + n^2\gamma_{nz}^{(2)}
\end{aligned} \tag{2.12}$$

The hoop stress is negligibly small when the hollow section is not subjected to internal pressure. With this assumption and integrating over thickness, 3-D equations are reduced to 2-D equivalent as,

$$\begin{Bmatrix} N_{zz}^{0} \\ N_{zz}^{1} \\ N_{zz}^{3} \\ N_{sz}^{0} \\ N_{sz}^{2} \end{Bmatrix} = \begin{bmatrix} k_{11} & k_{21} & k_{31} & k_{41} & k_{51} \\ k_{12} & k_{22} & k_{32} & k_{42} & k_{52} \\ k_{13} & k_{23} & k_{33} & k_{43} & k_{53} \\ k_{14} & k_{24} & k_{34} & k_{44} & k_{54} \\ k_{15} & k_{25} & k_{35} & k_{45} & k_{55} \end{bmatrix} \begin{Bmatrix} \varepsilon_{zz}^{0} \\ \varepsilon_{zz}^{1} \\ \varepsilon_{zz}^{3} \\ \gamma_{sz}^{0} \\ \gamma_{sz}^{2} \end{Bmatrix}; \begin{Bmatrix} N_{nz}^{0} \\ N_{nz}^{2} \end{Bmatrix} = \begin{bmatrix} A_{44} & D_{44} \\ D_{44} & H_{44} \end{bmatrix} \begin{Bmatrix} \gamma_{nz}^{0} \\ \gamma_{nz}^{2} \end{Bmatrix} \tag{2.13}$$

where, $(A,\ B,\ D,\ F,\ H,\ I,\ J) = \sum_{1}^{N} \int_{-h/2}^{h/2} \bar{Q}_{ij} (1,\ n,\ n^2,\ n^3,\ n^4,\ n^5,\ n^6) \mathrm{d}n$ and

$k_{11} = A_{22} - A_{12}^2 / A_{11};$ $k_{12} = B_{22} - B_{12} A_{12} / A_{11};$ $k_{13} = F_{22} - F_{12} A_{12} / A_{11};$

$k_{14} = A_{26} - A_{16} A_{12} / A_{11};$ $k_{15} = D_{26} - D_{16} A_{12} / A_{11};$ $k_{22} = D_{22} - B_{12}^2 / A_{11};$

$k_{23} = H_{22} - F_{12} B_{12} / A_{11};$ $k_{24} = B_{26} - A_{16} B_{12} / A_{11};$ $k_{25} = F_{26} - D_{16} B_{12} / A_{11};$

$k_{33} = J_{22} - F_{12}^2 / A_{11};$ $k_{34} = F_{26} - A_{16} F_{12} / A_{11};$ $k_{35} = I_{26} - D_{16} F_{12} / A_{11};$

$k_{44} = A_{66} - A_{16}^2 / A_{11};$ $k_{45} = D_{66} - A_{16} D_{16} / A_{11};$ $k_{55} = H_{66} - D_{16}^2 / A_{11};$

2.2.5 Hamilton's principle

The equations of motion of rotating beam are derived using Hamilton's Principle. The Hamilton's variational equation for a dynamic system is written as,

$$\int_{t_1}^{t_2} [\delta T - \delta V + \delta W] \mathrm{d}t = 0 \tag{2.14}$$

where, V, T and W are the potential energy, kinetic energy and virtual work respectively.

$$V = \tfrac{1}{2} \int_{\tau} \sigma_{ij} \varepsilon_{ij} \, \mathrm{d}\tau \tag{2.15}$$

$$T = \tfrac{1}{2} \int_{\tau} \rho (\dot{\mathbf{R}}_{\mathbf{i}} . \dot{\mathbf{R}}_{\mathbf{i}}) \mathrm{d}\tau \tag{2.16}$$

2.2.6 Variational potential energy

Assuming in–plane deformations are negligible, (i.e $\varepsilon_{ss} = \varepsilon_{nn} = \gamma_{ns} = 0$) strain energy equation can be written as [Song and Librescu (1997)],

$$V = \tfrac{1}{2}\int_{\tau}\left[\sigma_{zz}\varepsilon_{zz} + \sigma_{sz}\gamma_{sz} + \sigma_{nz}\gamma_{nz}\right]\mathrm{d}\tau \tag{2.17}$$

$$\delta V = \int_{t_o}^{t_1}\int_{\tau}\left[\sigma_{zz}\delta\varepsilon_{zz} + \sigma_{sz}\delta\gamma_{sz} + \sigma_{nz}\delta\gamma_{nz}\right]\mathrm{d}\tau\ \mathrm{d}t \tag{2.18}$$

Substituting Eqs. (2.2) – (2.13) in Eq. (2.18) total variational strain energy equation is obtained as,

$$\delta V = \int_{t_1}^{t_2}\int_{0}^{L}\begin{bmatrix}
+\left\{(a_{43}+\tilde{a}_2)\theta_x' - (a_{44}+\tilde{a}_1)(\theta_y - u_o') + \tilde{a}_3 v_o''\right\}\delta u_o' \\
+\left\{\tilde{a}_6 u_o'' + \tilde{a}_4(\theta_x + v_o') - \tilde{a}_5\theta_y'\right\}\delta u_o'' \\
+\left\{(a_{55}+\tilde{a}_7)(\theta_x + v_o') - (a_{52}+\tilde{a}_8)\theta_y' + \tilde{a}_4 u_o''\right\}\delta v_o' \\
+\left\{\tilde{a}_{10} v_o'' + \tilde{a}_3(-\theta_y + u_o') + \tilde{a}_9\theta_x'\right\}\delta v_o'' + \left\{a_{17} w_o' + a_{77}\phi'\right\}\delta\phi' \\
+\left\{a_{11} w_o' + a_{17}\phi'\right\}\delta w_o' + a_{66}\phi''\delta\phi'' \\
+\left\{(a_{55}+\tilde{a}_7)(\theta_x + v_o') - (a_{52}+\tilde{a}_8)\theta_y' + \tilde{a}_4 u_o''\right\}\delta\theta_x \\
+\left\{(a_{33}+\tilde{a}_{12})\theta_x') + (a_{43}+\tilde{a}_2)(-\theta_y + u_o') + \tilde{a}_9 v_o''\right\}\delta\theta_x' \\
-\left\{(a_{43}+\tilde{a}_2)\theta_x' - (a_{44}+\tilde{a}_1)(\theta_y - u_o') + \tilde{a}_3 v_o''\right\}\delta\theta_y \\
-\left\{(a_{52}+\tilde{a}_8)(\theta_x + v_o') - (a_{22}+\tilde{a}_{11})\theta_y' + \tilde{a}_5 u_o''\right\}\delta\theta_y'
\end{bmatrix}\mathrm{d}z\ \mathrm{d}t \tag{2.19}$$

2.2.7 Variational kinetic energy

The position vector relative to the fixed origin O of a point on the deformed beam is obtained as,

$$\mathbf{R} = R_o\mathbf{k} + x\mathbf{i} + y\mathbf{j} + z\mathbf{k} + u\mathbf{i} + v\mathbf{j} + w\mathbf{k} \tag{2.20}$$

Differentiating twice with respect to time, the acceleration of point P can be written as,

$$\ddot{\mathbf{R}} = \left(\ddot{u} + 2\Omega\dot{w} - \Omega^2(\mathrm{x+u})\right)\mathbf{I} + \ddot{v}\mathbf{J} + \left(\ddot{w} - 2\Omega\dot{u} - \Omega^2(R_o + z + w)\right)\mathbf{K} \tag{2.21}$$

Variational kinetic energy is obtained by substituting Eqs. (2.2)– (2.13) and (2.20) – (2.21) in Eq. (2.16).

$$\delta T = -\int_{t_1}^{t_2}\int_0^L \left[\begin{array}{l} b_1\left\{\ddot{u}_o + 2\Omega\dot{w}_o - \Omega^2 u_o\right\}\delta u_o + b_1\ddot{v}_o'\delta v_o \\ +\left\{\begin{array}{l}\tilde{M}_4\tilde{I}_{mm}\ddot{\theta}_y - \tilde{M}_6\tilde{I}_{mm}(\ddot{\theta}_y + \ddot{u}_o') \\ -\Omega^2\left(\tilde{M}_4\tilde{I}_{mm}\theta_y - \tilde{M}_6\tilde{I}_{mm}(\theta_y + u_o') - R_z b_1 u_o'\right)\end{array}\right\}\delta u_o' \\ +\left\{\begin{array}{l}\tilde{M}_6\tilde{I}_\mu(\ddot{\theta}_x + \ddot{v}_o') - \tilde{M}_4\tilde{I}_\mu\ddot{\theta}_x - 2\Omega\tilde{M}_4\tilde{I}_\mu\dot{\phi} \\ -\Omega^2\left(\tilde{M}_6\tilde{I}_\mu(\ddot{\theta}_x + \ddot{v}_o') - \tilde{M}_4\tilde{I}_\mu\ddot{\theta}_x - R_z b_1 v_o'\right)\end{array}\right\}\delta v_o' \\ +b_1\left\{\ddot{w}_o - 2\Omega\dot{u}_o - \Omega^2(R_o + z + w_o)\right\}\delta w_o \\ +\left\{\begin{array}{l}I_{xx}\ddot{\theta}_x + (\tilde{M}_6 - \tilde{M}_4)\tilde{I}_\mu(\ddot{\theta}_x + \ddot{v}_o') - \tilde{M}_4\tilde{I}_\mu\ddot{\theta}_x \\ +2\Omega(I_{xx} - \tilde{M}_4\tilde{I}_\mu)\dot{\phi} \\ -\Omega^2\left(I_{xx}\theta_x + (\tilde{M}_6 - \tilde{M}_4)\tilde{I}_\mu(\theta_x + v_o') - \tilde{M}_4\tilde{I}_\mu\theta_x\right)\end{array}\right\}\delta\theta_x \\ +\left\{\begin{array}{l}(\tilde{M}_6 - \tilde{M}_4)\tilde{I}_{mm}(\ddot{\theta}_y - \ddot{u}_o') + I_{yy}\ddot{\theta}_y - \tilde{M}_4\tilde{I}_{mm}\ddot{\theta}_y \\ -\Omega^2\left\{I_{yy}\theta_y + (\tilde{M}_6 - \tilde{M}_4)\tilde{I}_{mm}(\theta_y - u_o') - \tilde{M}_4\tilde{I}_{mm}\theta_y\right\}\end{array}\right\}\delta\theta_y \\ +\left\{(I_{xx} + I_{yy})\ddot{\phi} + 2\Omega[(\tilde{M}_4\tilde{I}_\mu - I_{xx})\dot{\theta}_x + \tilde{M}_4\tilde{I}_\mu\dot{v}_o'] - \Omega^2 I_{xx}\phi\right\}\delta\phi \\ +\left\{I_{ww}\ddot{\phi}' - \Omega^2\left(I_{ww}\phi' - R_z b_1(I_{xx} + I_{yy})\phi'\right)\right\}\delta\phi' \end{array}\right] \mathrm{d}z\,\mathrm{d}t \tag{2.22}$$

2.2.8 Equations of motion and boundary conditions

Upon substituting Eqs. (2.19) and (2.22) in Eq. (2.14), Equations of motion for untwisted beam are obtained as,

$$\begin{aligned}\delta u_o:\ & \tilde{a}_4(\theta_x'' + v_o''') - \tilde{a}_5\theta_y''' + \tilde{a}_6 u_o^{IV} - (a_{43} + \tilde{a}_2)\theta_x'' + (a_{44} + \tilde{a}_1)(\theta_y' - u_o'') - \tilde{a}_3 v_o''' \\ & + b_1(\ddot{u}_o - \underline{2\Omega\dot{w}_o} - \Omega^2 u_o) + (\tilde{M}_6 - \tilde{M}_4)\tilde{I}_{mm}\ddot{\theta}_y' + \tilde{M}_6\tilde{I}_{mm}\ddot{u}_o'' \\ & - \Omega^2[(\tilde{M}_6 - \tilde{M}_4)\tilde{I}_{mm}\theta_y' + \tilde{M}_6\tilde{I}_{mm}u_o'' - \underline{\underline{R_z b_1 u_o''}}] = 0\end{aligned} \tag{2.23}$$

$$\begin{aligned}\delta v_o:\ & \tilde{a}_3(-\theta_y'' + u_o''') + \tilde{a}_9\theta_x''' + \tilde{a}_{10}v_o^{IV} + (a_{52} + \tilde{a}_8)\theta_y'' - \tilde{a}_4 u_o''' - (a_{55} + \tilde{a}_7)(\theta_x' + v_o'') \\ & + b_1\ddot{v}_o - (\tilde{M}_6 - \tilde{M}_4)\tilde{I}_\mu\ddot{\theta}_x' - \tilde{M}_6\tilde{I}_\mu\ddot{v}_o'' + \underline{2\Omega\tilde{M}_4\tilde{I}_\mu\dot{\phi}'} - \Omega^2[-(\tilde{M}_6 - \tilde{M}_4)\tilde{I}_\mu\theta_x' \\ & - \tilde{M}_6\tilde{I}_\mu v_o'' - \underline{\underline{R_z b_1 v_o''}}] = 0\end{aligned} \tag{2.24}$$

$$\delta w_o:\ -a_{11}w_o'' - a_{17}\phi'' + b_1\left(\ddot{w}_o - \underline{2\Omega\dot{u}_o} - \Omega^2(R_o + z + w_o)\right) = 0 \tag{2.25}$$

$$\delta\theta_x:\ (a_{55}+\tilde{a}_7)(\theta_x+v_o')-(a_{52}+\tilde{a}_8)\theta_y'+\tilde{a}_4u_o''-(a_{33}+\tilde{a}_2)\theta_x''+(a_{43}+\tilde{a}_2)(-\theta_y'+u_o'')-\tilde{a}_9v_o'''+\underline{2\Omega(I_{xx}-\tilde{M}_4\tilde{I}_\mu)\dot{\phi}}+I_{xx}\underline{\ddot{\theta}_x}+(\tilde{M}_6-\tilde{M}_4)\tilde{I}_\mu(\underline{\ddot{\theta}_x}+\underline{\ddot{v}_o'})-\tilde{M}_4\tilde{I}_\mu\underline{\ddot{\theta}_x}-\Omega^2[I_{xx}\theta_x+(\tilde{M}_6-\tilde{M}_4)\tilde{I}_\mu(\theta_x+v_o')-\tilde{M}_4\tilde{I}_\mu\theta_x]=0 \tag{2.26}$$

$$\delta\theta_y:\ (a_{44}+\tilde{a}_1)(\theta_y-u_o')-(a_{43}+\tilde{a}_2)\theta_x'+\tilde{a}_3v_o''-(a_{22}+\tilde{a}_{11})\theta_y''+(a_{52}+\tilde{a}_8)(\theta_x'+v_o'')+\tilde{a}_5u_o'''+(\tilde{M}_6-\tilde{M}_4)\tilde{I}_{mm}(\underline{\ddot{\theta}_y}-\underline{\ddot{u}_o'})+I_{yy}\underline{\ddot{\theta}_y}-\tilde{M}_4\tilde{I}_{mm}\underline{\ddot{\theta}_y}-\Omega^2[I_{yy}\ddot{\theta}_y+(\tilde{M}_6-\tilde{M}_4)\tilde{I}_{mm}(\theta_y-u_o')-\tilde{M}_4\tilde{I}_{mm}\theta_y]=0 \tag{2.27}$$

$$\delta\phi:\ -a_{77}\phi''-a_{17}w_o''+a_{66}\phi^{IV}+(I_{xx}+I_{yy})\ddot{\phi}-I_{ww}\ddot{\phi}''+\underline{2\Omega((\tilde{M}_4\tilde{I}_\mu-I_{xx})\dot{\theta}_x+\tilde{M}_4\tilde{I}_\mu\dot{v}_o')}-\Omega^2[I_{xx}\phi-I_{ww}\phi''-\underline{\underline{R_zb_1(I_{xx}+I_{yy})\phi''}}]=0 \tag{2.28}$$

The forced boundary conditions are obtained as,

$$\delta u_o:\tilde{a}_5\theta_y''-\tilde{a}_4(\theta_x'+v_o'')-\tilde{a}_6u_o'''-(a_{44}+\tilde{a}_1)(\theta_y-u_o')+\tilde{a}_3v_o''+(a_{43}+\tilde{a}_2)\theta_x'+(\tilde{M}_6-\tilde{M}_4)\tilde{I}_{mm}\ddot{\theta}_y+\tilde{M}_6\tilde{I}_{mm}\ddot{u}_o'+\Omega^2[-(\tilde{M}_6-\tilde{M}_4)\tilde{I}_{mm}\theta_y-\tilde{M}_6\tilde{I}_{mm}u_o'-R_zb_1u_o']=0 \tag{2.29}$$

$$\delta u_o':\tilde{a}_4(\theta_x+v_o')-\tilde{a}_5\theta_y'+\tilde{a}_6u_o''=0 \tag{2.30}$$

$$\delta v_o:\tilde{a}_3(\theta_y'-u_o'')-\tilde{a}_9\theta_x''-\tilde{a}_{10}v_o'''+(a_{55}+\tilde{a}_7)(\theta_x+v_o')+\tilde{a}_4u_o''-(a_{52}+\tilde{a}_8)\theta_y'+(\tilde{M}_6-\tilde{M}_4)\tilde{I}_\mu\ddot{\theta}_x+\tilde{M}_6\tilde{I}_\mu\ddot{v}_o'-\Omega^2[(\tilde{M}_6-\tilde{M}_4)\tilde{I}_\mu\theta_x+\tilde{M}_6\tilde{I}_\mu v_o'-R_zb_1v_o']=0 \tag{2.31}$$

$$\delta v_o':+\tilde{a}_3(-\theta_y+u_o')+\tilde{a}_9\theta_x'+\tilde{a}_{10}v_o''=0 \tag{2.32}$$

$$\delta w_o:a_{11}w_o'+a_{17}\phi'=0 \tag{2.33}$$

$$\delta\theta_x:(a_{33}+\tilde{a}_{12})\theta_x'-(a_{43}+\tilde{a}_2)(\theta_y-u_o')+\tilde{a}_9v_o''=0 \tag{2.34}$$

$$\delta\theta_y:(a_{22}+\tilde{a}_{11})\theta_y'-(a_{52}+\tilde{a}_8)(\theta_x+v_o')-\tilde{a}_5u_o''=0 \tag{2.35}$$

$$\delta\phi:a_{77}\phi'+\tilde{a}_{17}w_o'-a_{66}\phi'''+I_{ww}\ddot{\phi}'+\Omega^2(-I_{ww}\phi'+R_zb_1(I_{xx}+I_{yy})\phi'')=0 \tag{2.36}$$

$$\delta\phi':a_{66}\phi'' \tag{2.37}$$

Global stiffness quantities a_{ij} and $\tilde{a}_i$ for untwisted beam are defined in Appendix A and inertia quantities are defined in Appendix C.

2.3 Non-uniform pretwisted rotating beam

The beam coordinate and local beam coordinate systems are related by the transformation rule

$$\begin{aligned} x &= x^p \cos(\gamma + \beta(z)) - y^p \sin(\gamma + \beta(z)) \\ y &= x^p \sin(\gamma + \beta(z)) + y^p \cos(\gamma + \beta(z)); \;\; z = z^p \end{aligned} \tag{2.38}$$

where, $\left(x^p,\ y^p,\ z^p\right)$ represents local beam coordinate system (Figure 2.2).

Taper parameters in the beam are taken as $\eta = \dfrac{cr}{ct} = \dfrac{br}{bt}$, where, cr, ct, br and bt are the chord and breadth at root and tip of the beam respectively. Midline cross-section profile can be written as,

$$c(z) = \frac{cr}{\eta}\left[1 + \frac{(\eta - 1)(L - z)}{L}\right]; b(z) = \frac{br}{\eta}\left[1 + \frac{(\eta - 1)(L - z)}{L}\right] \tag{2.39}$$

2.3.1 Displacement fields

Linear displacements u, v and w representing lag, flap and extensional motion respectively, are obtained for pretwisted shearable beam by substituting Eq. (2.38) in Eqs. (2.2) – (2.4) as,

$$u = u_o - (\bar{y}^p \cos\beta + \bar{x}^p \sin\beta)\phi - n(m^p \cos\beta + l^p \sin\beta)\phi \tag{2.40}$$

$$v = v_o + (\bar{x}^p \cos\beta - \bar{y}^p \sin\beta)\phi + n(l^p \cos\beta - m^p \sin\beta)\phi \tag{2.41}$$

$$\begin{aligned} w = w_o &+ \left[\left(\bar{y}^p + nm^p\right)\cos\beta + \left(\bar{x}^p + nl^p\right)\sin\beta\right]\theta_x - [\left(\bar{x}^p + nl^p\right)\cos\beta - (\bar{y}^p \\ &+ nm^p)\sin\beta]\theta_y + \frac{4n^3}{3h^2}[\left(\theta_y - u_o^{'}\right)\left(l^p \cos\beta - m^p \sin\beta\right) - \left(\theta_x + v_o^{'}\right)(m^p \cos\beta \\ &+ l^p \sin\beta)] - \left[F_w + na\right]\phi' \end{aligned} \tag{2.42}$$

From Eqs. (2.1) and (2.42), the axial displacement component in arc length stretch coordinate system is

$$\hat{s} = w_o + \left[\left(\bar{y}^p + nm^p\right)\cos\beta + \left(\bar{x}^p + nl^p\right)\sin\beta\right]\theta_x - [\left(\bar{x}^p + nl^p\right)\cos\beta - (\bar{y}^p + nm^p)\sin\beta]\theta_y + \frac{4n^3}{3h^2}[\left(\theta_y - u_o^{'}\right)\left(l^p\cos\beta - m^p\sin\beta\right) - \left(\theta_x + v_o^{'}\right)(m^p\cos\beta + l^p\sin\beta)] - \left[F_w + na\right]\phi' + \frac{1}{2}\int_0^z\left[\left(\frac{\partial u}{\partial\sigma}\right)^2 + \left(\frac{\partial v}{\partial\sigma}\right)^2\right]\mathrm{d}\sigma \tag{2.43}$$

where $l^p = \frac{\mathrm{d}\bar{y}^p}{\mathrm{d}s}$, $m^p = -\frac{\mathrm{d}\bar{x}^p}{\mathrm{d}s}$ and $a = m^p\bar{x}^p - l^p\bar{y}^p$.

2.3.2 Variational potential energy for pretwisted rotating beam

The procedure described in sections 2.2.4 – 2.2.6 is adopted to derive variational potential energy equation of pretwisted beam. First, substituting Eqs. (2.40) – (2.41) and (2.44) in Eqs. (2.7) – (2.9) span wise strain, tangential shear strain and transverse shear strain are obtained. Substituting the obtained strain measures and stress measures from Eq. (2.6) in Eq. (2.18), total variational strain energy equation is obtained as,

$$\delta V = \int_{t1}^{t2}\int_0^L \left\{\begin{array}{l}
\left\{\begin{array}{l}\theta_x'\left(a_{34}+\delta_h\tilde{a}_2\right)+\theta_y'\left(-a_{42}+\delta_h\tilde{a}_{30}\right)+\left(\theta_x+v_0'\right)\\ \left(a_{45}+\tilde{a}_{31}\right)+\left(-\theta_y+u_0'\right)\left(a_{44}+\tilde{a}_1\right)+u_0''a_{32}+\tilde{a}_3v_0''\end{array}\right\}\delta u_0' \\
+\left\{\left(\tilde{a}_{34}\theta_x' - \tilde{a}_5\theta_y' + \tilde{a}_4\left(\theta_x+v_0'\right)+\tilde{a}_{32}\left(-\theta_y+u_0'\right)+\tilde{a}_{35}v_0''+\tilde{a}_6u_0''\right)\right\}\delta u_0'' \\
+\left\{\begin{array}{l}\theta_x'\left(a_{35}+\tilde{a}_{30}\right)+\theta_y'\left(-a_{52}-\tilde{a}_8\right)+\left(\theta_x+v_0'\right)\left(a_{55}+\tilde{a}_7\right)\\ +\left(-\theta_y+u_0'\right)\left(a_{45}+\tilde{a}_{31}\right)+u_0''a_4-v_0''\tilde{a}_{32}\end{array}\right\}\delta v_0' \\
+\left\{\left(\tilde{a}_9\theta_x' - \tilde{a}_{34}\theta_y' - \tilde{a}_{32}\left(\theta_x+v_0'\right)+\tilde{a}_3\left(-\theta_y+u_0'\right)+\tilde{a}_{35}u_0''+\tilde{a}_{10}v_0''\right)\right\}\delta v_0'' \\
+\left\{\begin{array}{l}\theta_x'\left(a_{35}+\tilde{a}_{30}\right)+\theta_y'\left(-a_{25}-\tilde{a}_8\right)+\left(\theta_x+v_0'\right)\left(a_{55}+\tilde{a}_7\right)\\ +\left(-\theta_y+u_0'\right)\left(a_{45}+\tilde{a}_{31}\right)+u_0''\tilde{a}_4+v_0''\left(-\tilde{a}_{32}\right)\end{array}\right\}\delta\theta_x \\
+\left\{\begin{array}{l}\theta_x'\left(a_{33}+\tilde{a}_{12}\right)+\theta_y'\left(-a_{23}-\tilde{a}_{33}\right)+\left(\theta_x+v_0'\right)\left(a_{35}+\tilde{a}_{30}\right)\\ +\left(-\theta_y+u_0'\right)\left(a_{34}+\tilde{a}_2\right)+u_0''\tilde{a}_{34}+v_0''\tilde{a}_9\end{array}\right\}\delta\theta_x' \\
-\left\{\begin{array}{l}\theta_x'\left(a_{34}+\tilde{a}_2\right)+\theta_y'\left(-a_{42}+\tilde{a}_{30}\right)+\left(\theta_x+v_0'\right)\left(a_{45}+\tilde{a}_{31}\right)\\ +\left(-\theta_y+u_0'\right)\left(a_{44}+\tilde{a}_1\right)+u_0''\tilde{a}_{32}+v_0''\tilde{a}_3\end{array}\right\}\delta\theta_y \\
-\left\{\begin{array}{l}\theta_x'\left(a_{23}+\tilde{a}_{33}\right)+\theta_y'\left(-a_{22}-\tilde{a}_{11}\right)+\left(\theta_x+v_0'\right)\left(a_{25}+\tilde{a}_8\right)\\ +\left(-\theta_y+u_0'\right)\left(a_{24}-\tilde{a}_{30}\right)+u_0''\tilde{a}_5+v_0''\tilde{a}_{34}\end{array}\right\}\delta\theta_y' \\
+\left\{a_{11}w_o+\tilde{a}_{17}\phi'\right\}\delta w_o+\left\{\tilde{a}_{17}w_o+a_{77}\phi'\right\}\delta\phi'+a_{66}\phi''\delta\phi''
\end{array}\right\}\mathrm{d}z\mathrm{d}t \tag{2.44}$$

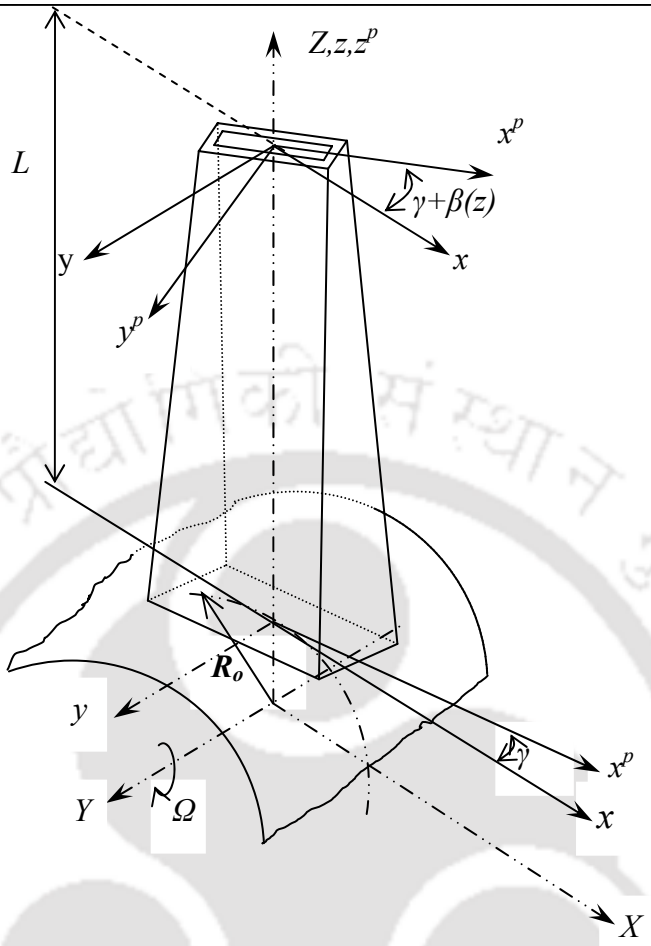

(a) Beam coordinate system

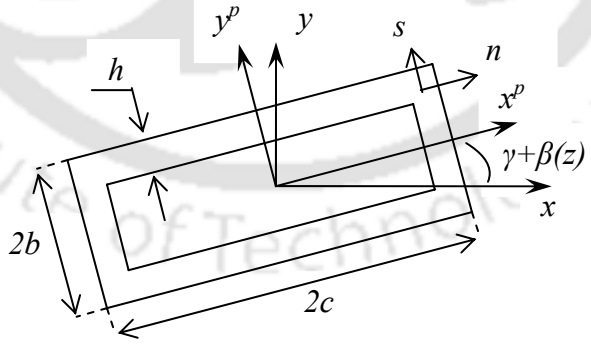

(b) Beam cross-section

Figure 2.2. Pretwisted beam configuration and coordinate system

2.3.3 Variational kinetic energy for pretwisted rotating beam

Kinetic energy equation can be derived by substituting Eqs. (2.40) – (2.41), (2.43) and (2.20) in Eq. (2.16).

$$\delta T = -\int_{t0}^{t1}\int_{0}^{L}\left\{\begin{array}{l} b_1\left(\ddot{u}_0 + 2\Omega\dot{w}_o - \Omega^2 u_0\right)\delta u_0 + b_1\left\{\ddot{w}_o - 2\Omega\dot{u}_0 - \Omega^2\left(R_0 + z + w_o\right)\right\}\delta w_o + \\ +\left\{\begin{array}{l} +I_3\ddot{\theta}_y - I_1\left(\ddot{\theta}_y - \ddot{u}_0'\right) - I_6\ddot{\theta}_x + I_5\left(\ddot{\theta}_x + \ddot{v}_0'\right) - 2\Omega I_6\delta_h\dot{\phi} \\ -\Omega^2\left[I_3\theta_y - I_1\left(\theta_y - u_0'\right) - I_6\theta_x + I_5\left(\theta_x + v_0'\right) - b_1R_2u_0'\right]\end{array}\right\}\delta u_0' + b_1\ddot{v}_0\delta v_0 \\ +\left\{\begin{array}{l} -I_4\ddot{\theta}_x + I_2\left(\ddot{\theta}_x + \ddot{v}_0'\right) + I_6\ddot{\theta}_y - I_5\left(\ddot{\theta}_y - \ddot{u}_0'\right) - 2\Omega I_4\dot{\phi} \\ -\Omega^2\left[-I_4\theta_x + I_2\left(\theta_x + v_0'\right) + I_6\theta_y - I_5\left(\theta_y - u_0'\right) - b_1R_zv_0'\right]\end{array}\right\}\delta v_0' \\ +\left\{\begin{array}{l} \ddot{\theta}_x\left(I_8 - 2I_4 + I_2\right) + \ddot{v}_0'\left(I_2 - I_4\right) + \ddot{\theta}_y\left(-I_9 + 2I_6 - I_5\right) + \ddot{u}_0'\left(-I_6 + I_5\right) \\ -2\Omega\left[-I_8\dot{\phi} + I_4\dot{\phi}\right] - \Omega^2\left[\begin{array}{l}\theta_x\left(I_8 - 2I_4 + I_2\right) + v_0'\left(I_2 - I_4\right) \\ +\theta_y\left(-I_9 + 2I_6 - I_5\right) + u_0'\left(-I_6 + I_5\right)\end{array}\right]\end{array}\right\}\delta\theta_x \\ +\left\{\begin{array}{l} \ddot{\theta}_y\left(I_7 - 2I_3 + I_1\right) + \ddot{u}_0'\left(I_3 - I_1\right) + \ddot{\theta}_x\left(-I_9 + 2I_6 - I_5\right) + \ddot{v}_0'\left(I_6 - I_5\right) \\ -2\Omega\left[I_9\dot{\phi} - I_6\dot{\phi}\right] - \Omega^2\left[\begin{array}{l}\theta_y\left(I_7 - 2I_3 + I_1\right) + u_0'\left(I_3 - I_1\right) \\ +\theta_x\left(-I_9 + 2I_6 - I_5\right) + v_0'\left(I_6 - I_5\right)\end{array}\right]\end{array}\right\}\delta\theta_y \\ +\left\{\begin{array}{l} \left(I_8 + I_7\right)\ddot{\phi} - \Omega^2\left[\left(I_8 - I_7\right)\phi - I_9\right] \\ -2\Omega\left[I_8\dot{\theta}_x - I_9\dot{\theta}_y + I_6\left(\dot{\theta}_y - \dot{u}_0'\right) - I_4\left(\dot{\theta}_x + \dot{v}_0'\right)\right]\end{array}\right\}\delta\phi \\ +\left\{I_{ww}\ddot{\phi}' - \Omega^2\left[I_{ww}\phi' - R_2\left(I_8 + I_7\right)\phi'\right]\right\}\delta\phi' \end{array}\right\}\mathrm{d}z\ \mathrm{d}t \quad (2.45)$$

2.3.4 Equations of motion and boundary conditions for pretwisted rotating beam

Equations of motion for a pretwisted beam are obtained by substituting Eqs. (2.44) – (2.45) in Hamilton's principle (Eq. 2.14).

$$\begin{aligned} \delta u_o :\ & \tilde{a}_4(\theta_x'' + v_o''') - \tilde{a}_5\theta_y''' + \tilde{a}_6u_o^{IV} - (a_{43} + \tilde{a}_2)\theta_x'' + (a_{44} + \tilde{a}_1)(\theta_y' - u_o'') - \tilde{a}_3v_o''' \\ & + \tilde{a}_{34}\theta_x''' - \tilde{a}_{32}(\theta_y'' - u_o''') + \tilde{a}_{35}v_o^{IV} + (a_{42} - \tilde{a}_{30})\theta_y'' - (a_{45} + \tilde{a}_{31})(\theta_x' + v_o'') \\ & + b_1(\ddot{u}_o - \underline{2\Omega\dot{w}_o} - \Omega^2u_o) - I_1\ddot{u}_o'' - \underline{\ddot{\theta}_y'}(I_3 - I_1) - I_5\ddot{v}_o'' - \underline{\ddot{\theta}_x'}(I_5 - I_6) + \underline{2\Omega I_6\dot{\phi}'} \\ & - \Omega^2[-I_1u_o'' - \theta_y'(I_3 - I_1) - I_5v_o'' - \theta_x'(I_5 - I_6) + \underline{\underline{R_zb_1u_o''}}] = 0 \end{aligned} \quad (2.46)$$

$$\delta v_o:\ \tilde{a}_3(-\theta_y'' + u_o''') + \tilde{a}_9\theta_x''' + \tilde{a}_{10}v_o^{IV} + (a_{52}+\tilde{a}_8)\theta_y'' - \tilde{a}_4u_o''' - (a_{55}+\tilde{a}_7)(\theta_x' + v_o'')$$
$$-\tilde{a}_{34}\theta_y''' - \tilde{a}_{32}(\theta_x'' + v_o''') + \tilde{a}_{35}u_o^{iv} - (a_{35}+\tilde{a}_{30})\theta_x'' - (a_{45}+\tilde{a}_{31})(-\theta_y' + u_o'') + b_1\ddot{v}_o$$
$$-I_2\ddot{v}_o'' - \underset{---}{\ddot{\theta}_x'}(I_2 - I_4) - I_5\ddot{u}_o'' - \underset{---}{\ddot{\theta}_y'}(I_6 - I_5) + \underline{2\Omega I_4\dot{\phi}'} - \Omega^2[-I_2v_o'' - \theta_x'(I_2 - I_4)$$
$$-I_5u_o'' - \theta_y'(I_6 - I_5) + \underline{\underline{R_zb_1v_o''}}] = 0 \tag{2.47}$$

$$\delta w_o:\ -a_{11}w_o'' - \tilde{a}_{17}\phi'' + b_1\left(\ddot{w}_o + \underline{2\Omega\dot{u}_o} - \Omega^2(R_o + z + w_o)\right) = 0 \tag{2.48}$$

$$\delta\theta_x:(a_{55}+\tilde{a}_7)(\theta_x + v_o') - (a_{52}+\tilde{a}_8)\theta_y' + \tilde{a}_4u_o'' - (a_{33}+\tilde{a}_2)\theta_x'' + (a_{43}+\tilde{a}_2)(\theta_y'$$
$$-u_o'') + \tilde{a}_9v_o''' - \tilde{a}_{32}v_o'' + \tilde{a}_{34}u_o''' - (a_{45}+\tilde{a}_{31})(\theta_y - u_o') + (a_{23}+\tilde{a}_{33})\theta_y'' - (a_{35}$$
$$+\tilde{a}_{30})(\theta_x' + v_o'') + \underset{---}{\ddot{\theta}_x}(I_8 - 2I_4 + I_2) + \underset{---}{\ddot{\theta}_y}(-I_9 + 2I_6 - I_5) + \underset{---}{\ddot{v}_o'}(I_2 - I_4) \tag{2.49}$$
$$+\ddot{u}_o'(I_5 - I_6) + \underline{2\Omega(I_8 - I_4)\dot{\phi}} - \Omega^2[\theta_x(I_8 - 2I_4 + I_2) + \theta_y(-I_9 + 2I_6 - I_5)$$
$$+v_o'(I_2 - I_4) + u_o'(I_5 - I_6)] = 0$$

$$\delta\theta_y:(a_{44}+\tilde{a}_1)(\theta_y - u_o') - (a_{43}+\tilde{a}_2)\theta_x' + \tilde{a}_3v_o'' - (a_{22}+\tilde{a}_{11})\theta_y'' + (a_{52}+\tilde{a}_8)(\theta_x'$$
$$+v_o'') + (a_{42}-\tilde{a}_{30})\theta_y' - \tilde{a}_{32}u_o'' - (a_{45}+\tilde{a}_{31})(\theta_x + v_o') + (a_{23}+\tilde{a}_{33})\theta_x'' - (a_{24}$$
$$-\tilde{a}_{30})(\theta_y' - u_o'') + \tilde{a}_{34}v_o''' + \tilde{a}_5u_o''' + \underset{---}{\ddot{\theta}_y}(I_7 - 2I_3 + I_1) + \underset{---}{\ddot{u}_o'}(I_3 - I_1) + \underset{---}{\ddot{\theta}_x}(-I_9 \tag{2.50}$$
$$+2I_6 - I_5) + \ddot{v}_o'(I_6 - I_5) + \underline{\underline{2\Omega(I_6 - I_9)\dot{\phi}}} - \Omega^2[\theta_y(I_7 - 2I_3 + I_1) + u_o'(I_3 - I_1)$$
$$+\theta_x(-I_9 + 2I_6 - I_5) + v_o'(I_6 - I_5)] = 0$$

$$\delta\phi:\ a_{66}\phi^{IV} - a_{77}\phi'' - \tilde{a}_{17}w_o'' + (I_8 + I_7)\ddot{\phi} - I_{ww}\ddot{\phi}'' - 2\Omega[\underline{\underline{\dot{\theta}_x(I_8 - I_4) + I_4\dot{v}_o' + \dot{\theta}_y(I_6}}$$
$$\underline{\underline{-I_9) - I_6\dot{u}_o'}}] - \Omega^2[I_8\phi - I_{ww}\phi'' + \underline{R_zb_1(I_8 + I_7)\phi''} - I_9] = 0 \tag{2.51}$$

The forced boundary conditions are obtained as,

$$\delta u_o:(a_{43}+\tilde{a}_2)\theta_x' - (a_{42}-\tilde{a}_{30})\theta_y' + (a_{45}+\tilde{a}_{31})(\theta_x + v_o') - (a_{44}+\tilde{a}_1)(\theta_y - u_o')$$
$$+\tilde{a}_3v_o'' - \tilde{a}_{34}\theta_x'' + \tilde{a}_5\theta_y'' - \tilde{a}_6u_o''' - \tilde{a}_4(\theta_x' + v_o'') + \tilde{a}_{32}(\theta_y' - u_o'') - \tilde{a}_{35}v_o''' + I_1\ddot{u}_o'$$
$$+\ddot{\theta}_y(I_3 - I_1) + I_5\ddot{v}_o' + \ddot{\theta}_x(I_5 - I_6) + 2\Omega I_6\dot{\phi} - \Omega^2[I_1u_o' + \theta_y(I_3 - I_1) + I_5v_o' \tag{2.52}$$
$$+\theta_x(I_5 - I_6) + R_zb_1u_o'] = 0$$

$$\delta u_o':\tilde{a}_{34}\theta_x' - \tilde{a}_5\theta_y' + \tilde{a}_6u_o'' + \tilde{a}_4(\theta_x + v_o') + \tilde{a}_{32}(\theta_y - u_o') + \tilde{a}_{35}v_o'' = 0 \tag{2.53}$$

$$\delta v_o : (a_{35}+\tilde{a}_{30})\theta_x^{'} - (a_{52}+\tilde{a}_8)\theta_y^{'} + (a_{55}+\tilde{a}_7)(\theta_x + v_o^{'}) + (a_{45}+\tilde{a}_{31})(-\theta_y + u_o^{'}) + \tilde{a}_4 u_o^{''} - \tilde{a}_9\theta_x^{''} + \tilde{a}_{34}\theta_y^{''} + \tilde{a}_{32}(\theta_x^{'} + v_o^{''}) - \tilde{a}_3(-\theta_y^{'} + u_o^{''}) - \tilde{a}_{35}u_o^{'''} - \tilde{a}_{10}v_o^{'''} + I_2\ddot{v}_o^{'} + \ddot{\theta}_x(I_2 - I_4) + I_5\ddot{u}_o^{'} + \ddot{\theta}_y(I_6 - I_5) + 2\Omega\dot{\phi} - \Omega^2[I_2 v_o^{'} + \theta_x(I_2 - I_4) + I_5 u_o^{'} + \theta_y(I_6 - I_5) - R_z b_1 v_o^{'}] = 0 \quad (2.54)$$

$$\delta v_o^{'} : \tilde{a}_9\theta_x^{'} - \tilde{a}_{34}\theta_y^{'} - \tilde{a}_{32}(\theta_x + v_o^{'}) + \tilde{a}_3(-\theta_y + u_o^{'}) + \tilde{a}_{35}u_o^{''} + \tilde{a}_{10}v_o^{''} = 0 \quad (2.55)$$

$$\delta w_o : a_{11}w_o^{'} + a_{17}\phi^{'} = 0 \quad (2.56)$$

$$\delta\theta_x : (a_{33}+\tilde{a}_{12})\theta_x^{'} - (a_{23}+\tilde{a}_{33})\theta_y^{'} + (a_{35}+\tilde{a}_{30})(\theta_x + v_o^{'}) - (a_{43}+\tilde{a}_2)(\theta_y - u_o^{'}) + \tilde{a}_{34}u_o^{''} + \tilde{a}_9 v_o^{''} = 0 \quad (2.57)$$

$$\delta\theta_y : (a_{22}+\tilde{a}_{11})\theta_y^{'} - (a_{23}+\tilde{a}_{33})\theta_x^{'} - (a_{52}+\tilde{a}_8)(\theta_x + v_o^{'}) + (a_{24}-\tilde{a}_{30})(\theta_y - u_o^{'}) - \tilde{a}_5 u_o^{''} - \tilde{a}_{34}v_o^{''} = 0 \quad (2.58)$$

$$\delta\phi : a_{77}\phi^{'} + \tilde{a}_{17}w_o^{'} - a_{66}\phi^{'''} + I_{ww}\ddot{\phi}^{'} + \Omega^2(-I_{ww}\phi^{'} + R_z b_1(I_{xx}+I_{yy})\phi^{''}) = 0 \quad (2.59)$$

$$\delta\phi^{'} : a_{66}\phi^{''} \quad (2.60)$$

where, $R(z) = R_o(L-z) + 0.5(L^2 - z^2)$. Global stiffness quantities a_{ij} and $\tilde{a}_i$ for pretwisted beam are defined in Appendix B and inertia quantities are defined in Appendix C.

2.4 Comments on the equations of motion

The underlined terms in the equations of motion are centrifugal stiffening terms. Song and Librescu (1997) captured centrifugal stiffening effect using geometrically nonlinear modelling method. In their approach, a set of nonlinear equations of motion are derived. Neglecting gyroscopic coupling and making use of suitable assumptions nonlinear extension equation of motion is decoupled and integrated to obtain axial force. The axial force is substituted in the equations of motion to obtain centrifugal stiffening effect.

However in the present method, a non-Cartesian deformation variable representing axial stretch, along with two Cartesian variables is used for the analysis. Due to this transformation, centrifugal stiffening and gyroscopic coupling

effects can be captured in potential and kinetic energy equations respectively. This makes the formulation less cumbersome compared to geometrically nonlinear modelling method. Moreover, this method provides the advantage of inclusion of gyroscopic coupling. The effect of gyroscopic coupling makes the structural model more realistic. The effects of gyroscopic coupling and centrifugal stiffening on the free vibration are highlighted in the Chapter 3.

Table 2.1 Coupling present in the derived un-twisted rotating beam equations of motion

	u_o	v_o	$\hat{s}$	θ_x	θ_y	Φ
u_o	---------	Stiffness	Gyroscopic coupling	Stiffness	Stiffness, Centrifugal acceleration, Rotary inertia	---------
v_o	Stiffness	---------	---------	Stiffness, Centrifugal acceleration, Rotary inertia	Stiffness	Gyroscopic coupling
$\hat{s}$	Gyroscopic coupling	---------	---------	---------	---------	Stiffness
θ_x	Stiffness	Stiffness, Centrifugal acceleration, Rotary inertia	---------	---------	Stiffness	---------
θ_y	Stiffness, Centrifugal acceleration, Rotary inertia	Stiffness	---------	Stiffness	---------	Gyroscopic coupling
Φ	---------	Gyroscopic coupling	Stiffness	Gyroscopic coupling	---------	---------

From the equations of motion, it can be observed that all the equations of governing system are coupled. Underlined terms proportional to Ω in the Eqs. 2.23 – 2.28 and Eqs. 2.46 – 2.51 represent gyroscopic terms and double underlined terms represent centrifugal stiffening terms. Centrifugal stiffening terms appear in equation of motion as $R_z\Omega^2$ and centrifugal force terms appear as Ω^2. Similarly, terms with a_{ij} $(i \neq j)$ represent stiffness coupling and dotted underlined terms

represent rotary inertia. The coupling existing between the different motions for un-twisted and pretwisted rotating beam are tabulated in Table 2.1 and Table 2.2 respectively. Compared to un-twisted beam, the pretwisted beam is highly coupled. Double underlined terms in the equations of motion are gyroscopic coupling terms. $u_o - w_o$, $u_o - \phi$, $v_o - \phi$, $\theta_x - \phi$ and $\theta_y - \phi$ motions are coupled with gyroscopic terms. Gyroscopic couplings $u_o - \phi$ and $\theta_y - \phi$ arise due to pretwist. Depending on the composite ply angle, lay up orientation and for untwisted beam, many constants in the governing system vanish, resulting in decoupling. It can be observed that for a beam configuration of $\theta = 0^o$ or $\theta = 90^o$, $\beta = 0^o$, $\gamma = 0^o$ and $\eta = 1$, structural coupling between $u_o - v_o$, $u_o - \theta_x$ and $u_o - \phi$ vanishes. Consequently, the governing system of equations decouple into two subsystems representing motions $u_o - w_o - \theta_y$ and $v_o - \theta_x - \phi$.

Table 2.2 Coupling present in the derived pretwisted rotating beam equations of motion

	u_o	v_o	$\hat{s}$	θ_x	θ_y	Φ
u_o	---------	Stiffness, Centrifugal acceleration, Rotary inertia	Gyroscopic coupling	Stiffness, Centrifugal acceleration, Rotary inertia	Stiffness, Centrifugal acceleration, Rotary inertia	Gyroscopic coupling
v_o	Stiffness, Centrifugal acceleration, Rotary inertia	---------	---------	Stiffness, Centrifugal acceleration, Rotary inertia	Stiffness, Centrifugal acceleration, Rotary inertia	Gyroscopic coupling
$\hat{s}$	Gyroscopic coupling	---------	---------	---------	---------	Stiffness
θ_x	Stiffness, Centrifugal acceleration, Rotary inertia	Stiffness, Centrifugal acceleration, Rotary inertia	---------	---------	Stiffness, Centrifugal acceleration, Rotary inertia	Gyroscopic coupling
θ_y	Stiffness, Centrifugal acceleration, Rotary inertia	Stiffness, Centrifugal acceleration, Rotary inertia	---------	Stiffness, Centrifugal acceleration, Rotary inertia	---------	Gyroscopic coupling
Φ	Gyroscopic coupling	Gyroscopic coupling	Stiffness	Gyroscopic coupling	Gyroscopic coupling	---------

2.5 Chapter summary

In this Chapter, the governing equations for vibration of rotating composite cantilever beam using dynamic modelling method are presented. The effect of higher shear deformation theory is included in the structural model. The variational strain energy and kinetic energy equations are derived. The equations of motion for rotating beams with boundary conditions are obtained using Hamilton's principle. It has been shown that dynamic modelling method simplifies the formulation procedure as compared to geometrically non-linear modelling method. In Chapter 3, the equations of motion presented in this chapter are used to study the free and forced vibration behaviour of rotating beams.

Chapter 3

Vibration analysis of rotating beams

3.1 Introduction

As mentioned in Chapter 1, rotating blades are flexible structures, which have practical applications in turbo machines, helicopter blades, robot manipulators, compressor blades, windmill turbine blades, spinning space structures, propeller blades etc. In this chapter the equations of motion presented in Chapter 2 have been solved for vibration analysis of rotating composite beams. In the solution procedure gyroscopic coupling is included. Effects of pretwist, presetting, taper, ply angle orientation and gyroscopic coupling on the free and forced vibration are highlighted.

3.2 Approximate solution using extended Galerkin's method

In the present study, extended Galerkin's method is used to obtain the approximate solution. In this approach discretization is carried out within the Hamilton's equation. The natural boundary conditions are taken back into the variational equation by carrying out reverse integration in space. Hence, only geometric boundary conditions appear as boundary terms. Thus $u_o = \varphi_1 q_1$, $v_o = \varphi_2 q_2$, $w_o = \varphi_3 q_3$, $\theta_x = \varphi_4 q_4$, $\theta_y = \varphi_5 q_5$ and $\phi = \varphi_6 q_6$, where, $\varphi_i(z)$ and $q_i(t)$ are vectors of trial function which satisfy geometric boundary conditions and generalized coordinates respectively. Upon substituting these quantities, the equations of motion can be written in the matrix form as,

$$M\ddot{q} + G_c\dot{q} + Kq = F_{CF} + R(t) \tag{3.1}$$

where $F_{CF}\left(=\int_0^L 2b_1\Omega^2(R_o+z)\mathrm{d}z\right)$ and $R(t)$ are centrifugal force vector and arbitrary excited load respectively and K, M and G matrices are as follows:

$$K=\int_0^L\begin{bmatrix} K_{11} & K_{12} & 0 & K_{14} & K_{15} & 0\\ K_{12} & K_{22} & 0 & K_{24} & K_{25} & 0\\ 0 & 0 & K_{33} & 0 & 0 & K_{36}\\ K_{14} & K_{24} & 0 & K_{44} & K_{45} & 0\\ K_{15} & K_{25} & 0 & K_{45} & K_{55} & 0\\ 0 & 0 & K_{36} & 0 & 0 & K_{66}\end{bmatrix}\mathrm{d}z \tag{3.2}$$

$$M=\int_0^L\begin{bmatrix} M_{11} & M_{12} & 0 & M_{14} & M_{15} & 0\\ M_{12} & M_{22} & 0 & M_{24} & M_{25} & 0\\ 0 & 0 & M_{33} & 0 & 0 & M_{36}\\ M_{14} & M_{24} & 0 & M_{44} & M_{45} & 0\\ M_{15} & M_{25} & 0 & M_{45} & M_{55} & 0\\ 0 & 0 & M_{36} & 0 & 0 & M_{66}\end{bmatrix}\mathrm{d}z \tag{3.3}$$

$$G=\int_0^L\begin{bmatrix} 0 & 0 & G_{13} & 0 & 0 & G_{16}\\ 0 & 0 & 0 & 0 & 0 & G_{26}\\ -G_{13} & 0 & 0 & 0 & 0 & 0\\ 0 & 0 & 0 & 0 & 0 & G_{46}\\ 0 & 0 & 0 & 0 & 0 & G_{56}\\ G_{-16} & -G_{26} & 0 & -G_{46} & -G_{56} & 0\end{bmatrix}\mathrm{d}z \tag{3.4}$$

where, the components of stiffness matrix are obtained as,

$$\begin{aligned}
K_{11} &= \tilde{a}_{32}\phi_1''\phi_1''^{T}+\tilde{a}_6\phi_1''\phi_1''^{T}+\left(a_{44}+\tilde{a}_1\right)\phi_1'\phi_1'^{T}-\Omega^2\left[b_1\phi_1\phi_1^{T}-b_1R_2\phi_1'\phi_1'^{T}+I_1\phi_1'\phi_1^{T}\right]\\
K_{12} &= \left(a_{45}+\tilde{a}_{31}\right)\phi_1'\phi_2'^{T}+\tilde{a}_3\phi_1'\phi_2'''^{T}+\tilde{a}_4\phi_1''\phi_2'^{T}+\tilde{a}_{35}\phi_1''\phi_2''^{T}-\Omega^2\left[I_5\phi_1'\phi_2'^{T}\right]\\
K_{14} &= \left(a_{34}+\tilde{a}_2\right)\phi_1'\phi_4'^{T}+\left(a_{45}+\tilde{a}_{31}\right)\phi_1'\phi_4'^{T}+\tilde{a}_{34}\phi_1''\phi_4'^{T}+\tilde{a}_4\phi_1''\phi_4^{T}-\Omega^2\left[-I_6\phi_1'\phi_4^{T}+I_5\phi_1'\phi_4^{T}\right]
\end{aligned} \tag{3.5}$$

$$K_{15} = -\left(a_{42} + \tilde{a}_{30}\right)\phi_1'\phi_5'^T - \left(a_{44} + \tilde{a}_1\right)\phi_1'\phi_5^T - \tilde{a}_5\phi_1''\phi_5'^T - \tilde{a}_{32}\phi_1''\phi_5^T - \Omega^2\left[I_3\phi_1'\phi_5^T - I_1\phi_1'\phi_5^T\right]$$

$$K_{22} = \left(a_{55} + \tilde{a}_7\right)\phi_2'\phi_2'^T - \tilde{a}_{32}\phi_2'\phi_2''^T + \tilde{a}_{10}\phi_2''\phi_2''^T - \Omega^2\left[I_2\phi_2'\phi_2'^T - b_1R_2\phi_2'\phi_2'^T\right]$$

$$K_{24} = \left(a_{35} + \tilde{a}_{30}\right)\phi_2'\phi_4'^T + \left(a_{55} + \tilde{a}_7\right)\phi_2'\phi_4'^T + \tilde{a}_9\phi_2''\phi_4'^T - \tilde{a}_{32}\phi_2''\phi_4^T - \Omega^2\left[-I_4\phi_2'\phi_4^T + I_2\phi_2'\phi_4^T\right]$$

$$K_{25} = -\left(a_{52} + \tilde{a}_8\right)\phi_2'\phi_5'^T - \left(a_{45} + \tilde{a}_{31}\right)\phi_2'\phi_5^T - \tilde{a}_{34}\phi_2''\phi_4'^T - \tilde{a}_3\phi_2''\phi_5^T - \Omega^2\left[I_6\phi_2'\phi_5^T - I_5\phi_2'\phi_5^T\right]$$

$$K_{33} = \tilde{a}_{11}^P\phi_3'\phi_3'^T - \Omega^2\left[b_1\phi_3\phi_3^T\right]$$

$$K_{36} = \tilde{a}_{17}^P\phi_3'\phi_6'^T$$

$$K_{44} = \left(a_{35} + \tilde{a}_{30}\right)\phi_4\phi_4'^T + \left(a_{55} + \tilde{a}_7\right)\phi_4\phi_4^T + \left(a_{33} + \tilde{a}_{12}\right)\phi_4'\phi_4'^T - \Omega^2\left[\left(I_8 - 2I_4 + I_2\right)\phi_4\phi_4^T\right]$$

$$K_{45} = -\left(a_{25} + \tilde{a}_8\right)\phi_4\phi_5'^T - \left(a_{45} + \tilde{a}_{31}\right)\phi_4\phi_5^T - \left(a_{23} + \tilde{a}_{33}\right)\phi_4'\phi_5' - \left(a_{34} + \tilde{a}_2\right)\phi_4'\phi_5^T$$
$$- \Omega^2\left[\left(-I_9 + 2I_6 - I_5\right)\phi_4\phi_5^T\right]$$

$$K_{55} = \left(a_{42} - \tilde{a}_{30}\right)\phi_5\phi_5'^T + \left(a_{44} + \tilde{a}_1\right)\phi_5\phi_5^T + \left(a_{22} + \tilde{a}_{11}\right)\phi_5'\phi_5'^T - \Omega^2\left[\left(I_7 - 2I_3 + I_1\right)\phi_5\phi_5^T\right]$$

$$K_{66} = a_{77}^P\phi_6'\phi_6'^T + a_{66}^P\phi_6''\phi_6''^T - \Omega^2\left[\left(I_8 - I_7\right)\phi_6\phi_6^T + I_{ww}\phi_6'\phi_6'^T - R_2\left(I_8 + I_7\right)\phi_6'\phi_6'^T\right]$$

The components of mass matrix are,

$$M_{11} = b_1\phi_1\phi_1^T + I_1\phi_1'\phi_1'^T \qquad M_{25} = I_6\phi_2'\phi_5^T - I_5\phi_2'\phi_5^T$$

$$M_{12} = I_5\phi_1'\phi_2'^T \qquad M_{33} = b_1\phi_3\phi_3^T$$

$$M_{14} = -I_6\phi_1'\phi_4^T + I_5\phi_1'\phi_4^T \qquad M_{44} = \left(I_8 - 2I_4 + I_2\right)\phi_4\phi_4^T$$

$$M_{15} = I_3\phi_1'\phi_5^T - I_1\phi_1'\phi_5^T \qquad M_{45} = \left(-I_9 + 2I_6 - I_5\right)\phi_4\phi_5^T \qquad (3.6)$$

$$M_{22} = b_1\phi_2\phi_2^T + I_2\phi_2'\phi_2'^T \qquad M_{55} = \left(I_7 - 2I_3 + I_1\right)\phi_5\phi_5^T$$

$$M_{24} = -I_4\phi_2'\phi_4^T + I_2\phi_2'\phi_4^T \qquad M_{66} = \left(I_8 + I_7\right)\phi_6\phi_6^T + I_{ww}\phi_6'\phi_6'^T$$

Gyroscopic coupling matrix components are obtained as,

$$G_{13} = -2b_1\Omega\phi_1\phi_3^T \qquad G_{46} = 2\Omega\left[-I_8\phi_4\phi_6^T + I_4\phi_4\phi_6^T\right]$$

$$G_{16} = 2\Omega I_6\phi_1'\phi_6^T \qquad G_{56} = 2\Omega\left[I_9\phi_5\phi_6^T - I_6\phi_5\phi_6^T\right] \qquad (3.7)$$

$$G_{26} = 2\Omega I_4\phi_2'\phi_6^T$$

3.3 Free vibration studies

For free vibration analysis, the forcing term in Eq. (3.1) is neglected. The eigen solution of Eq. (3.1) in exponential form is written as $q = e^{i\omega t} X$, where ω is a constant scalar and X is a constant vector, which is in general complex. For a conservative gyroscopic system, the eigen value problem is written as,

$$AX = \lambda X$$

where

$$A = \begin{bmatrix} 0 & I \\ -M^{-1}K & -M^{-1}G \end{bmatrix} \tag{3.8}$$

Here, $\omega = \sqrt{\lambda}$, is the natural frequency.

3.4 Time response

Newmark's direct integration method is employed to obtain time responses of rotating beams. The Newmark method uses the following finite difference approximations [Bathe and Wilson (1976)]

$$\ddot{q}_{t+\Delta t} = a_o(q_{t+\Delta t} - q_t) - a_2\dot{q}_t - a_3\ddot{q}_t \tag{3.9}$$

$$\dot{q}_{t+\Delta t} = \dot{q}_t + a_6\ddot{q}_t + a_7\ddot{q}_{t+\Delta t} \tag{3.10}$$

These are substituted into system equation (3.1) and solved for the unknown displacements $q_{t+\Delta t}$. This results in the following system of linear of equations

$$\hat{K}q_{t+\Delta t} = \hat{R}_{t+\Delta t}$$

where

$$\hat{K} = K + a_o M + a_1 G_c \tag{3.11}$$

$$\hat{R} = \hat{R}_{t+\Delta t} + M(a_o q_t + a_2\dot{q}_t + a_3\ddot{q}_t) + G_c(a_1 q_t + a_4\dot{q}_t + a_5\ddot{q}_t)$$

$$a_o = \frac{1}{\alpha \Delta t^2};\quad a_1 = \frac{\delta}{\alpha \Delta t};\quad a_2 = \frac{1}{\alpha \Delta t};\quad a_3 = \frac{1}{\alpha \Delta t^2} - 1;\quad a_4 = \frac{\delta}{\alpha \Delta t} - 1;$$

$$a_5 = \frac{\Delta t}{2}\left(\frac{\delta}{\alpha} - 2\right);\quad a_6 = \Delta t\left(1 - \delta\right);\quad a_7 = \delta \Delta t;$$

Parameters α and δ can be varied to obtain optimum integration accuracy and stability. In the present study, the time step of 0.0001 sec with $\alpha = 0.75$ and $\delta = 0.5$ is taken in the analysis.

3.5 Convergence study and comparison with available predictions

The beam considered in the numerical analysis is composed of graphite-epoxy material with properties $E_1 = 206.8$ GPa; $E_2 = 5.17$ GPa; $G_{12} = G_{13} = 3.1$ GPa; $G_{23} = 2.5511$ GPa; $\gamma_{12} = 0.25$; $\rho = 1528.15$ kg/m^3, with beam geometric configuration (Figure 2.1) $L = 2.023$ m; $R_o = 0.2023$ m; $h = 0.01016$ m; $c = 0.127$ m; $b = 0.0254$ m. The vectors of trial functions selected to satisfy geometric boundary conditions at the beam root ($z = 0$) are

$$\begin{aligned} &\varphi_1 = [z^2\ z^3 ....], \quad \varphi_2 = [z^2\ z^3 ....], \quad \varphi_3 = [z\ z^2 ....], \\ &\varphi_4 = [z\ z^2 ....], \quad \varphi_5 = [z\ z^2 ....], \quad \varphi_6 = [z^2\ z^3 ....]) \end{aligned} \tag{3.12}$$

Convergence study is carried out by increasing the order of vectors in trial functions in Eq. (3.12). Table 3.1 shows the first three natural frequencies for a 30^o ply angle, pretwist angle of 30^o, preset angle of 0^o and rotational speed of 200 rad/s. From the present study it is found that for the convergence of first three natural frequencies, a minimum order of trial functions vector required is ten. Hence further analysis is carried out using ten term vectors in trial function.

To validate the developed code, the results obtained from the present method are compared with the experimental and theoretical results of Chandra and Chopra (1992) for graphite epoxy beam and are shown in Table. 3.2. For validation, material properties

considered are $E_1 = 141.93$ GPa; $E_2 = 9.788$ GPa; $G_{12} = 6.135$ GPa; $\rho = 1444.8$ kg/m^3, with beam geometric configuration (Figure 2.1) $L =$ 0.84455 m; $R_o =$ 0.06985 m; $h =$ 0.762 mm; $c =$ 11.4046 mm; $b = 6.8834$ mm; $k = 6$ and $\theta = 30^o$. It can be observed that the present results are in good agreement with the experimental results. Furthermore, the results obtained by the present method are in close agreement with the theoretical results obtained by Chandra and Chopra (1992).

Table 3.1. Convergence of natural frequencies

Vectors of trial function	First	Second	Third
1	332.48	349.75	1383.95
2	279.03	320.19	1252.68
3	272.31	313.62	1203.84
4	271.31	310.73	1191.22
5	271.19	309.65	1184.3
6	271.19	309.28	1180.75
7	271.19	309.17	1178.48
8	271.19	309.15	1177.3
9	271.19	309.14	1176.54
10	271.19	309.14	1176.17

Table 3.2 Comparison of natural frequencies with experimental results [Chandra and Chopra (1992)]

	Rotational speed (rad/s)	Chandra and Chopra (1992)		Present	% deviation from experimental results
		Expt.	Theory		
Flap I	0	21.1	19.8	19.84	5.97
	1000	28.3	26.8	26.15	7.59
Lag I	0	37.6	37.1	36.35	3.32
	1000	39.1	37.5	38.05	2.68
Flap II	0	127.8	124.2	129.6	1.39
	1000	134.9	131	138.17	2.37

Table 3.3 demonstrates the comparison of first three natural frequencies for four values of presetting angle and four values of rotational speed with the results of Oh et al. (2003). The beam is composed of graphite-epoxy material with properties $E_1 = 206.8$ GPa; $E_2 = 5.17$ GPa; $G_{12} = G_{13} = 3.1$ GPa; $G_{23} = 2.5511$ GPa; $\gamma_{12} = 0.25$; $\rho = 1528.15$ kg/m^3, with beam geometric configuration $L = 2.023$ m; $R_o = 0.1$ m; $h = 0.01016$ m; $c = 0.127$ m; $b = 0.0254$ m. The analysis is performed for a 0^o ply angle, 30^o pretwist angle and ignoring gyroscopic coupling.

Table 3.3 Comparison of first three natural frequencies with Reference [Oh et al. (2003)]

Rotational speed	Presetting angle	Present			Reference [Oh et. al (2003)]		
		ω_1	ω_2	ω_3	ω_1	ω_2	ω_3
Ω=100 rad/s	γ=0°	119.26	143.3	366.21	118.21	145.59	362.00
	γ=30°	98.788	157.83	360.69	98.96	158.98	358.36
	γ=60°	75.021	170.19	354.5	75.01	171.89	350.4
	γ=90°	65.927	173.98	353.82	66.45	175.21	349.37
Ω=200 rad/s	γ=0°	173.24	225.78	570.91	172.92	225.11	586.64
	γ=30°	150.57	241.13	542.32	150.08	241.24	577.11
	γ=60°	118.65	258.09	519.41	118.25	257.88	559.63
	γ=90°	104.88	264.1	526.55	104.79	264.30	550.11
Ω=300 rad/s	γ=0°	209.33	332.83	834.51	206.86	332.25	832.40
	γ=30°	191.27	343.1	810.9	188.81	342.77	815.45
	γ=60°	159.46	358.65	786.96	157.78	358.09	788.44
	γ=90°	144.44	365.04	784.41	143.73	363.50	776.35
Ω=400 rad/s	γ=0°	247.25	440.34	1086.6	241.81	442.20	1085.57
	γ=30°	230.96	448.58	1052.8	226.55	447.90	1059.63
	γ=60°	199.86	462.85	1021.5	196.92	460.82	1023.61
	γ=90°	184.54	469.23	1017.9	182.26	466.54	1009.38

Table 3.4 shows the comparison of first three natural frequencies for various (*c/h*) (beam width to thickness) ratios ignoring the gyroscopic coupling, for a 0^o ply angle and rotational speed of 100 rad/s. It reveals from the table that *c/h* ratio is not having considerable effect on the first three natural frequencies for the considered range of *c/h* ratio. The maximum percentage deviation between the two sets of results is 1.656 for (*c/h*) = 10.

Table 3.4 Comparison of first three natural frequencies for various (*c/h*) ratios

c/h	ω_i	Present	Reference [Chandiramani et. al (2002)]	% deviation
10	ω_1	119.59	119.94	0.295969
	ω_2	143.19	145.60	1.656571
	ω_3	358.92	362.67	1.034544
20	ω_1	119.48	119.83	0.296241
	ω_2	143.18	145.58	1.653982
	ω_3	357.81	361.51	1.025949
30	ω_1	119.46	119.81	0.295458
	ω_2	143.18	145.58	1.651956
	ω_3	357.6	361.30	1.025449
40	ω_1	119.45	119.80	0.297979
	ω_2	143.18	145.58	1.65128
	ω_3	357.53	361.23	1.024278
50	ω_1	119.45	119.80	0.29465
	ω_2	143.18	145.58	1.65128
	ω_3	357.5	361.19	1.022993

The comparisons indicate that the results obtained form the present method is in good agreement with the experimental and theoretical predictions of other researchers.

3.6 Numerical results and analysis

The beam is composed of graphite-epoxy material with properties $E_1 = 206.8$ GPa; $E_2 = 5.17$ GPa; $G_{12} = G_{13} = 3.1$ GPa; $G_{23} = 2.5511$ GPa; $\gamma_{12} = 0.25$; $\rho = 1528.15$ kg/m^3, with beam geometric configuration $L = 2.023$ m; $R_o = 0.1$ m; $h = 0.01016$ m; $c = 0.127$ m; $b = 0.0254$ m. Figure 3.1 shows the lagging, flapping and extension motions of rotating cantilever beam. When the motion is in the direction rotor (X – axis) rotation it is termed as lagging motion. If the motion is vertical to the rotor direction is termed as flapping motion and the motion along the length of the beam is termed as extension.

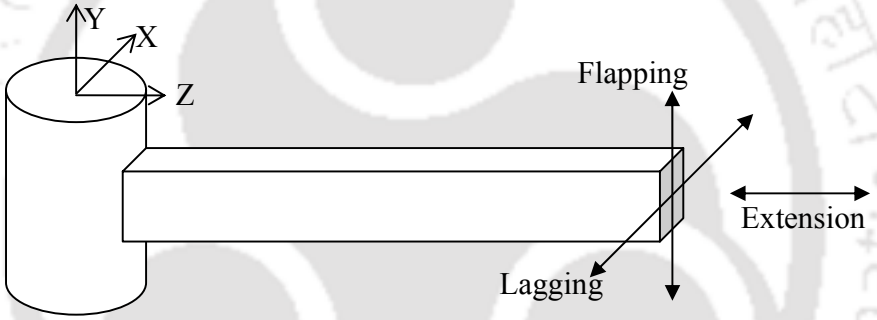

Figure 3.1 Rotating beam flapping,lagging and extension motions

3.6.1 Effect of gyroscopic coupling

The first three normalized eigen modes in lagging, flapping and extension motions for a 30^o ply angle are shown in Figures 3.2, 3.3 and 3.4 respectively. In lagging, flapping and extension modes, the beam gets straightened for a rotating beam. It is because centrifugal stiffening effect (terms associated with *R(z)* in Eqs. 2.46 – 2.51) increases with rotational speed. In lagging motion (Figure 3.2), the gyroscopic coupling effect straightens the beam more compared to the analysis neglecting gyroscopic coupling.

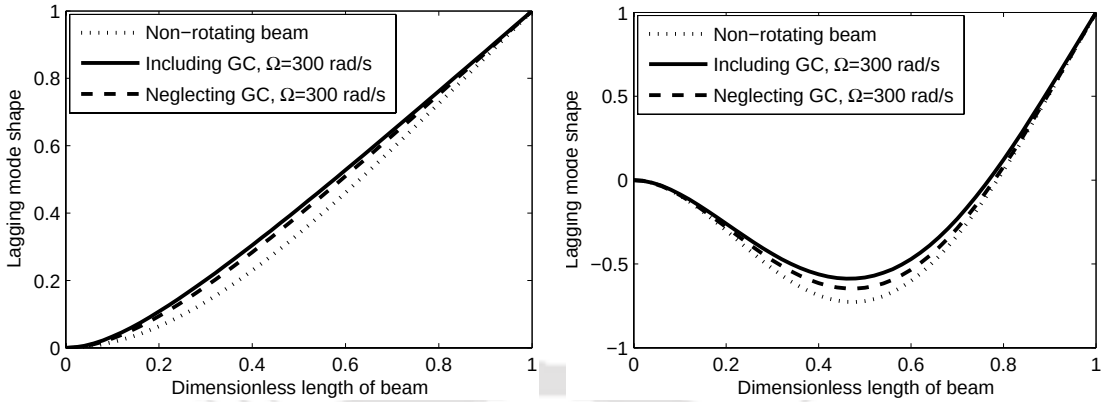

(a) First mode

(b) Second mode

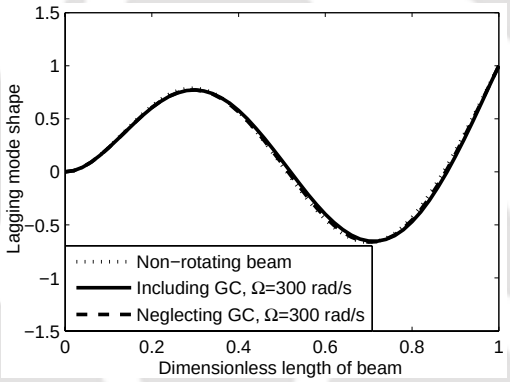

(c) Third mode

Figure 3.2 First three normalized lagging mode shape variations ($\theta = 0^o$, $\beta = 0^o$, $\gamma = 0^o$, $\eta = 1$).

In flapping motion (Figure 3.3), plot with and without gyroscopic coupling are found to coincide. In other words, gyroscopic coupling is not having much effect on flapping mode shapes. It is also observed that the gyroscopic coupling is not having considerable effect on twisting and rotational motion mode shapes. Thus gyroscopic coupling is found to have significant effect on lagging – extension mode shapes only.

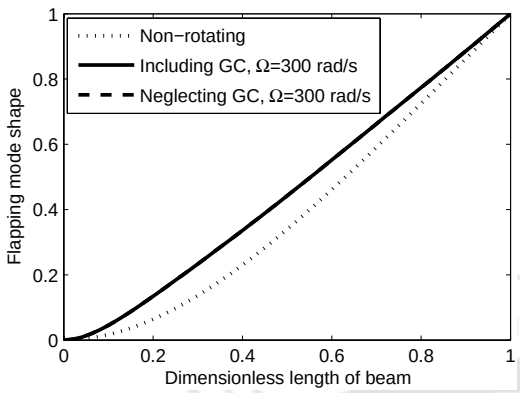

(a) First mode

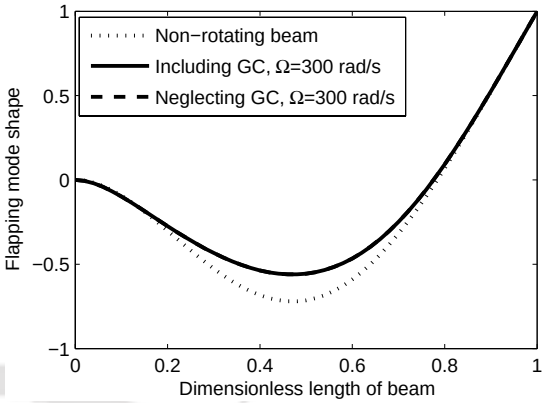

(b) Second mode

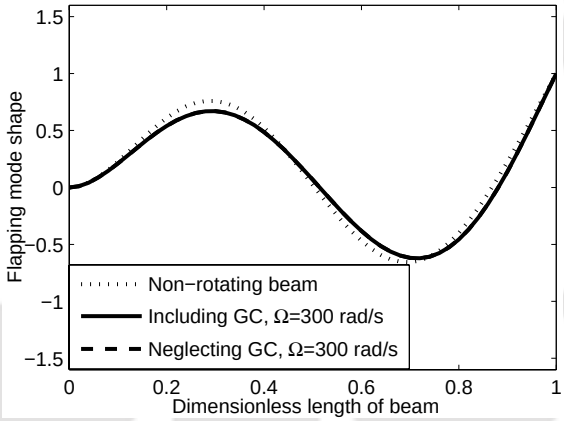

(c) Third mode

Figure 3.3 First three normalized flapping mode shape variations ($\theta = 0^o$, $\beta = 0^o$, $\gamma = 0^o$, $\eta = 1$)

The Figures 3.5(a)-3.5(d) show first four natural frequencies of the coupled lag-extension motion for various rotational speeds and ply angles. The solid lines represent the analysis by including gyroscopic coupling and dotted lines represent the analysis by neglecting gyroscopic coupling. Considerable variation in natural frequencies is observed between the analysis with and without gyroscopic coupling. In the first, second and fourth natural frequencies, gyroscopic coupling has softening effect, whereas in the third natural frequency, gyroscopic coupling has stiffening effect. For smaller values of ply angle ($0^o$to 45^o) the gyroscopic effect is more pronounced and gradually becomes negligible at higher values of ply angle (60^o to 90^o). The effect of

gyroscopic coupling on forced vibration response is shown in Figure 3.6. It is observed that, gyroscopic forces are having a tendency to increase the tip displacement. The effect of gyroscopic coupling on frequency response is shown in Figure 3.7. It is observed that gyroscopic coupling marginally decreases the amplitude of vibration.

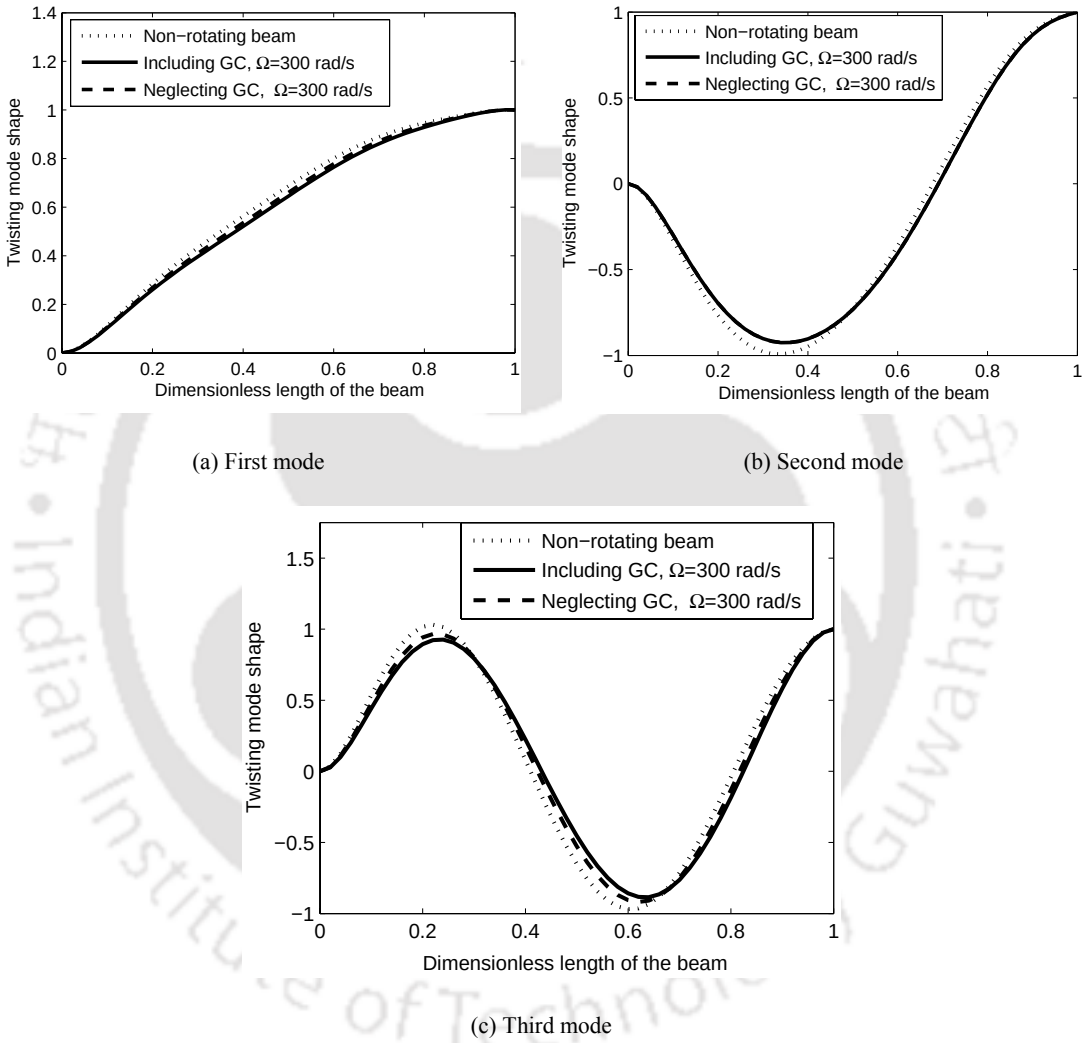

(a) First mode

(b) Second mode

(c) Third mode

Figure 3.4 First three normalized twisting mode shape variations ($\theta = 0^o$, $\beta = 0^o$, $\gamma = 0^o$, $\eta = 1$)

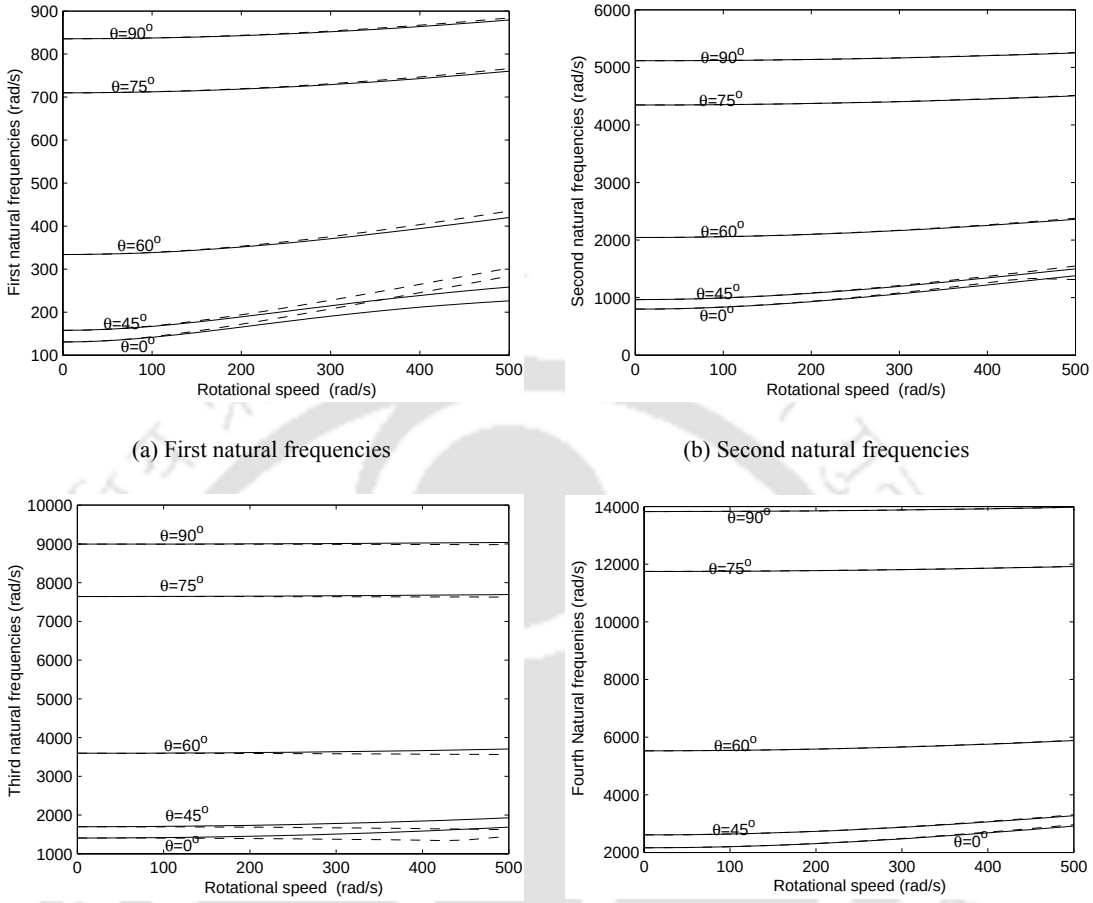

(a) First natural frequencies

(b) Second natural frequencies

(c) Third natural frequencies

(d) Fourth natural frequencies

Figure 3.5 Coupled natural frequencies for various rotational speeds and ply angles

The first three gyroscopically coupled and uncoupled natural frequencies of coupled $u_o - w_o - \theta_y$ motion for various rotational speeds are shown in Figure 3.8. Plot shows that instability occurs for the considered beam configuration at ≈1480 *rad/s*, in other words the dominant first natural frequency becomes zero. It is also observed that at lower rotational speeds, lagging frequencies increase with increase in rotational speed due to centrifugal stiffening effect. At higher rotational speeds gyroscopic coupling dominates and lagging frequencies start decreasing. In the analysis neglecting gyroscopic coupling, the lagging frequencies increase with rotational speed. The extensional natural frequencies increase when gyroscopic coupling is considered and

decreases when gyroscopic coupling is neglected. Hence, it can be concluded that, gyroscopic coupling is having softening effect on lagging natural frequencies and stiffening effect on extensional natural frequencies. Two eigen value loci (II Lag and I ext shown in Figure 3.8 at marker I) and (III Lag and II Ext shown in Figure 3.8 at marker II) veer (divergence of two root loci [Yoo, *et al.* (1998)]) at ≈ 430 rad/s and ≈ 925 rad/s respectively. Normalized mode shape variation of II lagging and I extension mode at veering I region is plotted in Figure 3.9. Similarly, Figure 3.10 shows mode shape variation at veering II region of III lagging and II extension mode. Since, in veering region energy exchanges between the eigen modes, abrupt changes in mode shape for small change in rotational speed is observed.

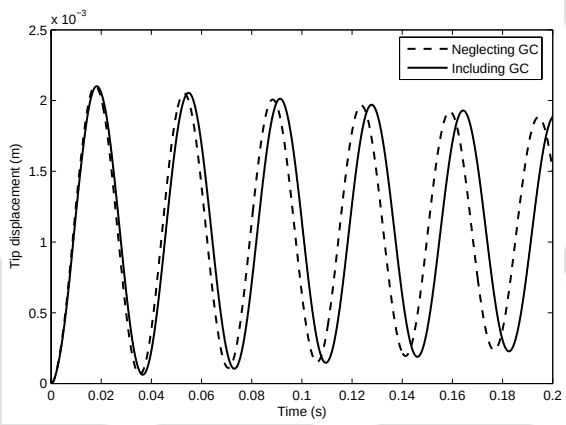

Figure 3.6 Effect of gyroscopic coupling on forced vibration ($\theta = 0^o$, $\beta = 0^o$, $\gamma = 0^o$, $\eta = 1$, $\Omega = 200$ rad/s)

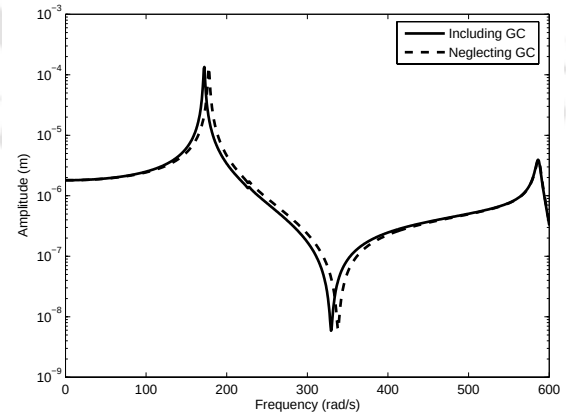

Figure 3.7 Effect of gyroscopic coupling on frequency response ($\theta = 0^o$, $\beta = 0^o$, $\gamma = 0^o$, $\eta = 1$, $\Omega = 200$ rad/s)

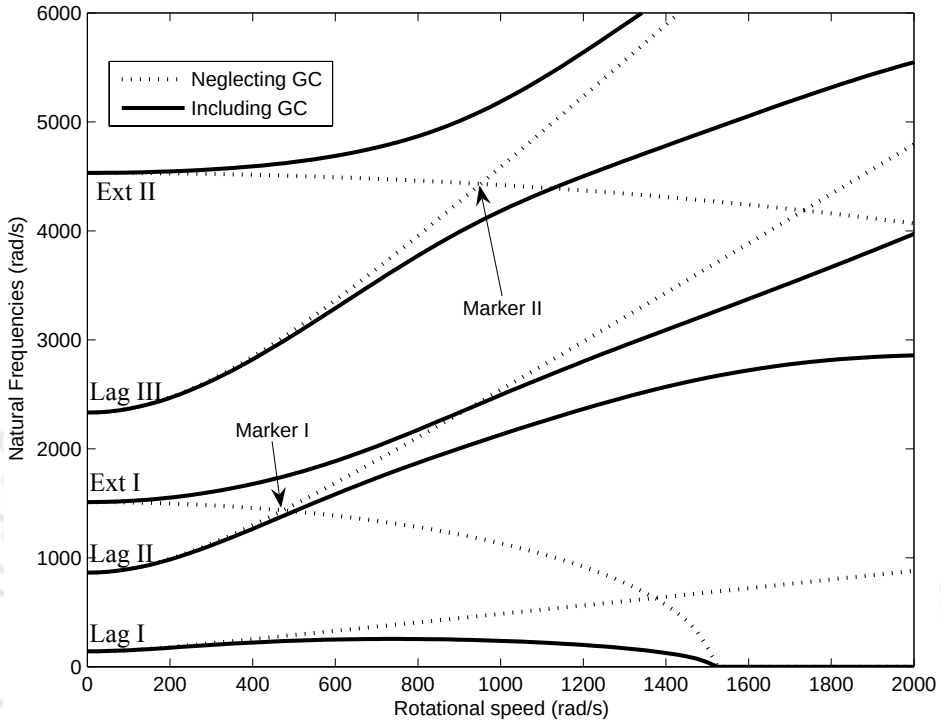

Figure 3.8 Effect of gyroscopic coupling on first five natural frequencies on lagging – extension coupled motion ($\theta = 0^o$, $\beta = 0^o$, $\gamma = 0^o$, $\eta = 1$)

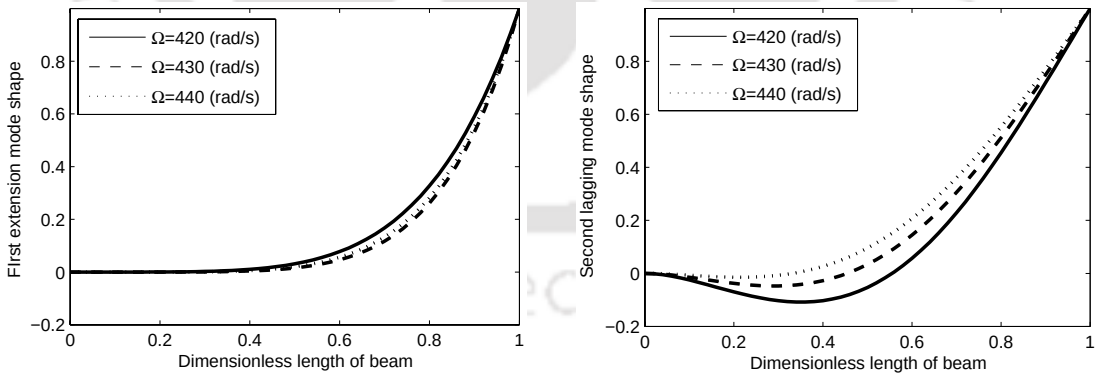

(a) First extension mode

(b) Second lagging mode

Figure 3.9 Normalized mode shape variation at I veering region

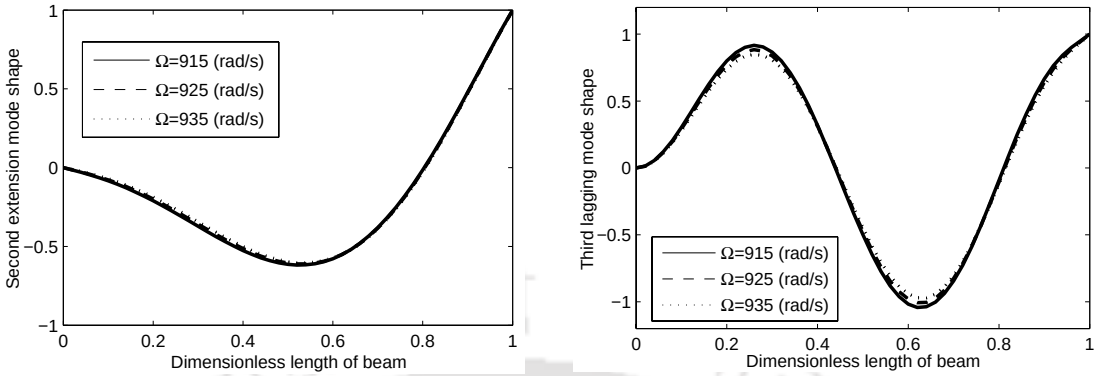

(a) Second extension mode (b) Third lagging mode

Figure 3.10 Normalized mode shape variation at II veering region

3.6.2 Effect of taper

The first three normalized eigen modes in lagging and flapping motion for taper parameter (η) varying from 1 to 4 are shown in Figures 3.11 and 3.12 respectively. In the second and third modes (Figures 3.11 (b) – (c) and 3.12 (b) – (c)) increase in beam taper straightens the beam; where as in the first mode (Figures 3.11 (a) and 3.12 (a)) increase in beam taper bends itself more.

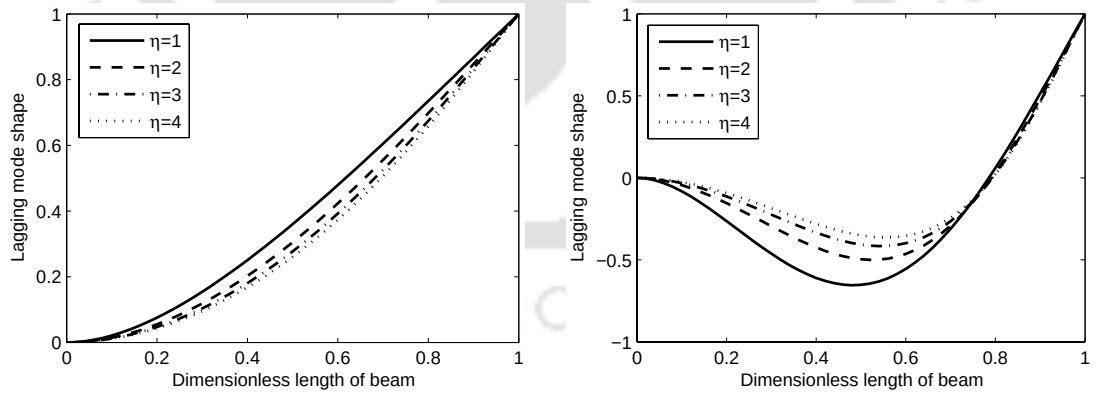

(a) First mode (b) Second mode

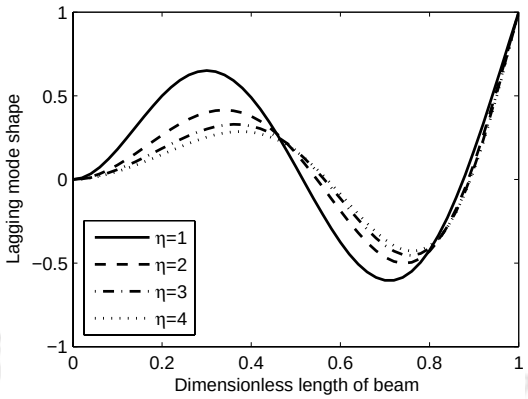

(c) Third mode

Figure 3.11 Normalized lagging mode shape for various taper parameters

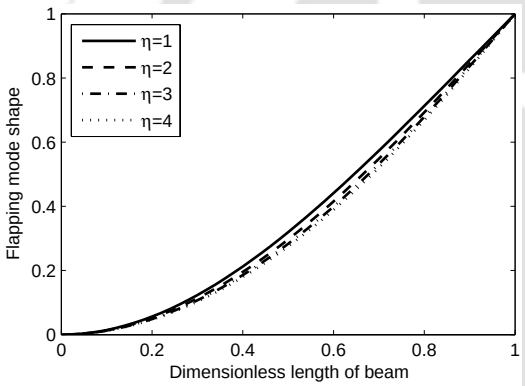

(a) First mode

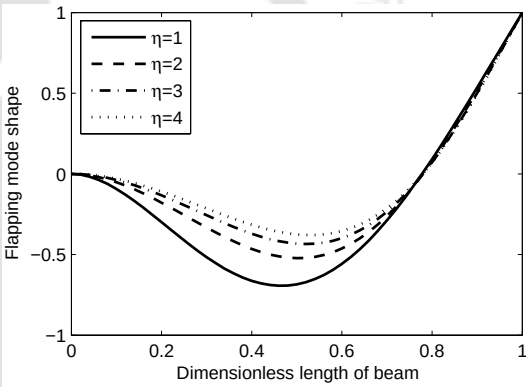

(b) Second mode

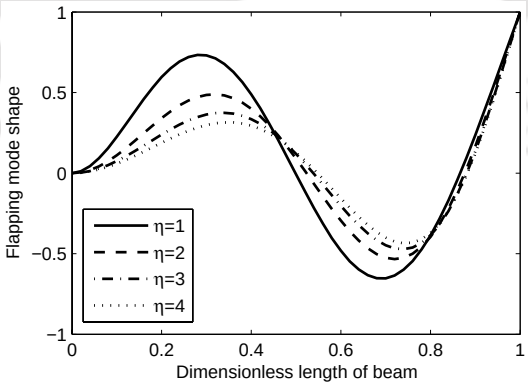

(c) Third mode.

Figure 3.12 Normalized flapping mode shape for various taper parameters

In Figure 3.13, the first four coupled natural frequencies for various rotational speeds and taper parameters are illustrated. It is observed that a tapered beam increases the first two natural frequencies (Figures 3.13 (a) – (b)) and decreases the third and fourth natural frequencies (Figures 3.13 (c) – (d)). It is also seen that as the rotational speed increases, the natural frequency also increases and stiffens the beam. Stiffening is more pronounced at higher rotational speeds because of combined effect of taper and centrifugal stiffening. It is also observed that for the first two natural frequencies as the rotational speed increases, the dominant motion changes from flap to lag and vice versa.

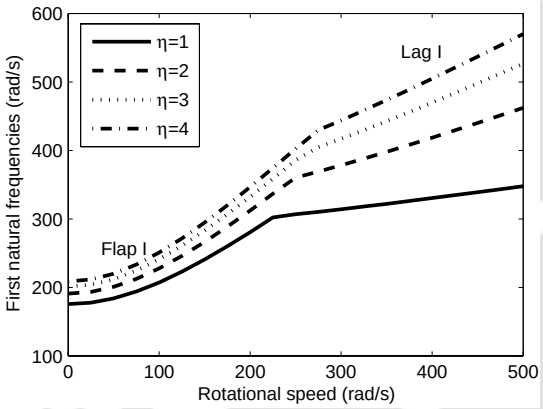

(a) First natural frequencies

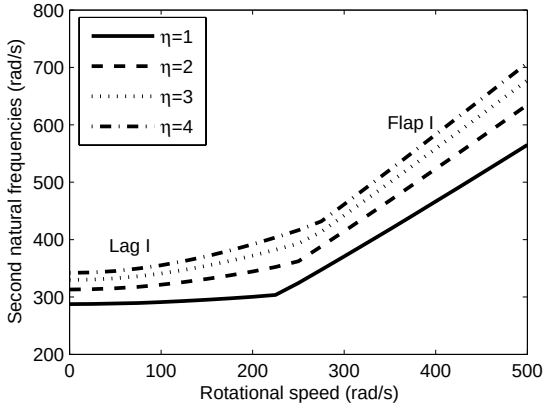

(b) Second natural frequencies

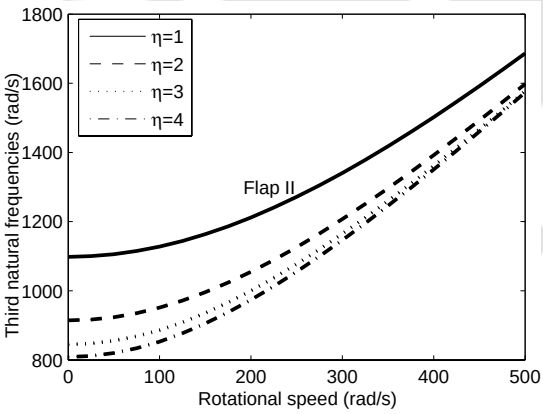

(c) Third natural frequencies

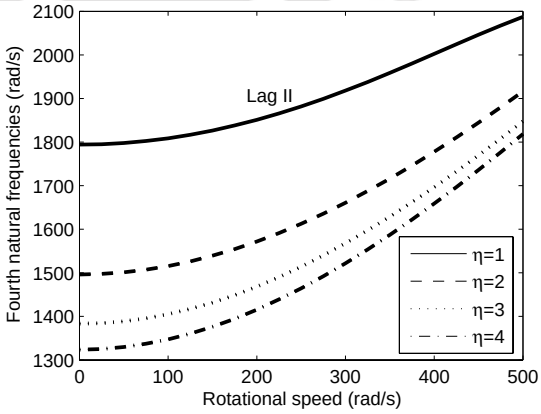

(d) Fourth natural frequencies

Figure 3.13 First four natural frequencies with rotational speeds for various taper paramaters ($\theta = 30^o$, $\beta = 0^o$, $\gamma = 0^o$)

In Figure 3.14, the first two coupled natural frequencies for various ply angles and taper parameters are illustrated. It is observed that a tapered beam yields higher natural frequencies than a uniform cross-section beam. The results show that till a ply angle of about 45^{o} the natural frequencies decrease. Beyond a ply angle $\approx 45^{o}$ the natural frequencies increase monotonically. This is due to the nature of bending stiffness of the tapered beam. The bending stiffness quantities (a_{22} and a_{33}) illustrating the effect of taper parameters for various ply angle orientations is shown in Figure 3.15. However, the overall behavior of tapered and uniform beams is similar. Figure 3.16 shows the effect of taper parameter on forced vibration. It demonstrates that as the taper parameter increases, tip displacement decreases. The maximum tip displacement reduces by 25.87%, 41.49% and 52.19% for the taper parameters of 2, 3 and 4 respectively, compared to taper parameter 1.

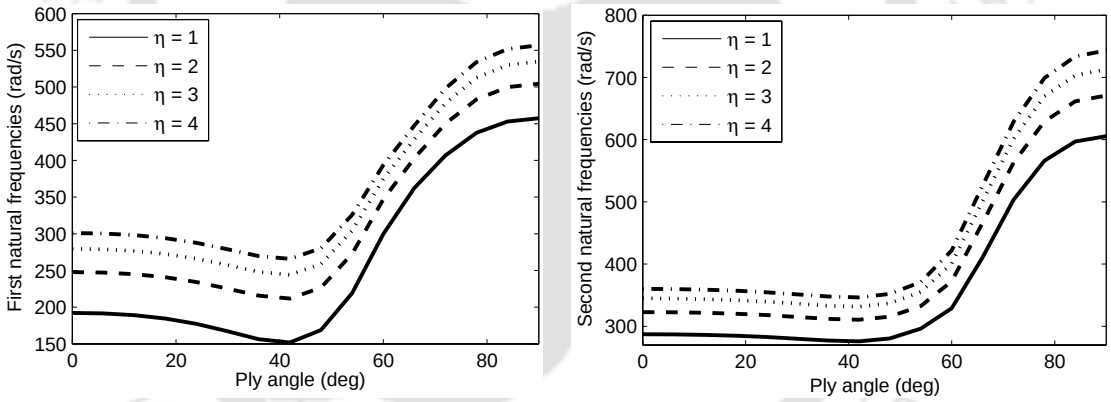

(a) First natural frequencies (b) Second natural frequencies

Figure 3.14 Variation of first two coupled natural frequencies with ply angle for various taper parameters (η) (β =30°, γ = 0°, Ω = 200 rad/s)

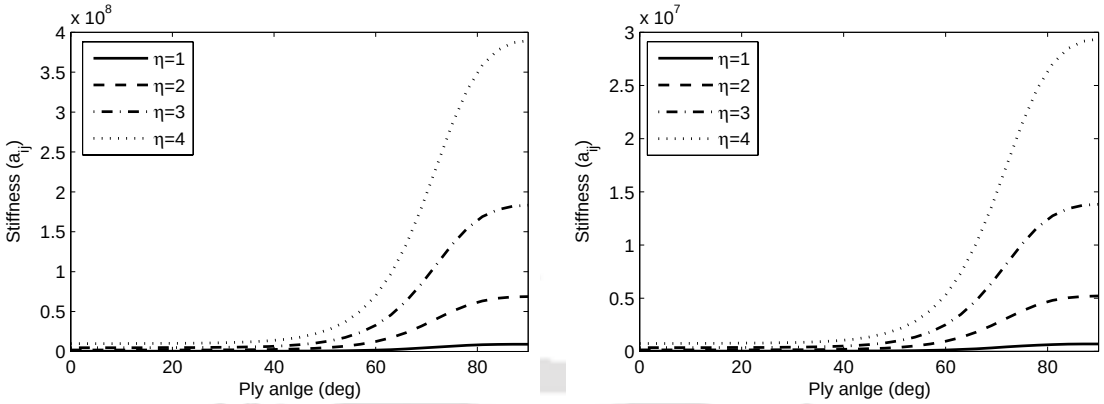

(a) a_{22} (b) a_{33}

Figure 3.15 Variation of bending stiffness quantities with ply angle for various taper parameters (η) (β =30°, γ = 0°, Ω = 200 rad/s)

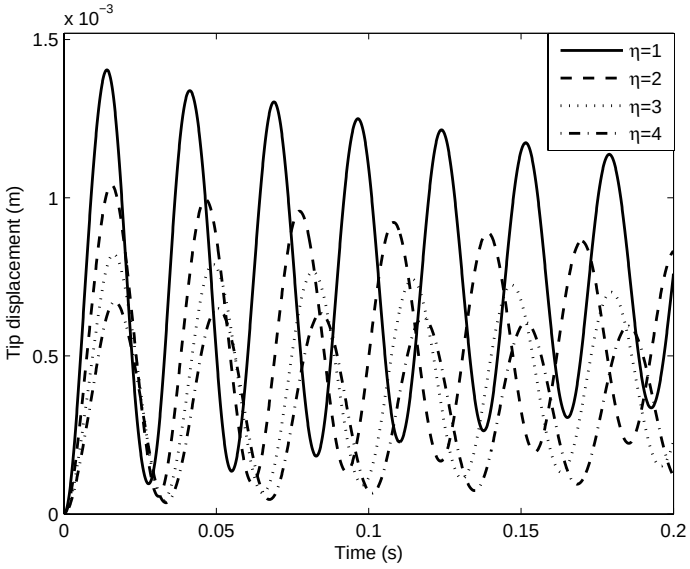

Figure 3.16 Effect of taper on forced vibration (θ = 30°, β = 30°, γ = 0°, Ω = 200 rad/s)

3.6.3 Effect of Pretwist

Figure 3.17 shows the first three normalized eigen modes in lagging mode for pretwist (β) angle varying from 0° to 90° with an increment of 30° pretwist angle. In the first mode increase in pretwist angle bends the beam, whereas in the second and

third modes increase in pretwist angle straightens the beam. Plots also reveal that pretwist angle has marginal influence on the first lagging mode shapes.

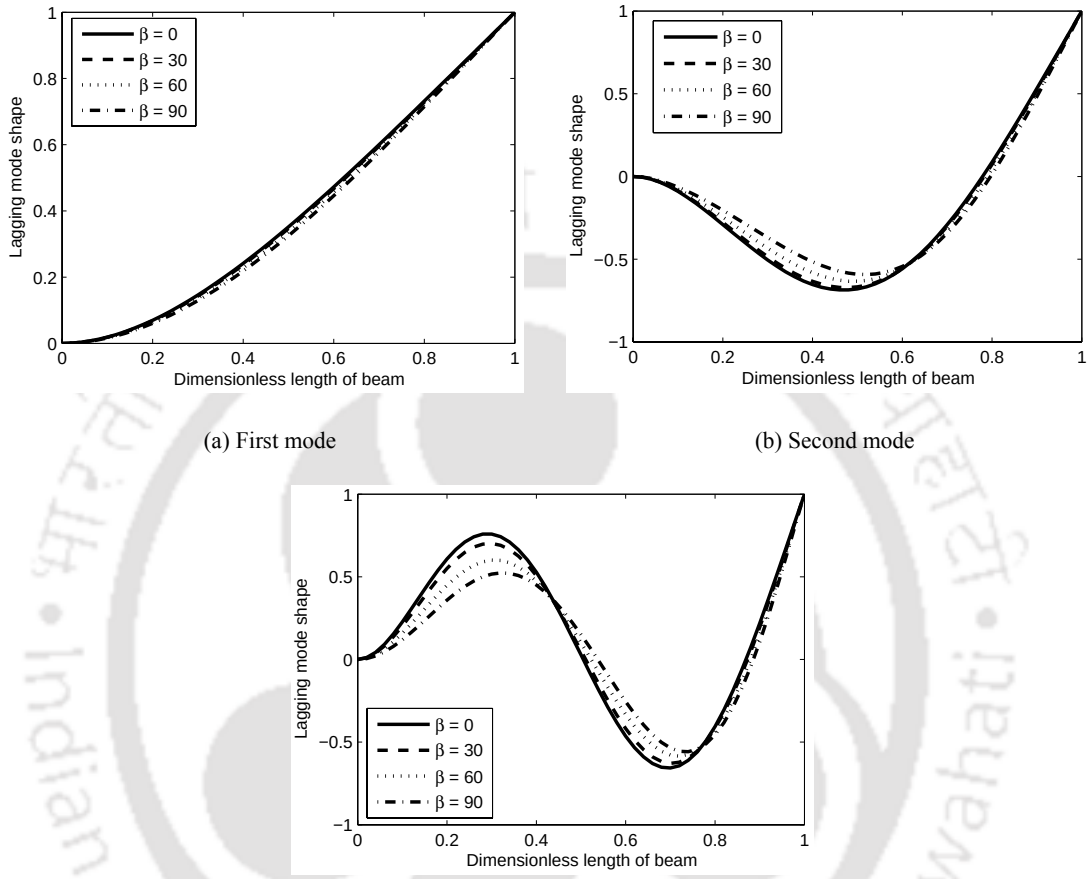

(a) First mode

(b) Second mode

(c)Third mode

Figure 3.17 Normalized lagging mode shape for various pretwist angles

Figure 3.18 shows the first three normalized eigen modes in flapping mode for pretwist (β) angle varying from 0° to 90° with an increment of 30° pretwist angle. In the first and third modes increase of pretwist angle straightens the beam and in the second mode increase of pretwist angle bends the beam. Plots also reveal that pretwist angle has marginal influence on the flapping mode shapes. The effect of pretwist on the first four natural frequencies for various rotational speeds is shown in Figure 3.19. As the rotational speed increases, the natural frequencies also increase. This is due to the centrifugal stiffening effect. Until the rotational speed ≈ 120 rad/s the pretwist in beam

is found to have stiffening effect and beyond ≈ 120 rad/s pretwist in beam has softening effect on the first natural frequencies. But, on the second natural frequencies pretwist has softening effect at lower rotational speeds and stiffening effect at higher rotational speeds. On the third and fourth natural frequencies, the pretwist is having stiffening and softening effect respectively. Plot also reveals that the first lagging mode natural frequency decreases with increase in pretwist angle. But, first flapping mode natural frequency increases with increase in pretwist angle. The effect of pretwist on forced vibration is shown in Figure 3.20. It is found that the tip displacement increases marginally with increase in pretwist angle.

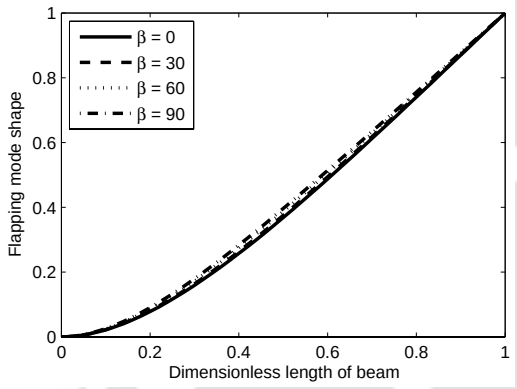

(a) First mode

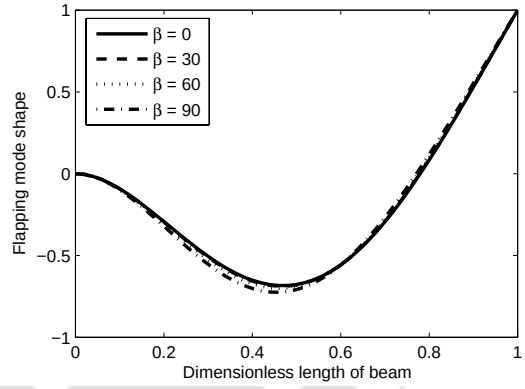

(b) Second mode

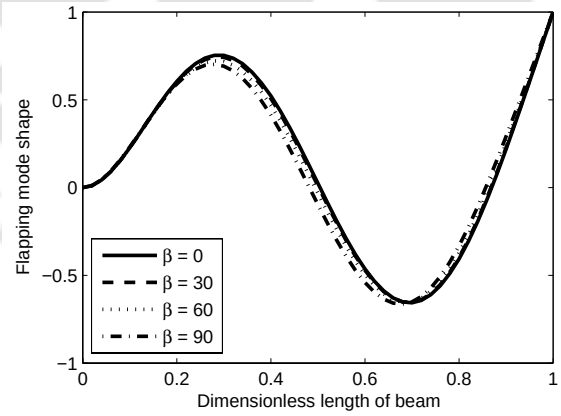

(c) Third mode

Figure 3.18 Normalized flapping mode shape for various pretwist angles

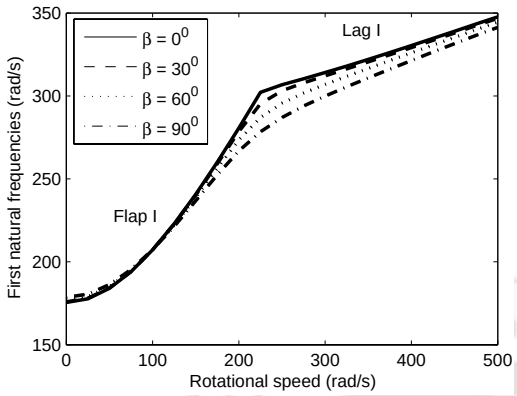

(a) First natural frequencies

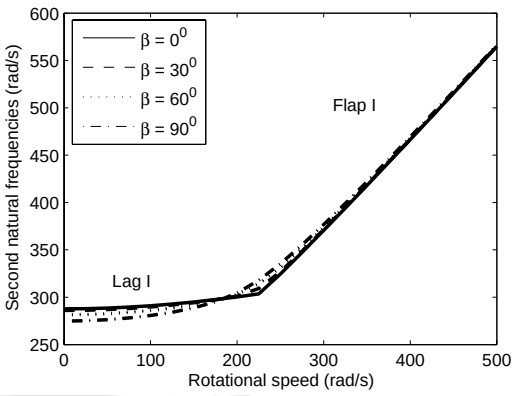

(b) Second natural frequencies

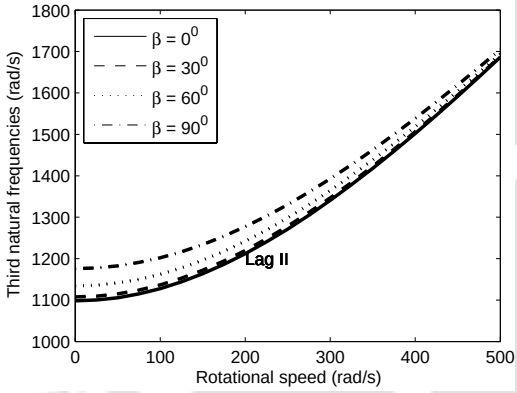

(c) Third natural frequencies

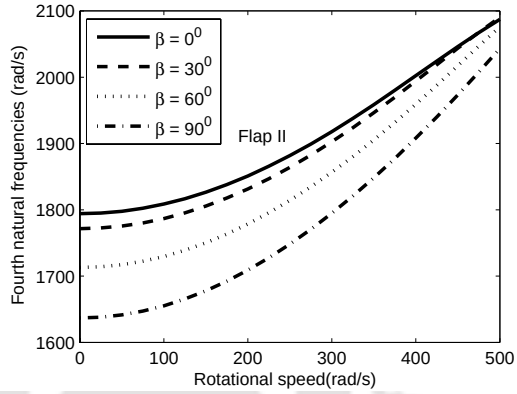

(d) Fourth natural frequencies

Figure 3.19 Variation of first four natural frequencies with rotational speed for various pretwist angles ($\theta = 30^o$, $\gamma = 0^o$, $\eta = 1$, $\Omega = 200$ rad/s)

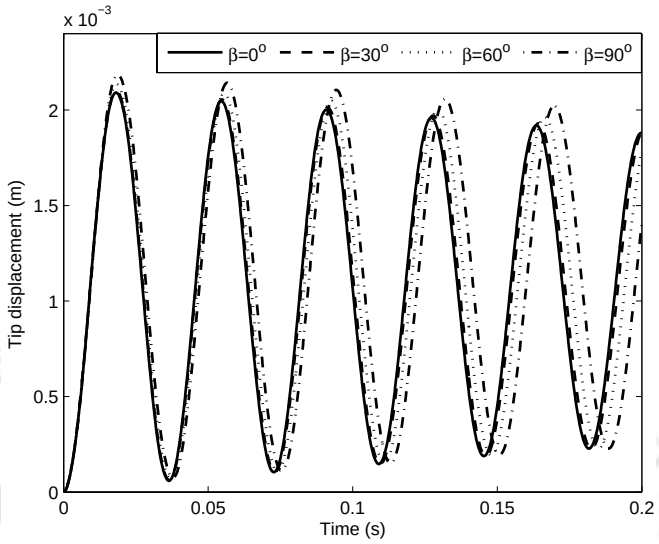

Figure 3.20 Effect of pretwist on forced vibration time response ($\theta = 30^o$, $\gamma = 0^o$, $\eta = 1$, $\Omega = 200$ rad/s)

3.6.4 Effect of presetting

Figures 3.21 (a) - (d) show the first four coupled natural frequencies for various rotational speeds and presetting angles. The first and third natural frequencies correspond to flapping natural frequencies and the second and fourth natural frequencies correspond to lagging natural frequencies. Plots reveal that, the first and third natural frequencies decrease as the presetting angle increases. In other words, preset in beam is having softening effect on the first and third natural frequencies. It is because of the fact that the flapwise bending stiffness a_{22} decreases with increase in presetting angle and lagwise bending stiffness a_{33} increases with presetting angle. Also, preset in the beam is having stiffening effect on the second and fourth natural frequencies. For non-rotating beams, preset is not having any effect on system natural frequencies.

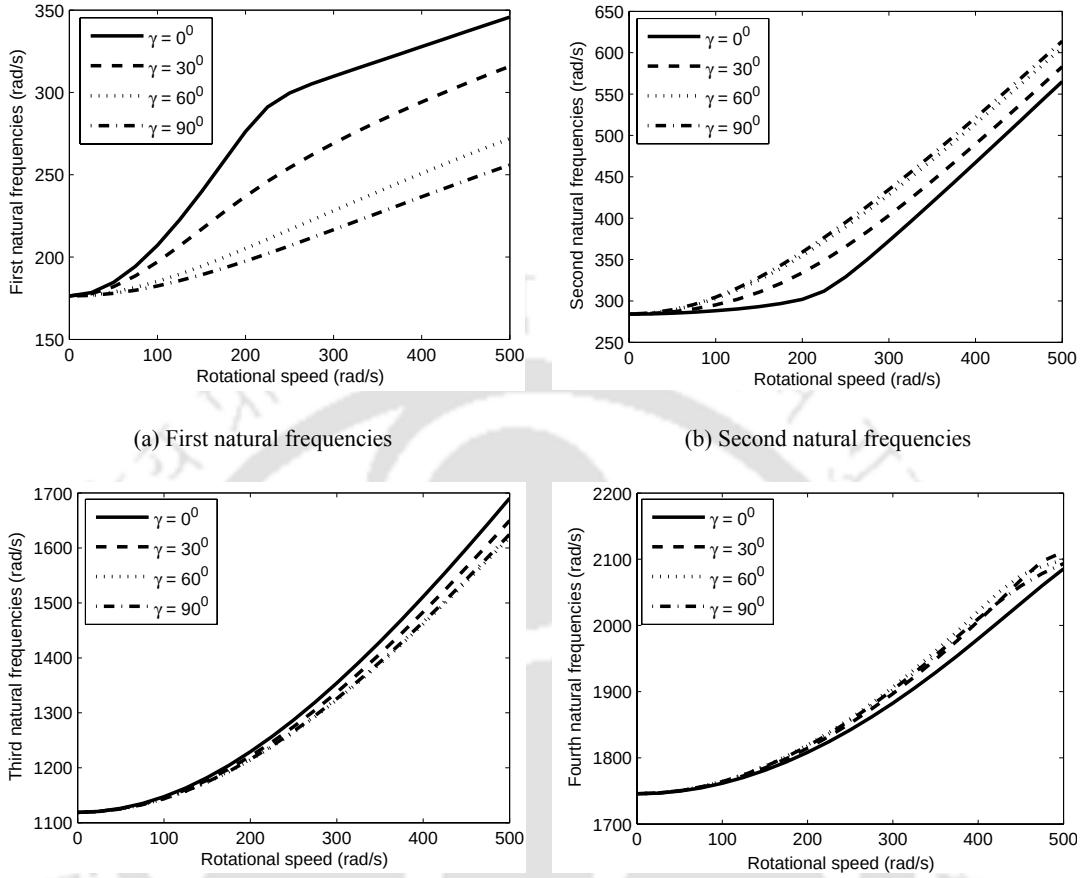

(a) First natural frequencies

(b) Second natural frequencies

(c) Third natural frequencies

(d) Fourth natural frequencies

Figure 3.21 First four natural frequency variations with rotational speeds for various presetting angle ($\theta = 30^o$, $\beta = 30^o$, $\eta = 1$)

In Figure 3.22, the first two coupled natural frequencies for various ply angles and taper parameters are illustrated. It is observed that a preset in beam is having softening effect on the first natural frequencies and stiffening effect on the second natural frequencies. This behaviour is justified by comparing the variation of bending stiffness quantities a_{22} and a_{33} shown in Figure 3.23. The softening effect in the first natural frequencies and stiffening in the second natural frequencies is because of the stiffness quantities a_{22} and a_{33} respectively. The results show that till a ply angle of about 45^o the natural frequencies decrease. Beyond the ply angle $\approx 45^o$ the natural frequencies increase monotonically. The Figure 3.24 shows the effect of preset angle on

forced vibration. It demonstrates that as the preset parameter increases, tip displacement decreases.

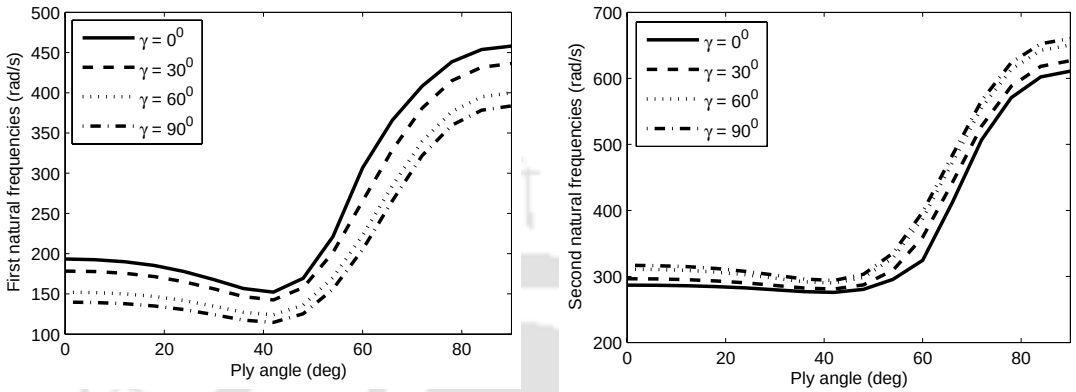

(a) First natural frequencies (b) Second natural frequencies

Figure 3.22 First two natural frequency variations with ply angle for various presetting angles

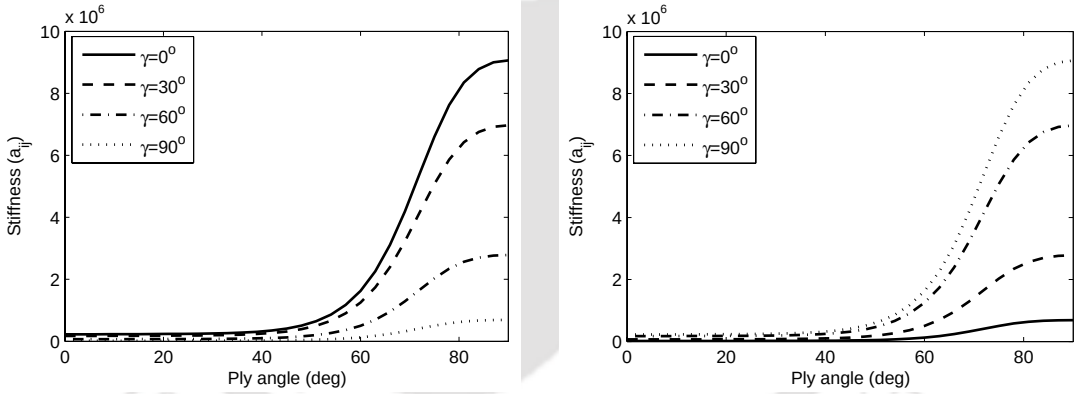

(a) a_{22} (b) a_{33}

Figure 3.23 Variation of bending stiffness quantities with ply angle for various presetting angles

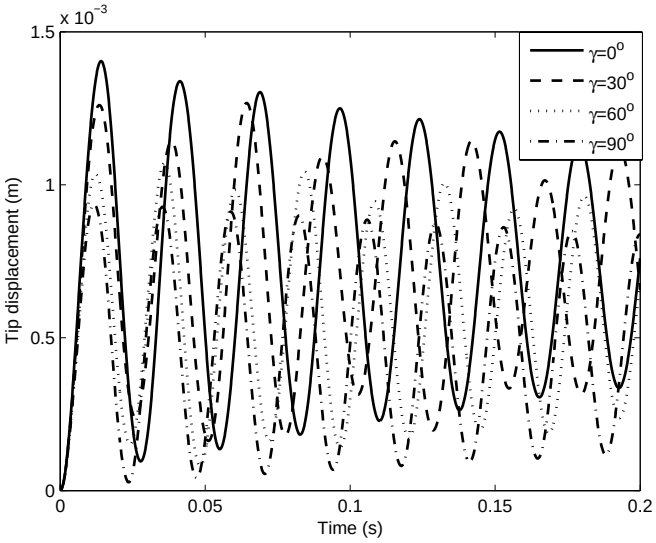

Figure 3.24 Effect of presetting on forced vibration ($\theta = 0^o$, $\beta = 0^o$, $\gamma = 0^o$, $\eta = 1$, $\Omega = 200$ rad/s)

3.7 Conclusions

In this chapter, free and forced vibration studies of rotating beams are presented. Approximate solutions for the equations of motion presented in Chapter 2 are obtained using extended Galerkin's method. Free vibration characteristics are obtained by solving eigen value problem for conservative gyroscopic system. Bending vibration time responses are calculated using Newmark's direct integration method. Results reveal that;

- Gyroscopic coupling between lagging-extension is having considerable effect on the system natural frequency, mode shape and forced response and hence cannot be neglected.
- With the increase in rotational speed the first lagging natural frequency (lagging mode buckles) becomes zero by including gyroscopic coupling. On the contrary by neglecting gyroscopic coupling, the extension mode buckles.

- In the 1st lagging mode, increase in the pretwist, bends the beam indicating softening of beam and in the 2nd & 3rd modes, increase in the pretwist, straightens the beam indicating stiffening of beam.
- In the 1st and 3rd flapping modes, increase in the pretwist stiffens the beam and in the 2nd mode increase in the pretwist softens the beam.
- Pretwist has shallow effect on the first two natural frequencies while it has stiffening and softening effect on the third and fourth natural frequencies respectively.
- Increase in pretwist in forced vibration increases settling time and tip displacement.
- Increase in taper angle softens the 1st flapping and lagging mode and stiffens the 2nd & 3rd flapping and lagging modes.
- Increase in taper increases the first two natural frequencies and decreases the 3rd and 4th natural frequencies.
- In forced vibration, increase in taper reduces the tip displacement.
- In forced vibration, increase in presetting angle reduces the tip displacement.

Chapter 4

Structural modelling of rotating beams with embedded MFC sensors and actuators

4.1 Introduction

In recent years, smart structures such as piezoelectric materials are being extensively used for vibration suppression of flexible structures. Strain in a piezoelectric material produces electrical charge, which is referred as direct piezoelectric effect. Conversely, induced electric field in a piezoelectric material results in a strain, which is known as converse piezoelectric effect. Objective in this chapter is to derive a mathematical model for rotating composite beams with embedded MFC actuators and sensors. In the following sections, the piezoelectric constitutive equations for MFC piezoelectric materials are established. Combined composite host and piezoelectric constitutive equations are derived. Equations of motion for rotating pretwisted composite beam with embedded MFC sensors and actuators using Hamilton's principle are presented.

4.2. Piezoelectric constitutive equation

In vibration suppression applications, direct piezoelectric effect is utilized to estimate the charge/voltage proportional to the strain in the system. The converse piezoelectric effect is used to generate localized strain in the system by applying voltage on the actuator. In the present study, the embedded MFC actuators and sensors are distributed over the top and bottom surface of the beam, respectively as shown in Figure 4.1(a) and Figure 4.1(b). The standard linear piezoelectric constitutive relation representing the direct and converse effect can be written as,

$$D = e\varepsilon + \in E \tag{4.1}$$

$$\sigma = C\varepsilon - e^{\mathrm{T}}E \tag{4.2}$$

where D, e, $\in$, E, ε, σ and C are electric displacement, piezoelectric constant, permittivity coefficient, electric field, strain, stress and elastic constant respectively. Assuming the MFCs to be transversely isotropic and poling in the 1–direction instead of standard 3–directions, converse piezoelectric effect can be written as,

$$\begin{Bmatrix} \sigma_{11}^p \\ \sigma_{22}^p \\ \sigma_{33}^p \\ \tau_{23}^p \\ \tau_{13}^p \\ \tau_{12}^p \end{Bmatrix} = \begin{bmatrix} C_{11} & C_{12} & C_{13} & 0 & 0 & 0 \\ C_{12} & C_{11} & C_{13} & 0 & 0 & 0 \\ C_{13} & C_{13} & C_{33} & 0 & 0 & 0 \\ 0 & 0 & 0 & C_{44} & 0 & 0 \\ 0 & 0 & 0 & 0 & C_{44} & 0 \\ 0 & 0 & 0 & 0 & 0 & \dfrac{C_{11}-C_{12}}{2} \end{bmatrix} \begin{Bmatrix} \varepsilon_{11}^p \\ \varepsilon_{22}^p \\ \varepsilon_{33}^p \\ \gamma_{23}^p \\ \gamma_{13}^p \\ \gamma_{12}^p \end{Bmatrix} - \begin{Bmatrix} e_{11} \\ e_{12} \\ e_{13} \\ 0 \\ 0 \\ 0 \end{Bmatrix} E_1 \tag{4.3}$$

Assuming that the through thickness stress is negligible and piezoelectric fiber is aligned at θ_p from the positive s-axis (Figure 4.1(c)), the transformed reduced constitutive equation for piezoelectric material can be written as

$$\begin{Bmatrix} \sigma_{ss}^p \\ \sigma_{zz}^p \\ \tau_{sz}^p \end{Bmatrix} = \begin{bmatrix} \bar{Q}_{11}^p & \bar{Q}_{12}^p & \bar{Q}_{16}^p \\ \bar{Q}_{12}^p & \bar{Q}_{22}^p & \bar{Q}_{26}^p \\ \bar{Q}_{16}^p & \bar{Q}_{26}^p & \bar{Q}_{66}^p \end{bmatrix} \begin{Bmatrix} \varepsilon_{ss}^p \\ \varepsilon_{zz}^p \\ \gamma_{sz}^p \end{Bmatrix} - \begin{Bmatrix} \bar{e}_{11} \\ \bar{e}_{12} \\ \bar{e}_{13} \end{Bmatrix} E_1; \quad \begin{Bmatrix} \tau_{nz}^p \\ \tau_{sn}^p \end{Bmatrix} = \begin{bmatrix} \bar{Q}_{44}^p & 0 \\ 0 & \bar{Q}_{44}^p \end{bmatrix} \begin{Bmatrix} \gamma_{nz}^p \\ \gamma_{sn}^p \end{Bmatrix} \tag{4.4}$$

where, transformed reduced stiffness,

$$\begin{aligned}
\bar{Q}_{11}^p &= Q_{11}^p \cos^4\theta_P + \left(2Q_{12}^p + 4Q_{66}^p\right)\sin^2\theta_P \cos^2\theta_P + Q_{22}^p \sin^4\theta_P \\
\bar{Q}_{12}^p &= \left(Q_{11}^p + Q_{22}^p - 4Q_{66}^p\right)\sin^2\theta_P \cos^2\theta_P + Q_{22}^p\left(\sin^4\theta_P + \cos^4\theta_P\right) \\
\bar{Q}_{22}^p &= Q_{11}^p \sin^4\theta_P + \left(2Q_{12}^p + 4Q_{66}^p\right)\sin^2\theta_P \cos^2\theta_P + Q_{22}^p \cos^4\theta_P \\
\bar{Q}_{16}^p &= \sin\theta_P \cos\theta_P\left[\left(Q_{11}^p - Q_{12}^p - 2Q_{66}^p\right)\sin^2\theta_P + \left(Q_{12}^p - Q_{22}^p + 2Q_{66}^p\right)\cos^2\theta_P\right] \\
\bar{Q}_{26}^p &= \sin\theta_P \cos\theta_P\left[\left(Q_{11}^p - Q_{12}^p - 2Q_{66}^p\right)\cos^2\theta_P + \left(Q_{12}^p - Q_{22}^p + 2Q_{66}^p\right)\sin^2\theta_P\right]
\end{aligned} \tag{4.5}$$

$$\bar{Q}_{66}^{p} = \sin^2\theta_P \cos^4\theta_P \left(Q_{11}^{p} - 2Q_{12}^{p} + Q_{22}^{p}\right) + \left(\cos^4\theta_P - \sin^4\theta_P\right) Q_{66}^{p}$$

$$\bar{Q}_{44}^{p} = Q_{44}^{p}\left(\sin^2\theta_P + \cos^2\theta_P\right)$$

and $\bar{e}_{11}$ transformed piezoelectric constants are obtained as,

$$\bar{e}_{11} = e_{11}\cos^2\theta_p + e_{12}\sin^2\theta_p$$

$$\bar{e}_{12} = e_{11}\sin^2\theta_p + e_{12}\cos^2\theta_p \qquad (4.6)$$

$$\bar{e}_{13} = \left(e_{11} - e_{12}\right)\cos\theta_p \sin\theta_p$$

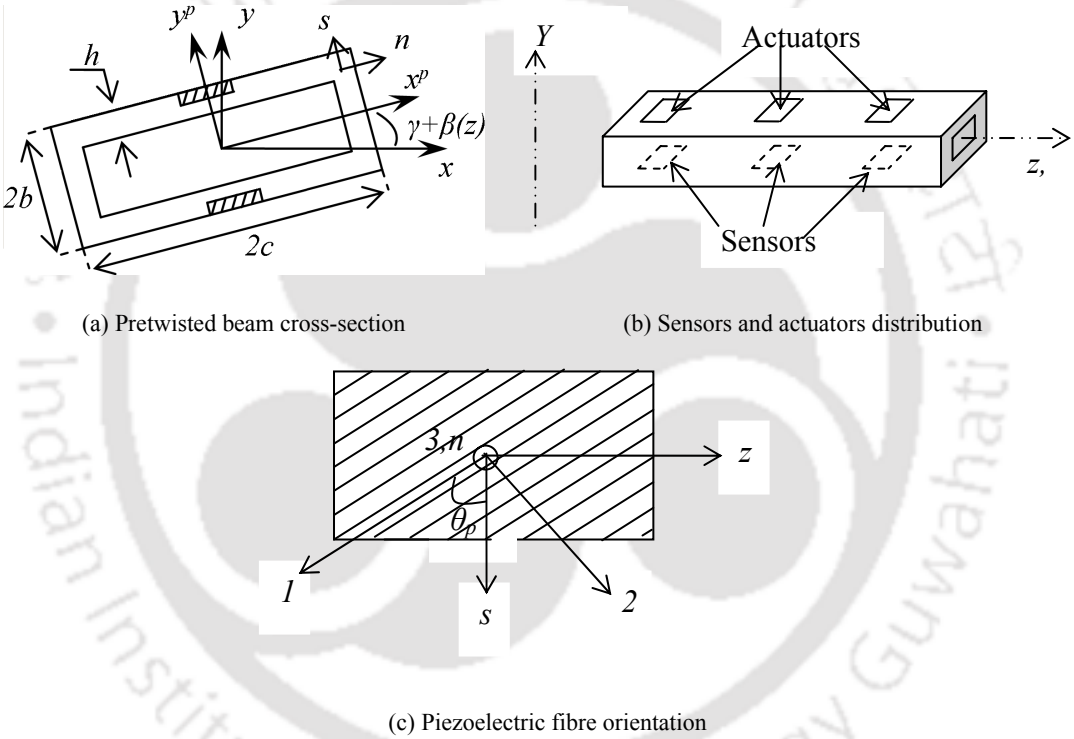

(a) Pretwisted beam cross-section

(b) Sensors and actuators distribution

(c) Piezoelectric fibre orientation

Figure 4.1. Pretwisted beam configuration with embedded piezoelectric patches

Electric displacement for MFCs with poling in 1–direction can be written as,

$$D_1 = \begin{bmatrix} e_{11} & e_{12} & e_{13} & 0 & 0 & 0 \end{bmatrix} \left\{ \varepsilon_{11}^{p} \quad \varepsilon_{22}^{p} \quad \varepsilon_{33}^{p} \quad \gamma_{23}^{p} \quad \gamma_{13}^{p} \quad \gamma_{12}^{p} \right\}^{T} + \in_{11} E_1 \qquad (4.7)$$

Transformed reduced constitutive electric displacement equation can be obtained as,

$$D_z = \bar{e}_{11}\varepsilon_{ss} + \bar{e}_{12}\varepsilon_{zz} + \bar{\in}_{11}\, E_1 \tag{4.8}$$

Piezoelectric constant matrix $\bar{e}$ can be written in the form of piezoelectric strain constant matrix d and elastic constants $\bar{Q}_{ij}^{p}$ as [Lam et al. (1997)]

$$[\bar{e}] = [d][\bar{Q}_{ij}^{p}] \tag{4.9}$$

where $\bar{e}_{ij}$, $\bar{\in}_{ij}$ transformed piezoelectric constant and permittivity coefficients are obtained as.

$$\bar{e}_{11} = d_{11}\bar{Q}_{11}^{p} + d_{12}\bar{Q}_{12}^{p};\ \bar{e}_{12} = d_{11}\bar{Q}_{12}^{p} + d_{12}\bar{Q}_{11}^{p};\ \bar{e}_{16} = (d_{11} + d_{12})\bar{Q}_{16}^{p}; \tag{4.10}$$

$$\bar{\in}_{11} = \in_{11} + \frac{e_{13}^{2}}{\bar{Q}_{33}} \tag{4.11}$$

4.3. Combined composite host and piezoelectric constitutive equation

From Eqs. (4.4) and (2.6) combined electro mechanical constitutive equation for host and piezoelectric material can be written as,

$$\begin{Bmatrix}\sigma_{ss}\\ \sigma_{zz}\\ \tau_{sz}\end{Bmatrix} = \begin{bmatrix}\bar{Q}_{11} & \bar{Q}_{12} & \bar{Q}_{16}\\ \bar{Q}_{12} & \bar{Q}_{22} & \bar{Q}_{26}\\ \bar{Q}_{16} & \bar{Q}_{26} & \bar{Q}_{66}\end{bmatrix}\begin{Bmatrix}\varepsilon_{ss}\\ \varepsilon_{zz}\\ \gamma_{sz}\end{Bmatrix} - \begin{Bmatrix}\bar{e}_{ss}\\ \bar{e}_{zz}\\ \bar{e}_{sz}\end{Bmatrix} E_1;\quad \begin{Bmatrix}\tau_{nz}\\ \tau_{sn}\end{Bmatrix} = \begin{bmatrix}\bar{Q}_{44} & \bar{Q}_{45}\\ \bar{Q}_{45} & \bar{Q}_{55}\end{bmatrix}\begin{Bmatrix}\gamma_{nz}\\ \gamma_{sz}\end{Bmatrix} \tag{4.12}$$

where $\bar{Q}_{ij} = \bar{Q}_{ij}^{h} + \left(\bar{Q}_{ij}^{p} - \bar{Q}_{ij}^{h}\right)H(s,z,n)$ are the transformed reduced stiffness quantities. $H(s,z,n)$ is the Heaviside function and takes value 1 when integrating over piezoelectric material and 0 for host structure.

4.4. Equation of motion

The Hamilton's variational equation is written as,

$$\int_{t_1}^{t_2}\left[\delta T - \delta V + \delta W\right]\mathrm{d}t = 0 \tag{4.13}$$

where, V is the combined potential energy of composite host and piezoelectric material. Potential energy of piezoelectric material includes electrostatic energy. Therefore,

$$V = \tfrac{1}{2}\int_{\tau}\left[\sigma_{ij}\varepsilon_{ij} - ED\right]\mathrm{d}\tau \tag{4.14}$$

$$T = \tfrac{1}{2}\int_{\tau}\rho(\dot{\mathbf{R}}_{\mathrm{i}}.\dot{\mathbf{R}}_{\mathrm{i}})\mathrm{d}\tau \tag{4.15}$$

$$W = \tfrac{1}{2}\int_{\tau}\left[FU - \bar{\sigma}\Phi\right]\mathrm{d}\tau \tag{4.16}$$

where, F, U, $\bar{\sigma}$ and Φ are the external force, displacement vector, applied electric charge and electric potential respectively. Potential energy equation of composite host structure is presented in section 2.3.2. Using Eqs. (2.18) and (4.8) in Eq. (4.14) variational potential energy takes the form,

$$\delta V = \int_{t_o}^{t_1}\int_{\tau}\left[\sigma_{zz}\delta\varepsilon_{zz} + \sigma_{sz}\delta\gamma_{sz} + \sigma_{nz}\delta\gamma_{nz} - \left[\bar{e}_{11}E_1\varepsilon_{ss} + \bar{e}_{12}E_1\varepsilon_{zz} + \bar{\in}_{11}E_1^2\right]\right]\mathrm{d}\tau\,\mathrm{d}t \tag{4.17}$$

From Eqs. (2.10), (2.40), (2.41), (2.43) and (4.17) potential energy equation can be derived as,

$$\delta V = \delta V^H + \int_{t0}^{t1}\int_{0}^{L}\left\{\begin{array}{l}\tilde{a}_1^p E_1\delta\hat{s}' + \tilde{a}_2^p E_1\delta u_0'' + E_1\tilde{a}_3^p\delta u_o' + E_1\tilde{a}_4^p\delta v_0''' + \tilde{a}_5^p\delta v_0' E_1 \\ +\tilde{a}_6^p\delta\theta_x' E_1 + \tilde{a}_7^p\delta\theta_x E_1 + \tilde{a}_8^p\delta\theta_y' E_1 + \tilde{a}_9^p E_1\delta\theta_y + \tilde{a}_{10}^p E_1\delta\phi'\end{array}\right\}\mathrm{d}z\,\mathrm{d}t \tag{4.18}$$

where, δV^H is the potential energy equation for host structure described in 2.3.2 of Chapter 2. To consider the passive effect of mass and stiffness of embedded sensors and actuators, stiffness quantity $\bar{Q}_{ij}$ takes the form described in section 4.3. Upon substituting Eq. (4.18) and kinetic energy equation (Eq. 2.45) in Eq. (4.13) one can write equations of motion as,

$$\begin{aligned}
&\delta u_o:\ \tilde{a}_4(\theta_x'' + v_o''') - \tilde{a}_5\theta_y''' + \tilde{a}_6 u_o^{IV} - (a_{43} + \tilde{a}_2)\theta_x'' + (a_{44} + \tilde{a}_1)(\theta_y' - u_o'') - \tilde{a}_3 v_o''' \\
&+ \tilde{a}_{34}\theta_x''' - \tilde{a}_{32}(\theta_y'' - u_o''') + \tilde{a}_{35}v_o^{IV} + (a_{42} - \tilde{a}_{30})\theta_y'' - (a_{45} + \tilde{a}_{31})(\theta_x' + v_o'') \\
&+ b_1(\ddot{u}_o - 2\Omega\dot{w}_o - \Omega^2 u_o) - I_1\ddot{u}_o'' - \ddot{\theta}_y'(I_3 - I_1) - I_5\ddot{v}_o'' - \ddot{\theta}_x'(I_5 - I_6) + 2\Omega I_6\dot{\phi}' \\
&- \Omega^2[-I_1 u_o'' - \theta_y'(I_3 - I_1) - I_5 v_o'' - \theta_x'(I_5 - I_6) + R_z b_1 u_o''] + (E_1\tilde{a}_2^p)'' - (E_1\tilde{a}_3^p)' = 0
\end{aligned} \tag{4.19}$$

$$\delta v_o:\ \tilde{a}_3(-\theta_y'' + u_o''') + \tilde{a}_9\theta_x''' + \tilde{a}_{10}v_o^{IV} + (a_{52}+\tilde{a}_8)\theta_y'' - \tilde{a}_4u_o''' - (a_{55}+\tilde{a}_7)(\theta_x' + v_o'') - \tilde{a}_{34}\theta_y''' - \tilde{a}_{32}(\theta_x'' + v_o''') + \tilde{a}_{35}u_o^{iv} - (a_{35}+\tilde{a}_{30})\theta_x'' - (a_{45}+\tilde{a}_{31})(-\theta_y' + u_o'') + b_1\ddot{v}_o - I_2\ddot{v}_o'' - \ddot{\theta}_x'(I_2 - I_4) - I_5\ddot{u}_o'' - \ddot{\theta}_y'(I_6 - I_5) + 2\Omega I_4\dot{\phi}' - \Omega^2[-I_2v_o'' - \theta_x'(I_2 - I_4) - I_5u_o'' - \theta_y'(I_6 - I_5) + R_zb_1v_o''] + (E_1\tilde{a}_4^p)'' - (E_1\tilde{a}_5^p)' = 0 \quad (4.20)$$

$$\delta w_o:\ -a_{11}w_o'' - \tilde{a}_{17}\phi'' + b_1\left(\ddot{w}_o + 2\Omega\dot{u}_o - \Omega^2(R_o + z + w_o)\right) - (E_1\tilde{a}_1^p)' = 0 \quad (4.21)$$

$$\delta\theta_x:(a_{55}+\tilde{a}_7)(\theta_x + v_o') - (a_{52}+\tilde{a}_8)\theta_y' + \tilde{a}_4u_o'' - (a_{33}+\tilde{a}_2)\theta_x'' + (a_{43}+\tilde{a}_2)(\theta_y' - u_o'') + \tilde{a}_9v_o''' - \tilde{a}_{32}v_o'' + \tilde{a}_{34}u_o''' - (a_{45}+\tilde{a}_{31})(\theta_y - u_o') + (a_{23}+\tilde{a}_{33})\theta_y'' - (a_{35}+\tilde{a}_{30})(\theta_x' + v_o'') + \ddot{\theta}_x(I_8 - 2I_4 + I_2) + \ddot{\theta}_y(-I_9 + 2I_6 - I_5) + \ddot{v}_o'(I_2 - I_4) + \ddot{u}_o'(I_5 - I_6) + 2\Omega(I_8 - I_4)\dot{\phi} - \Omega^2[\theta_x(I_8 - 2I_4 + I_2) + \theta_y(-I_9 + 2I_6 - I_5) + v_o'(I_2 - I_4) + u_o'(I_5 - I_6)] - (E_1\tilde{a}_6^p)' + E_1\tilde{a}_7^p = 0 \quad (4.22)$$

$$\delta\theta_y:(a_{44}+\tilde{a}_1)(\theta_y - u_o') - (a_{43}+\tilde{a}_2)\theta_x' + \tilde{a}_3v_o'' - (a_{22}+\tilde{a}_{11})\theta_y'' + (a_{52}+\tilde{a}_8)(\theta_x' + v_o'') + (a_{42}-\tilde{a}_{30})\theta_y' - \tilde{a}_{32}u_o'' - (a_{45}+\tilde{a}_{31})(\theta_x + v_o') + (a_{23}+\tilde{a}_{33})\theta_x'' - (a_{24}-\tilde{a}_{30})(\theta_y' - u_o'') + \tilde{a}_{34}v_o''' + \tilde{a}_5u_o''' + \ddot{\theta}_y(I_7 - 2I_3 + I_1) + \ddot{u}_o'(I_3 - I_1) + \ddot{\theta}_x(-I_9 + 2I_6 - I_5) + \ddot{v}_o'(I_6 - I_5) + 2\Omega(I_6 - I_9)\dot{\phi} - \Omega^2[\theta_y(I_7 - 2I_3 + I_1) + u_o'(I_3 - I_1) + \theta_x(-I_9 + 2I_6 - I_5) + v_o'(I_6 - I_5)] - (E_1\tilde{a}_8^p)' + E_1\tilde{a}_9^p = 0 \quad (4.23)$$

$$\delta\phi:\ a_{66}\phi^{IV} - a_{77}\phi'' - \tilde{a}_{17}w_o'' + (I_8 + I_7)\ddot{\phi} - I_{ww}\ddot{\phi}'' - 2\Omega\dot{\theta}_x(I_8 - I_4) + I_4\dot{v}_o' + \dot{\theta}_y(I_6 - I_9) - I_6\ddot{u}_o' - \Omega^2[I_8\phi - I_{ww}\phi'' + R_zb_1(I_8 + I_7)\phi'' - I_9] - (E_1\tilde{a}_{10}^p)' = 0 \quad (4.24)$$

The forced boundary conditions are obtained as,

$$\delta u_o:(a_{43}+\tilde{a}_2)\theta_x' - (a_{42}-\tilde{a}_{30})\theta_y' + (a_{45}+\tilde{a}_{31})(\theta_x + v_o') - (a_{44}+\tilde{a}_1)(\theta_y - u_o') + \tilde{a}_3v_o'' - \tilde{a}_{34}\theta_x'' + \tilde{a}_5\theta_y'' - \tilde{a}_6u_o''' - \tilde{a}_4(\theta_x' + v_o'') + \tilde{a}_{32}(\theta_y' - u_o'') - \tilde{a}_{35}v_o''' + I_1\ddot{u}_o' + \ddot{\theta}_y(I_3 - I_1) + I_5\ddot{v}_o' + \ddot{\theta}_x(I_5 - I_6) + 2\Omega I_6\dot{\phi} - \Omega^2[I_1u_o' + \theta_y(I_3 - I_1) + I_5v_o' + \theta_x(I_5 - I_6) + R_zb_1u_o'] - (E_1\tilde{a}_2^p)' + E_1\tilde{a}_3^p = 0 \quad (4.25)$$

$$\delta u_o':\ \tilde{a}_{34}\theta_x' - \tilde{a}_5\theta_y' + \tilde{a}_6u_o'' + \tilde{a}_4(\theta_x + v_o') + \tilde{a}_{32}(\theta_y - u_o') + \tilde{a}_{35}v_o'' + E_1\tilde{a}_2^p = 0 \quad (4.26)$$

$$\begin{aligned}\delta v_o : &(a_{35}+\tilde{a}_{30})\theta_x^{'}-(a_{52}+\tilde{a}_8)\theta_y^{'}+(a_{55}+\tilde{a}_7)(\theta_x+v_o^{'})+(a_{45}+\tilde{a}_{31})(-\theta_y+u_o^{'})\\&+\tilde{a}_4u_o^{''}-\tilde{a}_9\theta_x^{''}+\tilde{a}_{34}\theta_y^{''}+\tilde{a}_{32}(\theta_x^{'}+v_o^{''})-\tilde{a}_3(-\theta_y^{'}+u_o^{''})-\tilde{a}_{35}u_o^{'''}-\tilde{a}_{10}v_o^{'''}+I_2\ddot{v}_o^{'}\\&+\ddot{\theta}_x(I_2-I_4)+I_5\ddot{u}_o^{'}+\ddot{\theta}_y(I_6-I_5)+2\Omega\dot{\phi}-\Omega^2[I_2v_o^{'}+\theta_x(I_2-I_4)+I_5u_o^{'}\\&+\theta_y(I_6-I_5)-R_zb_1v_o^{'}]-(E_1\tilde{a}_4^p)^{'}+E_1\tilde{a}_5^p=0\end{aligned} \tag{4.27}$$

$$\delta v_o^{'} : \tilde{a}_9\theta_x^{'}-\tilde{a}_{34}\theta_y^{'}-\tilde{a}_{32}(\theta_x+v_o^{'})+\tilde{a}_3(-\theta_y+u_o^{'})+\tilde{a}_{35}u_o^{''}+\tilde{a}_{10}v_o^{''}+E_1\tilde{a}_4^p=0 \tag{4.28}$$

$$\delta w_o : a_{11}w_o^{'}+a_{17}\phi^{'}+E_1\tilde{a}_1^p=0 \tag{4.29}$$

$$\begin{aligned}\delta\theta_x : &(a_{33}+\tilde{a}_{12})\theta_x^{'}-(a_{23}+\tilde{a}_{33})\theta_y^{'}+(a_{35}+\tilde{a}_{30})(\theta_x+v_o^{'})-(a_{43}+\tilde{a}_2)(\theta_y-u_o^{'})\\&+\tilde{a}_{34}u_o^{''}+\tilde{a}_9v_o^{''}+E_1\tilde{a}_6^p=0\end{aligned} \tag{4.30}$$

$$\begin{aligned}\delta\theta_y : &(a_{22}+\tilde{a}_{11})\theta_y^{'}-(a_{23}+\tilde{a}_{33})\theta_x^{'}-(a_{52}+\tilde{a}_8)(\theta_x+v_o^{'})+(a_{24}-\tilde{a}_{30})(\theta_y-u_o^{'})\\&-\tilde{a}_5u_o^{''}-\tilde{a}_{34}v_o^{''}+E_1\tilde{a}_8^p=0\end{aligned} \tag{4.31}$$

$$\delta\phi : a_{77}\phi^{'}+\tilde{a}_{17}w_o^{'}-a_{66}\phi^{'''}+I_{ww}\ddot{\phi}^{'}+\Omega^2(-I_{ww}\phi^{'}+R_zb_1(I_{xx}+I_{yy})\phi^{''})+E_1\tilde{a}_{10}^p=0 \tag{4.32}$$

$$\delta\phi^{'} : a_{66}\phi^{''} \tag{4.33}$$

where, global stiffness quantities $\tilde{a}_{ij}^p$ of piezoelectric material are obtained as,

$$\begin{aligned}&\tilde{a}_1^p=\oint P_1\mathrm{d}s; && \tilde{a}_2^p=\oint -\frac{4P_3}{3h^2}m^p\sin\beta\ \mathrm{d}s;\\&\tilde{a}_3^p=\oint\left[-\frac{4P_3}{h^2}-P_2\right]\cos\beta\ m^p\mathrm{d}s; && \tilde{a}_4^p=\oint -\frac{4P_3}{3h^2}m^p\cos\beta\ \mathrm{d}s;\\&\tilde{a}_5^p=\oint\left[\frac{4P_6}{h^2}-P_4\right]m^p\sin\beta\ \mathrm{d}s; && \tilde{a}_6^p=\oint\left[\frac{4P_3m^p}{h^2}+P_1\bar{y}^p\right]\cos\beta\ \mathrm{d}s;\\&\tilde{a}_7^p=-\oint\left[\frac{4P_6}{h^2}-P_4\right]m^p\sin\beta\ \mathrm{d}s; && \tilde{a}_8^p=\oint\left[\frac{4P_3m^p}{h^2}+P_1\bar{y}^p\right]\sin\beta\ \mathrm{d}s;\\&\tilde{a}_9^p=\oint\left[-\frac{4P_6}{h^2}+P_4\right]m^p\mathrm{d}s; && \tilde{a}_{10}^p=\oint 4P_4\psi\mathrm{d}s;\end{aligned} \tag{4.34}$$

where, local piezoelectric constants are obtained as,

$$\begin{aligned}&P_1=\frac{L_{11}A_{12}}{A_{11}}-L_{12}; && P_2=\frac{L_{11}B_{12}}{A_{11}}-M_{12};\\&P_3=\frac{L_{11}D_{12}}{A_{11}}-O_{12}; && P_4=\frac{L_{11}F_{12}}{A_{11}}-L_{12};\end{aligned} \tag{4.35}$$

$$P_5 = \frac{L_{11}B_{16}}{A_{11}};$$

Stiffness and piezo coefficients are,

$$\begin{aligned}\left(A_{ij},\ B_{ij},\ D_{ij},\ F_{ij},\ H_{ij},\ I_{ij},\ J_{ij}\right) &= \int_{-h/2}^{h/2} \bar{Q}_{ij}\left(1,\ n,\ n^2,\ n^3,\ n^4,\ n^5,\ n^6\right)\mathrm{d}n;\\ \left(L_{ij},\ M_{ij},\ O_{ij},\ R_{ij}\right) &= \int_{h/2-t_P}^{h/2} \bar{e}_{ij}\left(1,\ n,\ n^2,\ n^3\right)\mathrm{d}n;\end{aligned} \tag{4.36}$$

4.5. Sensor equation

Total charge generated on the sensor surface is the spatial summation of all the point charges on the sensor layer [Ray (1998)],

$$q_s(t) = \int_A D_1 H(s,z)\mathrm{d}A \tag{4.37}$$

Therefore, current on the surface of a sensor can be written as,

$$i(t) = \frac{\mathrm{d}q_s(t)}{\mathrm{d}t} = [C_s]\dot{q} \tag{4.38}$$

Components of C_s are

$$\begin{aligned}C_1 &= \int_0^L \oint_s \bar{e}_{11}\frac{h}{6}m^p \sin\beta\ \phi_1^{''}\ \mathrm{d}z\ \mathrm{d}s;\\ C_2 &= \int_0^L \oint_s -\bar{e}_{11}\frac{h}{6}m^p \cos\beta\ \phi_2^{''}\ \mathrm{d}z\ \mathrm{d}s;\\ C_3 &= \int_0^L \oint_s \bar{e}_{11}\frac{h}{6}m^p \phi_3^{'}\ \mathrm{d}z\ \mathrm{d}s;\\ C_4 &= \int_0^L \oint_s \bar{e}_{11}[(\bar{x}^p \sin\beta + \bar{y}^p \cos\beta) + \frac{h}{3}m^p \cos\beta]\phi_4^{'}\ \mathrm{d}z\ \mathrm{d}s;\\ C_5 &= \int_0^L \oint_s \bar{e}_{11}[(\bar{x}^p \cos\beta - \bar{y}^p \sin\beta) - \frac{h}{3}m^p \sin\beta]\phi_4^{'}\ \mathrm{d}z\ \mathrm{d}s;\\ C_6 &= \int_0^L \oint_s -\bar{e}_{11}\frac{h}{2}a\phi_6^{''}\ \mathrm{d}z\ \mathrm{d}s;\end{aligned} \tag{4.39}$$

4.6 Chapter summary

In this Chapter, the governing equations for vibration of rotating composite cantilever beam with embedded MFC sensors and actuators are presented. The effect of higher shear deformation theory is included in the mathematical model. The variational strain energy, kinetic energy and work done by external forces are derived. The equations of motion for rotating beams with boundary conditions are obtained using Hamilton's principle. In Chapter 5, these equations are used to study the controlled time response of rotating beams.

Chapter 5

Vibration control of rotating beams

5.1 Introduction

Objective in this chapter is to design a controller to suppress the vibration of rotating composite cantilever beams. For this purpose, the equations of motion for rotating composite cantilever beam with embedded MFC sensors and actuators developed in Chapter 4 are used. First, approximate solution using extended Galerkin's method is derived and reduced order model constructed therefrom. Equations of motion are represented in state space form for control application. The controller is designed for finding the actuator voltages based on the sensor outputs so that vibration of the rotating beam can be supressed with minimum control effort. Optimal control system directly formulates the performance objectives of the control system and also produces the best possible control system for a given set of performance objectives. In the present study, linear quadratic regulator (LQR) and linear quadratic Gaussian (LQG) controller are designed for rotating cantilever beams.

5.2 Approximate solution using extended Galerkin's method

The approximate solution for the equations of motion with embedded sensors and actuators that have been presented in Chapter 4 is obtained using extended Galerkin's method. The extended Galerkin's method is described in Section 3.2 (Chapter 3). In this method, only geometric boundary conditions appear as boundary terms. Thus considering $u_o = \varphi_1 q_1$, $v_o = \varphi_2 q_2$, $w_o = \varphi_3 q_3$, $\theta_x = \varphi_4 q_4$, $\theta_y = \varphi_5 q_5$ and $\phi = \varphi_6 q_6$; where, $\varphi_i(z)$ and $q_i(t)$ are the vectors of trial function which satisfy geometric boundary conditions and generalized coordinates respectively. Upon

substituting these quantities, the equations of motion can be written in the matrix form as,

$$M\ddot{q} + G_c\dot{q} + Kq = F_{CF} + R(t) + Fu(t) \tag{5.1}$$

where $F_{CF}\left(=\int_0^L 2b_1\Omega^2(R_o+z)dz\right)$, $R(t)$ and F are centrifugal force vector, arbitrary excited load and electric force vector respectively. The electric force vector F is obtained as

$$\begin{aligned} F_1 &= \frac{\tilde{a}_2^p\phi_1^{''}}{h_p} + \frac{\tilde{a}_3^p\phi_1^{'}}{h_p};\ F_2 = \frac{\tilde{a}_4^p\phi_2^{''}}{h_p} + \frac{\tilde{a}_5^p\phi_2^{'}}{h_p};\ F_3 = \frac{\tilde{a}_1^p\phi_3^{'}}{h_p}; \\ F_4 &= \frac{\tilde{a}_6^p\phi_4^{'}}{h_p} - \frac{\tilde{a}_7^p\phi_4}{h_p};\ F_5 = \frac{\tilde{a}_8^p\phi_5^{'}}{h_p} + \frac{\tilde{a}_9^p\phi_5}{h_p};\ F_6 = \frac{\tilde{a}_{10}^p\phi_6^{''}}{h_p} \end{aligned} \tag{5.2}$$

5.3 Reduced order model

In vibration control of flexible structures, effective design of controller generally requires small system size and use of smaller order model for ensuring computational advantage. Therefore, it is necessary to apply a model reduction technique to the state space representation. This gives rise to a need for the model order reduction prior to controller design. The reduced order model contains only those degrees of freedom which are easily excitable ones. The reduced order system model extraction techniques solve the problem of complexity by keeping the essential properties of the full model. In formulating the reduced order model, it is assumed that the lower order modes have lower energy associated and consequently are the most easily excitable ones. First r lower order modes are utilized as a transformation matrix between the generalized coordinates q and the modal coordinates η. Therefore,

$$q(t) = \sum_{i=1}^{r}\psi_i\eta_i \tag{5.3}$$

where ψ is the truncated eigen vector matrix. Eq. (5.1) can be written in reduced order form as,

$$\bar{M}\ddot{\eta}(t) + (\bar{G}_c + C_d)\dot{\eta}(t) + \bar{K}\eta(t) = \psi^{\mathrm{T}}F_{CF} + \psi^{\mathrm{T}}R(t) + \psi^{\mathrm{T}}Fu(t) \tag{5.4}$$

where $\bar{M} = \psi^{\mathrm{T}} M \psi$, $\bar{G}_c = \psi^{\mathrm{T}} \bar{G}_c \psi$ and $\bar{K} = \psi^{\mathrm{T}} K \psi$ are $r \times r$ reduced mass, gyroscopic and stiffness matrices respectively. $C_d = 2\xi_i \omega_i$ is the modal damping matrix and ξ_i is the modal damping ratio.

5.4 Optimal control

Optimal control is the process of determining control and state trajectories for a dynamic system over a period of time to minimise a performance index. Optimal control theory is playing an increasingly important role in the design of modern systems. Given a system and reference signal that one wants the system output to track, the controller will minimize the error between the system output and the reference signal.

5.4.1 Linear quadratic regulator

The linear quadratic regulator (LQR) is a well-known design technique that is known to be less sensitive to system errors. LQR is a linear optimal full state feedback control method with the objective of minimizing the impulse response of the states and the control expenditure, in a quadratic sense. It has a very well designed control procedure and possesses a high level of stability robustness. The feedback controller is designed to minimize a performance index or cost function usually in quadratic form, which is dependent on the choice of the state weighting matrix Q and the input weighting matrix R.

The state space model of the Eq. (5.4) is given by,

$$\dot{X}(t) = AX(t) + Bu(t) + W_f[F_{CF}(t) + R(t)] \tag{5.5}$$

where $X = [q^{\mathrm{T}} \quad \dot{q}^{\mathrm{T}}]$ is the state vector.

Matrices A, B and W_f can be written as,

$$A = \begin{bmatrix} 0 & I \\ -\bar{M}^{-1}\bar{K} & -\bar{M}^{-1}G_c \end{bmatrix};\ B = \begin{bmatrix} 0 \\ -\bar{M}^{-1}F \end{bmatrix};\ W_f = \begin{bmatrix} 0 \\ \bar{M}^{-1} \end{bmatrix} \tag{5.6}$$

The optimal control $u(t)$ is obtained by minimizing the quadratic cost function,

$$J = \frac{1}{2}\int_0^\infty x(t)^T Q x(t) + u(t)^T R u(t) \mathrm{d}t \tag{5.7}$$

where, Q, R, $x(t)$ and $u(t)$ are positive semi-definite state weighting matrix, positive definite input weighting matrix, state vector and control input vector respectively. The components of Q and R matrices have to be chosen correctly to obtain good control gain. If the components of Q are chosen large relative to those of R, then deviations of x from zero will be penalized heavily relative to deviations of u from zero. If the components of R are large relative to those of Q, then control effort increases and settling time may also increase. The weighting matrices Q and R are selected such that they are related to potential energy, kinetic energy and electric force as,

$$Q = \begin{bmatrix} \beta \psi^{\mathrm{T}} K \psi & 0 \\ 0 & \alpha \psi^{\mathrm{T}} M \psi \end{bmatrix} \tag{5.8}$$

$$R = \eta F^T \psi^{\mathrm{T}} K \psi F \tag{5.9}$$

The control law that minimizes performance index J can be written as,

$$u(t) = -KX \tag{5.10}$$

where $K = R^{-1} B^{\mathrm{T}} P$ is the LQR gain and P is obtained by solving algebraic Riccati equation

$$PA + A^{\mathrm{T}} P + Q - PBR^{-1} B^{\mathrm{T}} P = 0 \tag{5.11}$$

5.4.2 Linear quadratic Gaussian

In vibration suppression applications, structural states are normally chosen as modal displacements and velocities. These states cannot be measured directly. Hence, full state feedback cannot be constructed. Using a Kalman filter for estimation and feeding the estimated states back is known as LQG control.

Covariance of disturbance and measured noise are the design parameters of the Kalman filter. In practice, these covariance values are not necessarily set to their actual values, but are used as adjustments to tune the filter. In LQG controller, full state feedback LQR gain and the Kalman filter state estimation are done separately. Kalman filter is designed with the assumption of Gaussian distribution of white noise. State space form of Eq. (5.4) with stochastic disturbances can be written as,

$$\dot{X}(t) = AX(t) + Bu(t) + W_f[F_{CF}(t) + R(t)] + w(t) \tag{5.12}$$

where $X = [\eta^{\mathrm{T}} \quad \dot{\eta}^{\mathrm{T}}]$ is the state vector.

$$y(t) = CX(t) + v(t) \tag{5.13}$$

where $w(t)$ and $v(t)$ are stochastic Gaussian white noises. The covariance of these white noises can be expressed as,

$$E\left\{w(t)w(t)^{\mathrm{T}}\right\} = W \tag{5.14}$$

$$E\left\{v(t)v(t)^{\mathrm{T}}\right\} = V \tag{5.15}$$

$$E\left\{w(t)v(t)^{\mathrm{T}}\right\} = 0 \tag{5.16}$$

The condition in Eq. (5.16) indicates that the system noise and sensor noise are independent. Matrices A, B, W_f and C can be written as,

$$A = \begin{bmatrix} 0 & I \\ -\bar{M}^{-1}\bar{K} & -\bar{M}^{-1}(C_d + \bar{G}_c) \end{bmatrix};\ B = \begin{bmatrix} 0 \\ -\psi^{\mathrm{T}}\bar{M}^{-1}F \end{bmatrix}; \tag{5.17}$$

$$W_f = \begin{bmatrix} 0 \\ \psi^{\mathrm{T}}\bar{M}^{-1} \end{bmatrix}; C = [0 \quad C_s\psi]$$

The LQG optimal control algorithm consists of minimizing the functional defined in Eq. (5.7) subject to constraints in Eqs. (5.12) and (5.13). The optimal control $u(t)$ is obtained from estimated state and measured output. Therefore, the actuator input voltage for the plant (Eq. 5.12) can be written as [Frank and Vassilis (1995)]

$$u(t) = -KX_e \tag{5.18}$$

where $K = R^{-1}B^{T}P$ is the LQR gain and P is obtained by solving algebraic Riccati equation

$$PA + A^{T}P + Q - PBR^{-1}B^{T}P = 0 \tag{5.19}$$

X_e is the estimated state that is obtained by solving the differential equation,

$$\dot{X}_e = (A - BK - LC)X_e + Ly \tag{5.20}$$

where $L = SC^{T}V^{-1}$ is the Kalman gain and S is obtained by solving filter Riccati equation

$$AS + SA + W - SC^{T}V^{-1}CS = 0 \tag{5.21}$$

5.5 Numerical analysis

The beam considered for analysis is composed of graphite-epoxy composite material with properties listed in Table 5.1. Properties of piezoelectric materials are also tabulated in Table 5.1.

Table 5.1 Composite and piezoelectric material properties

Material properties	Passive composite host	MFC	PZT
E_1 (Gpa)	206.8	30.4	124
E_2 (Gpa)	5.17	15.86	130
$G_{12} = G_{13}$ (GPa)	3.1	5.52	70
G_{23} (GPa)	2.5511	5.52	74
γ_{12}	0.25	0.31	0.25
ρ(kg/m^3)	1528.15	8528	8000
d_{11} (pC/N)	—	460	310 (d_{33})
d_{12} (pC/N)	—	-210	-140 (d_{31})
Thickness (mm)	10.16	0.3	0.3

Number of reduced order modes in a reduced order model should be large enough, such that the effect of residual modes can be neglected. Here number of reduced order modes is selected by analyzing convergence of tip displacement and

actuator voltage. To obtain required number of reduced order modes, different beam configurations are analyzed. Untwisted and pretwisted configuration results are displayed in Figures 5.1 and 5.2 respectively. The effect of number of modes considered in the reduced order model on tip displacement and applied control voltage are shown in Figures 5.1(a) and 5.1(b) respectively. Considered beam is composed of 6 layers of anti-symmetric configuration with the ply angle of 30 degrees. The control gain is obtained using LQR control algorithm. For the mentioned configuration, it is found that first five low frequency modes are sufficient for the convergence of tip displacement and actuator voltage. In Tables 2.1 and 2.2 coupling between different motions are listed. Also, it is discussed in Section 2.4 that some coupling vanishes for untwisted and symmetric ply angle orientation. To analyze the effect of reduced order modes on pretwist, pretwisted beam configuration is studied and the results are presented in Figures 5.2(a) and (b). The beam considered in the present analysis is composed of 6 layers of anti-symmetric configuration with the ply angle of 30^o and pretwist angle of 30^o. It is found that first eleven low frequency modes are sufficient for the convergence of tip displacement (Figure 5.2(a)) and actuator voltage (Figure 5.2(b)). Hence, further analysis is carried out by considering eleven low frequency modes in the reduced order model.

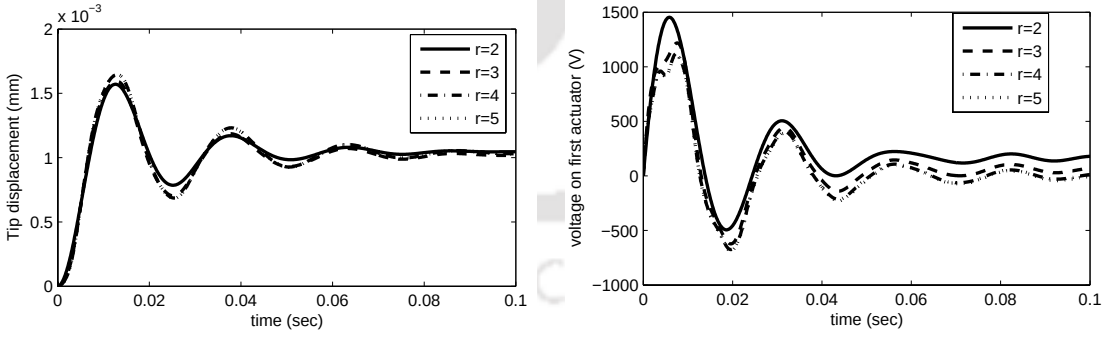

(a) Tip displacement

(b) Actuator voltage

Figure 5.1 Convergence of number of modes in reduced order model for a untwisted beam configuration for a step loading ($\theta = 0^o$, $\beta = 0^o$, $\gamma = 0^o$, $\eta = 1$, $\Omega = 200$ rad/s)

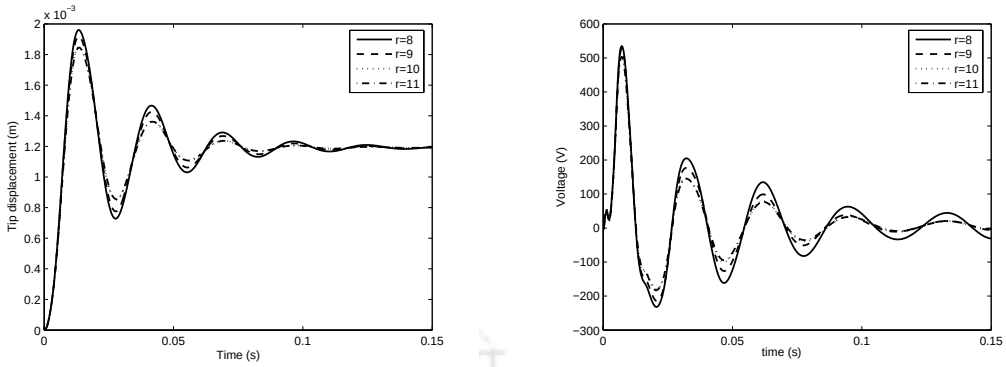

(a) Tip displacement (b) Actuator voltage

Figure 5.2 Convergence of number of modes in reduced order model for a pretwisted beam configuration for a step loading ($\theta = 0^o$, $\beta = 30^o$, $\gamma = 30^o$, $\eta = 1$, $\Omega = 200$ rad/s)

5.5.1 Passive effect of sensors and actuators

The variation of first four natural frequencies for different values of ply angle orientation and non-rotating beam configuration are shown in Figures 5.3(a)-(d). Solid line shows the results by neglecting the effect of mass and stiffness of sensors and actuators. Dashed line shows the results by considering the passive effect (effect of mass and stiffness) of MFCs. Dotted line shows the results with PZT sensors and actuators. For the analysis, 6 sensors and actuators of cross-section (0.057 m X 0.08 m) spaced equally and embedded in the host structure are considered. The plots reveal that inclusion of MFCs reduces the natural frequencies of the system up to approximately 75^o ply angle. Beyond 75^o, the natural frequencies increase in the case of MFC actuators and sensors. Decrease in natural frequency beyond 75^o is due to decrease in stiffness quantity $\tilde{a}_2$ (Figure 5.5). Figures 5.4 (a)-(d) show the counterpart for a rotating beam with rotational speed of 200 rad/s. Trends observed in rotating and non-rotating beams are similar. In Figure 5.6, the variation of first four natural frequencies for various rotational speeds is shown. The inclusion of piezoelectric material in a rotating beam softens the beam. Comparing the results of natural frequency, by neglecting and considering the effect of masses of sensors/actuators, it can be observed that at lower rotational speeds, the difference in natural frequencies increases with rotational speed; whereas, in 2^{nd}, 3^{rd} and 4^{th}

natural frequencies, difference in the frequencies reduces with increase in rotational speed. It is difficult to physically explain this phenomenon. It requires further investigation to confirm the effect and find possible explanation. This may be because increase in rotational speed changes the centrifugal force and gyroscopic force. This requires further investigation.

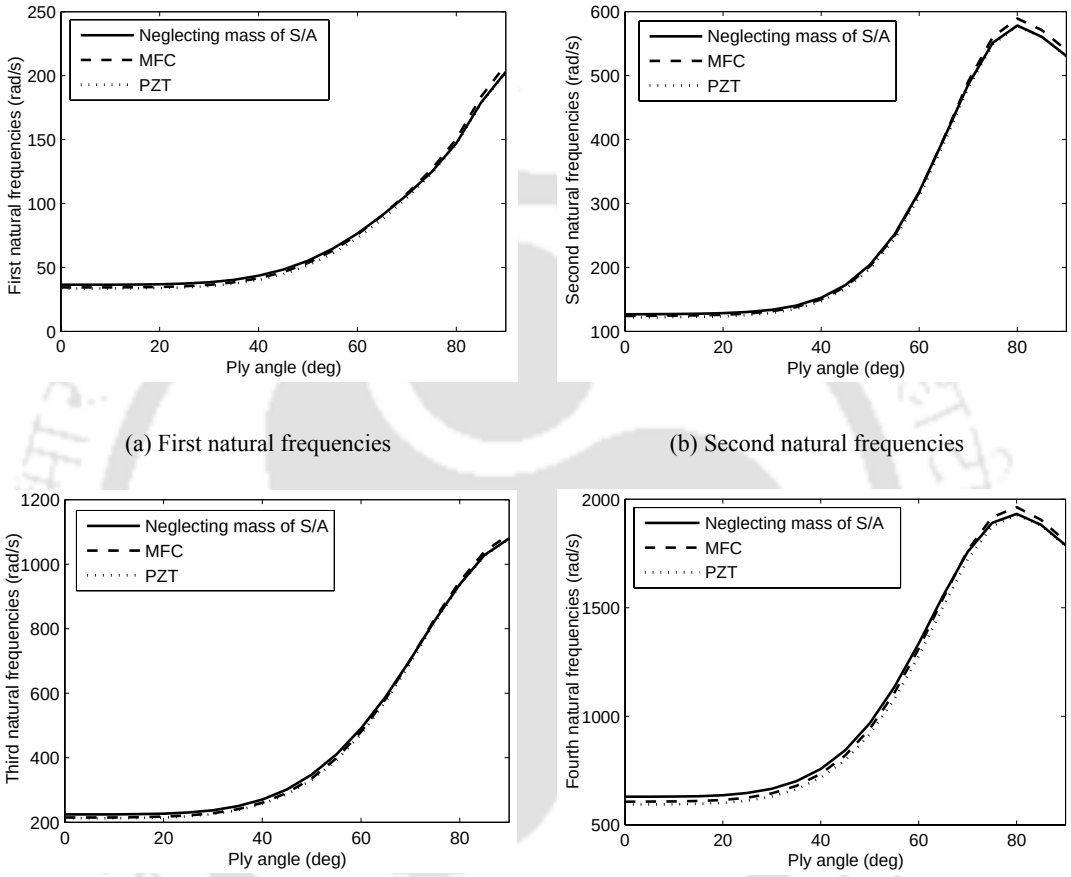

(a) First natural frequencies

(b) Second natural frequencies

(c) Third natural frequencies

(d) Fourth natural frequencies

Figure 5.3 Passive effect of piezoelectric masses on natural frequencies of non-rotating beam ($\beta = 0^o$, $\gamma = 0^o$, $\eta = 1$, $\Omega = 0$ rad/s)

5.5.2 Control of rotating beams

In the present study, the rotating beam is controlled using LQG algorithm using two methods. First, the output voltage from individual sensors are summed and amplified to obtain control gain. Identical amplified control voltage is applied to each actuator. In other words, same amplified voltage is applied to all the distributed actuators. Secondly, the output voltage from individual sensors are measured and

amplified to obtain control gain for each of the actuators separately and applied to the actuators. In Eq. 5.1, *F* (obtained from Eq. 5.2) is electric force vector and *u(t)* is the control voltage vector. If it is desired to individually control the actuators, *F* takes the dimension equal to (reduced order model X number of actuators) and *u(t)* is a vector of dimension equal to number of actuators. Control voltages applied to individual actuators *u(t)* are obtained by the product of control gain and the state vector (Eq. 5.10). The LQG control algorithm used to obtain the control gain is discussed in Section 5.4.2 on Page No. 75.

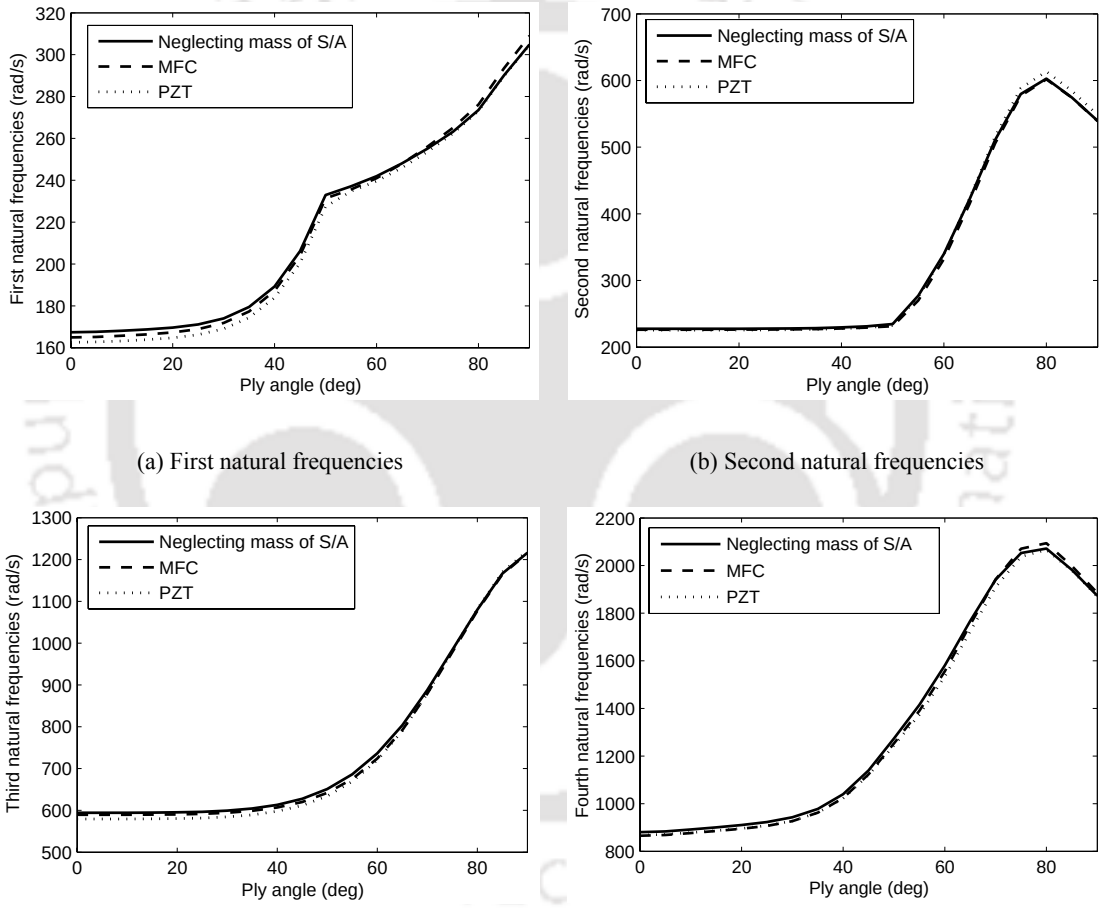

(a) First natural frequencies

(b) Second natural frequencies

(c) Third natural frequencies

(d) Fourth natural frequencies

Figure 5.4 Passive effect of piezoelectric masses on natural frequencies for various ply angles ($\beta = 0^o$, $\gamma = 0^o$, $\eta = 1$, $\Omega = 200$ rad/s)

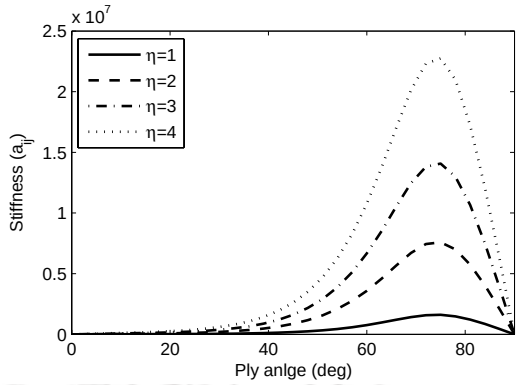

Figure 5.5 Variation of stiffness quantity $\widetilde{a}_2$ with ply angle for various taper parameters

5.5.2.1 Applying identical amplified voltage on all actuators

The bending vibration tip displacement controlled response with PZT and MFC actuators/sensors is shown in Figure 5.7 (a) for a ply angle of 30°. Four sensors and actuators of cross-section (0.057 m X 0.08 m) spaced equally and embedded in the host structure are considered for the numerical analysis. The applied amplified control voltage is shown in Figure 5.7 (b). The counterpart of results for ply angle orientation of 60° is shown in Figure 5.8. The settling time, peak displacement and actuating voltage by using MFC is comparatively less than that of PZT. Performance of MFC actuators for vibration suppression is evident from the plots. For the present configuration, voltages applied on the actuator are well below the upper limit of the MFC actuator voltage of 1500V.

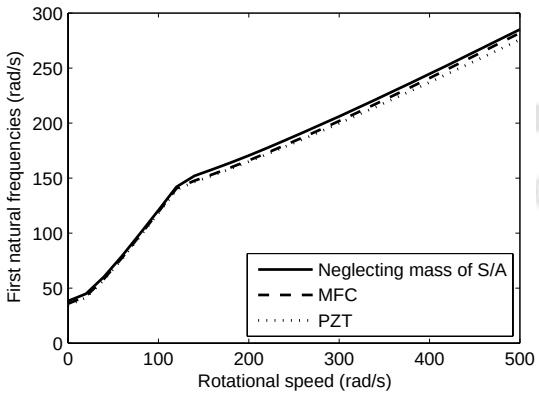

(a) First natural frequencies

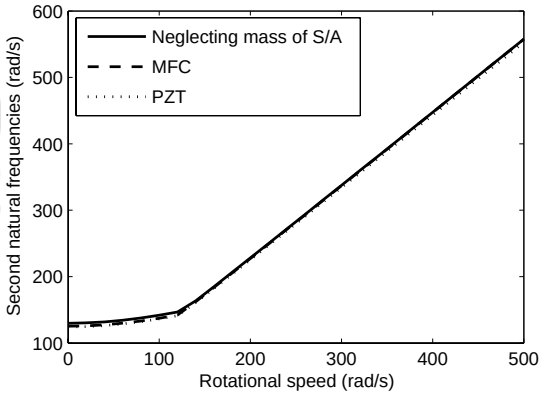

(b) Second natural frequencies

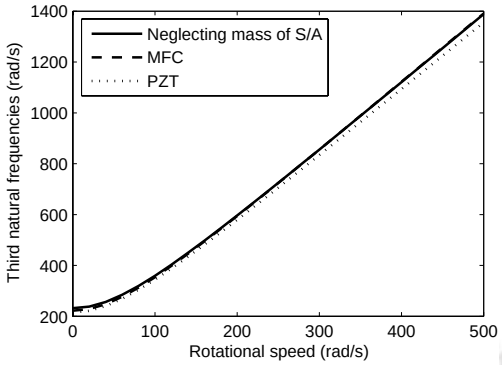

(c) Third natural frequencies

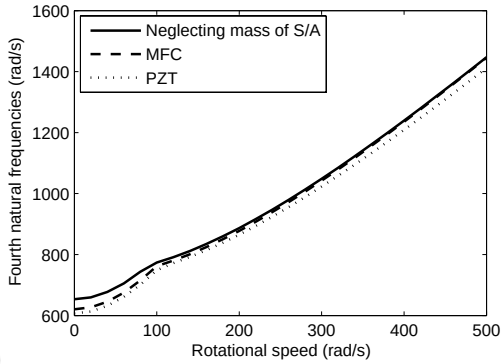

(d) Fourth natural frequencies

Figure 5.6 Passive effect of piezoelectric masses on natural frequencies for various rotational speeds ($\theta = 0^o$, $\beta = 0^o$, $\gamma = 0^o$, $\eta = 1$)

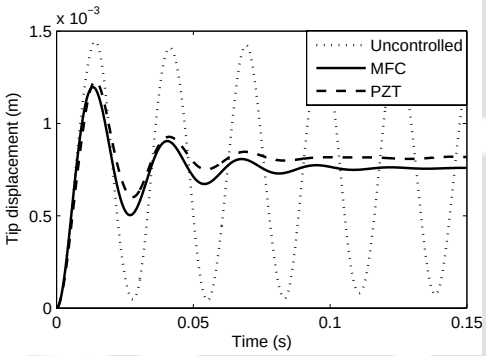

(a) Tip displacement

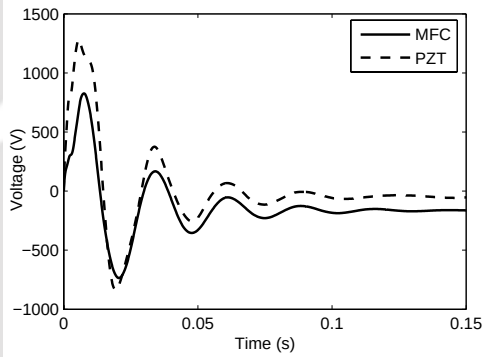

(b) Actuator voltage

Figure 5.7 Comparison of controlled response using MFC and PZT sensors and actuators for a step loading ($\theta = 30^o$, $\Omega = 200$ rad/s, $\beta = 30^o$, $\gamma = 30^o$, $\eta = 1$)

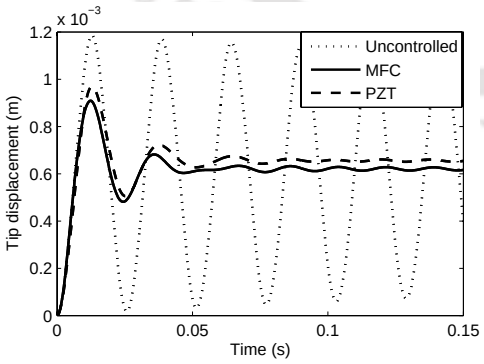

(a) Tip displacement

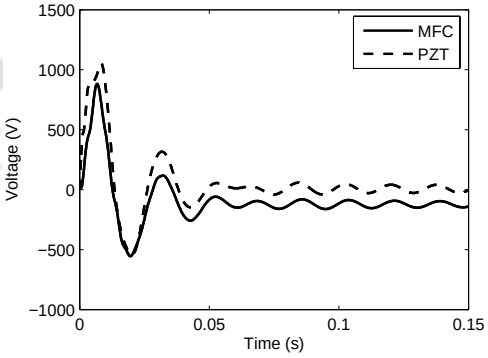

(b) Actuator voltage

Figure 5.8 Comparison of controlled response using MFC and PZT sensors and actuators for a step loading ($\theta = 60^o$, $\Omega = 200$ rad/s, $\beta = 30^o$, $\gamma = 30^o$, $\eta = 1$)

The effect of MFC actuator length on the tip displacement (Figure 5.9(a)) and actuator voltage (Figure 5.9(b)) are shown. In all these plots 10%, 25%, 50% and 100% area of sensors/actuators are considered. It is observed that the tip displacement and actuator voltage for the first three cases (10%, 25% and 50%) reduces, as the area of the sensor/actuator increases. In other words, control effort is less. Whereas, in the fourth case when the MFC sensors and actuators covers the entire surface of the beam, the tip displacement and settling time increases. When the sensors and actuators are at the tip of the rotating beam, they have negative effect. This is due to the fact that the sensors and actuators in the tip of the rotating beam act as added mass. Similar trend is observed by Choi et al. [2006, 2007]. Hence, in the analysis, co-located actuators and sensors are considered as equally distributed between 0 – 70% span of the beam.

The bending vibration controlled response for a step forcing with rotational speed of 100 rad/s is shown in Figure 5.10. Four sensors and actuators of cross-section (0.057 m X 0.08 m) spaced equally and embedded in the host structure are considered for the analysis. The counter part of Figure 5.10 with rotational speed of 200 rad/s is shown in Figure 5.11. It is noticed that maximum tip displacement and control voltage applied to the actuators for 60^{o} ply angle is less as compared to 30^{o} ply angle.

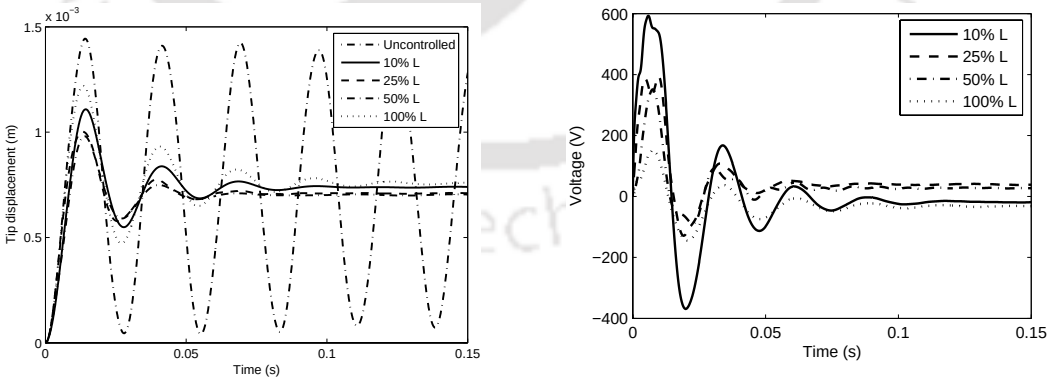

(a) Tip displacement (b) Actuator voltage

Figure 5.9 Controlled time responses for varying lengths of MFC sensors and actuators for a step loading ($\theta = 30^{o}$, $\beta = 0^{o}$, $\gamma = 0^{o}$, $\eta = 1$, Ω=200 rad/s)

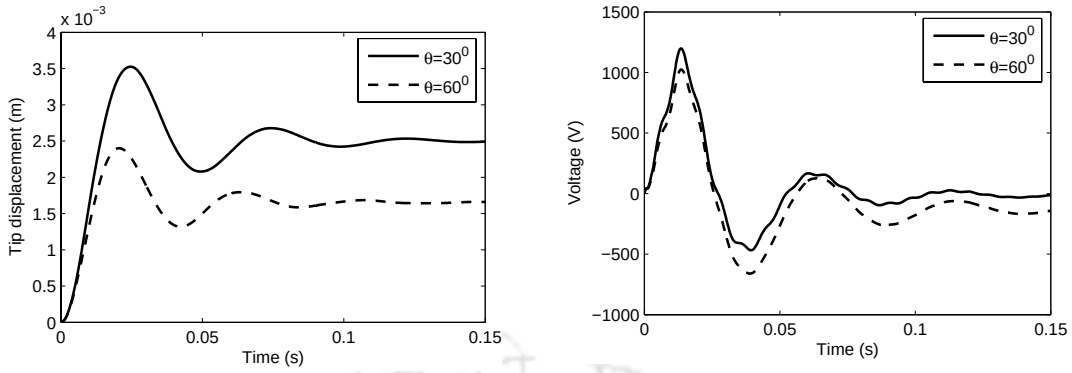

(a) Tip displacement (b) Actuator voltage

Figure 5.10 Controlled time responses for two ply angle orientations at 100 rad/s rotational speed for a step loading ($\beta = 0^o$, $\gamma = 0^o$, $\eta = 1$)

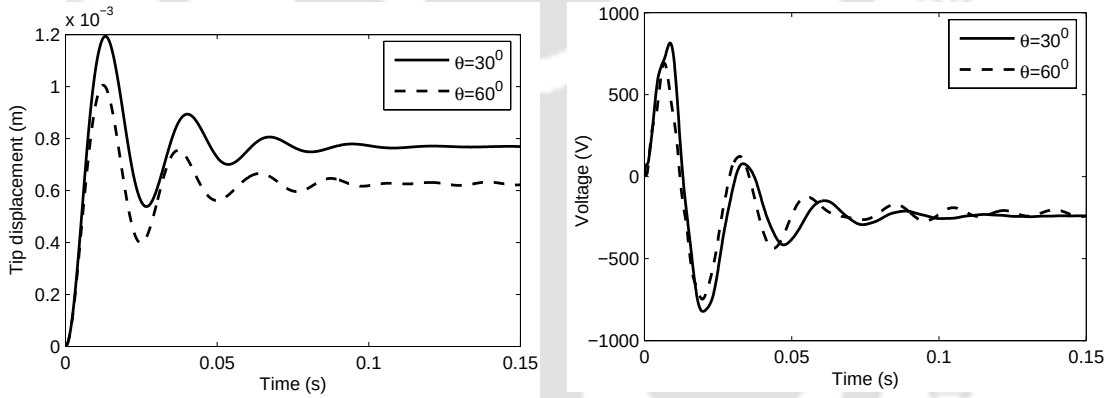

(a) Tip displacement (b) Actuator voltage

Figure 5.11 Controlled time responses for two ply angle orientations at 200 rad/s rotational speed for a step loading ($\beta = 0^o$, $\gamma = 0^o$, $\eta = 1$)

The effect of taper parameter on tip displacement and control voltage for a step forcing and rotational speed of 200 rad/s is presented in Figures 5.12(a) and 5.11(b) respectively. Four sensors and actuators of cross-section (0.057 m X 0.08 m) spaced equally and embedded in the host structure are considered for the analysis. It is observed that increase in taper, decreases the maximum tip displacement and actuator voltage. But, increase in taper, increases the settling time.

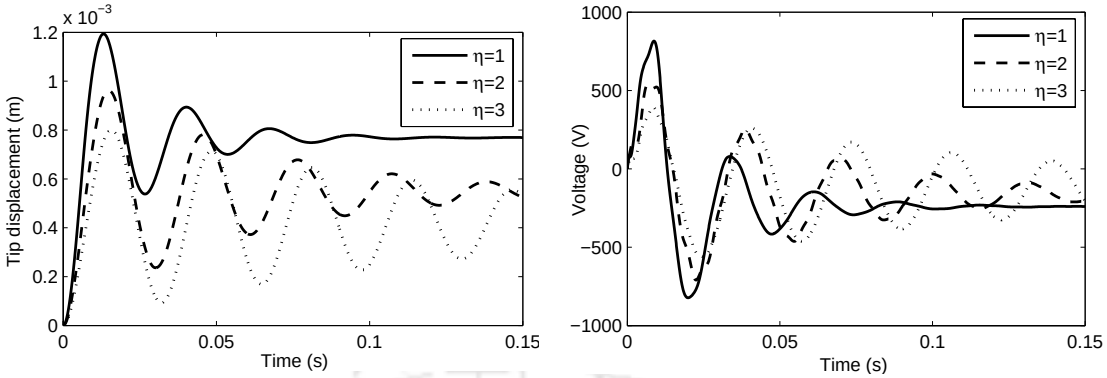

(a) Tip displacement (b) Actuator voltage

Figure 5.12 Controlled time responses for various taper parameters at 200 rad/s rotational speed for a step loading ($\theta = 30^o$, $\beta = 0^o$, $\gamma = 0^o$)

Transient bending vibration control for three pretwist angles of 0^o, 30^o and 60^o is shown in Figure 5.13 (a) and control voltages applied to the actuator is shown in Figure 5.13(b). It can be noticed that 0^o pretwisted beam settles a bit faster compared to 30^o and 60^o pretwisted beam. Applied peak voltages on the actuators for 0^o pretwisted beam is slightly higher, but settles a bit faster as compared to 30^o and 60^o pretwisted beam.

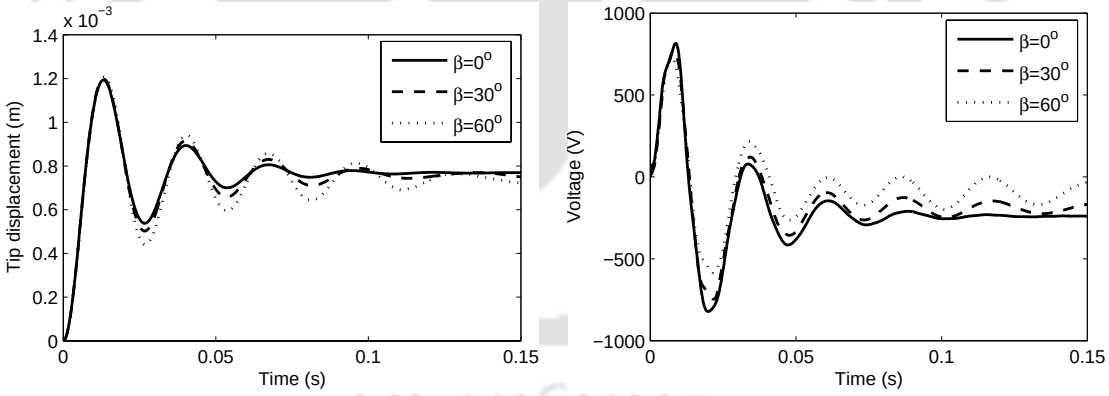

(a) Tip displacement (b) Actuator voltage

Figure 5.13 Controlled time responses for various pretwist angles at 200 rad/s rotational speed for a step loading ($\theta = 30^o$, $\gamma = 0^o$, $\eta = 1$)

5.5.2.2 Applying individual amplified voltage on each of the actuators

By using four actuators, it is found that maximum required control voltage on all actuators is well below the upper saturation voltage of 1500V. Therefore, four

sensors and actuators are considered in the analysis. Moreover, practical implementation is difficult if the number of actuators increases. In the following sections, effects of ply angle, taper parameter, pretwist angle and gyroscopic coupling is investigated by applying individual amplified voltage on each of the actuators.

5.5.2.3 Effect of ply angle

The bending vibration controlled time response for various ply angles is shown in Figure 5.14(a). Voltages applied on each of the actuators are presented in Figures 5.14 (b)-(e). It is observed that maximum tip displacement and applied control voltage reduces as the ply angle increases. Also, tip displacement and control voltage settling time for 90^o ply angle beam is less compared with 30^o ply angle beam.

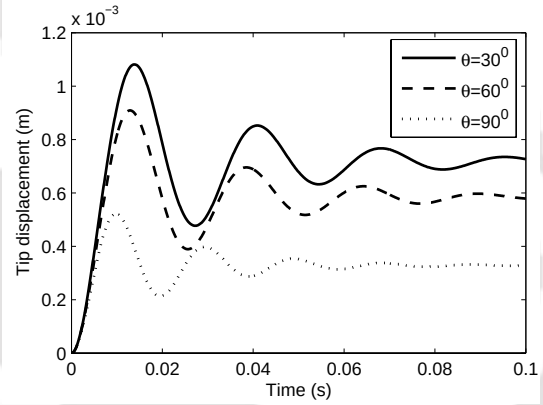

(a) Tip displacement

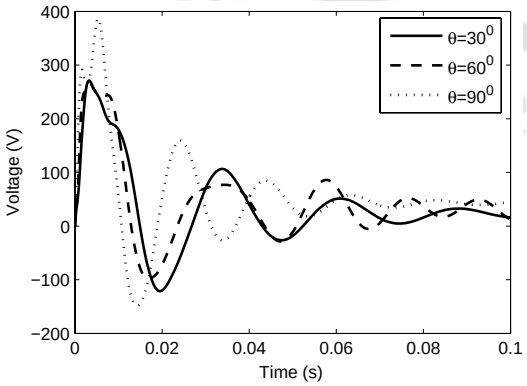

(b) Voltage on 1st actuator

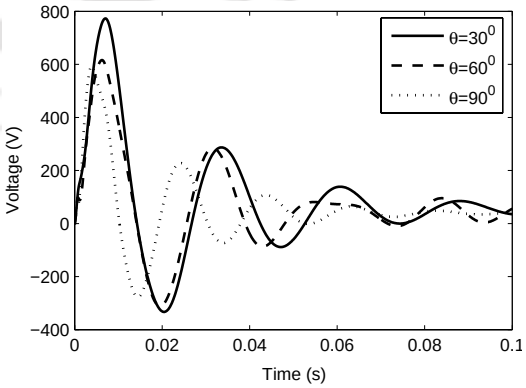

(c) Voltage on 2nd actuator

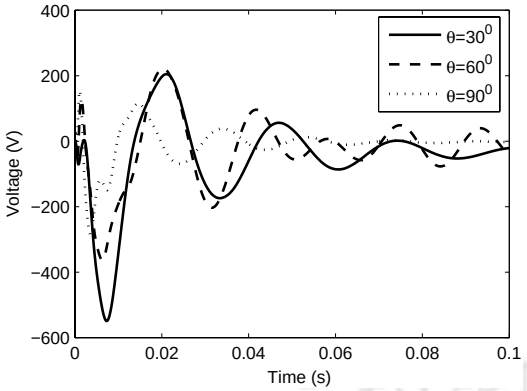

(d) Voltage on 3rd actuator

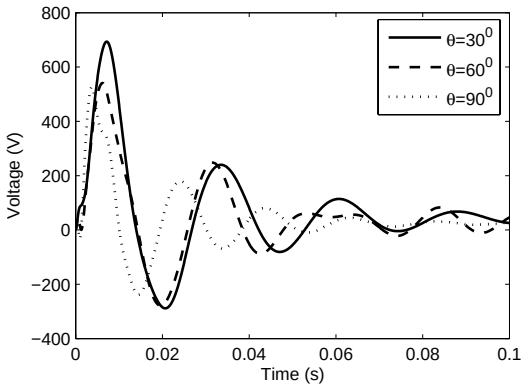

(e) Voltage on 4th actuator

Figure 5.14 Controlled time responses for three ply angle orientations for 200 rad/s rotational speed for a step loading ($\beta = 0^o$, $\gamma = 0^o$, $\eta = 1$)

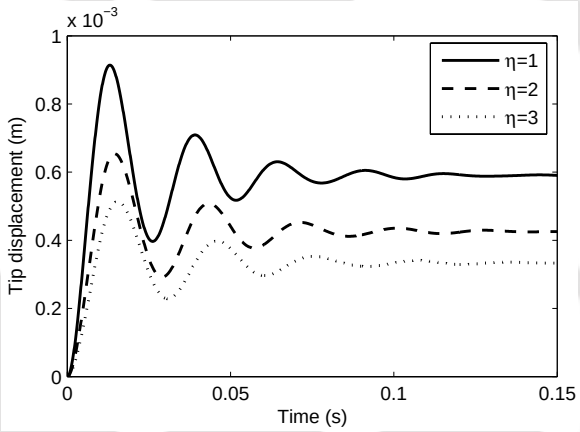

(a) Tip displacement

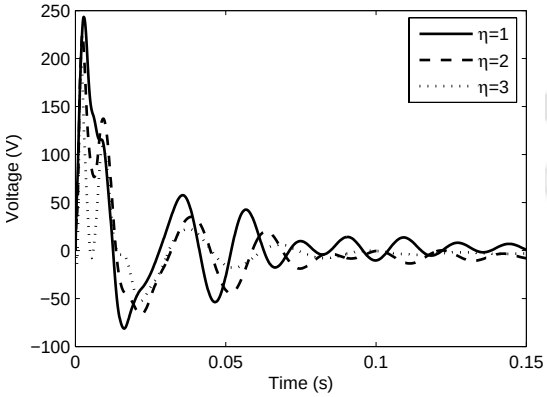

(b) Voltage on 1st actuator

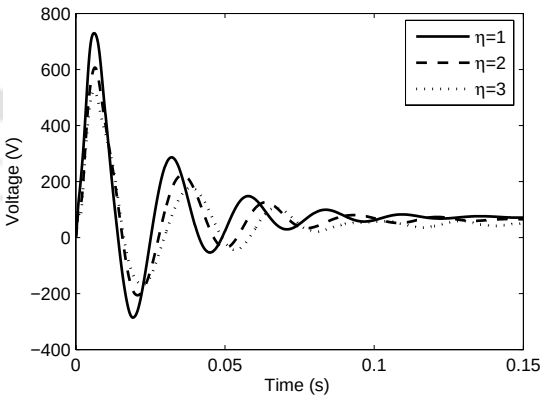

(c) Voltage on 2nd actuator

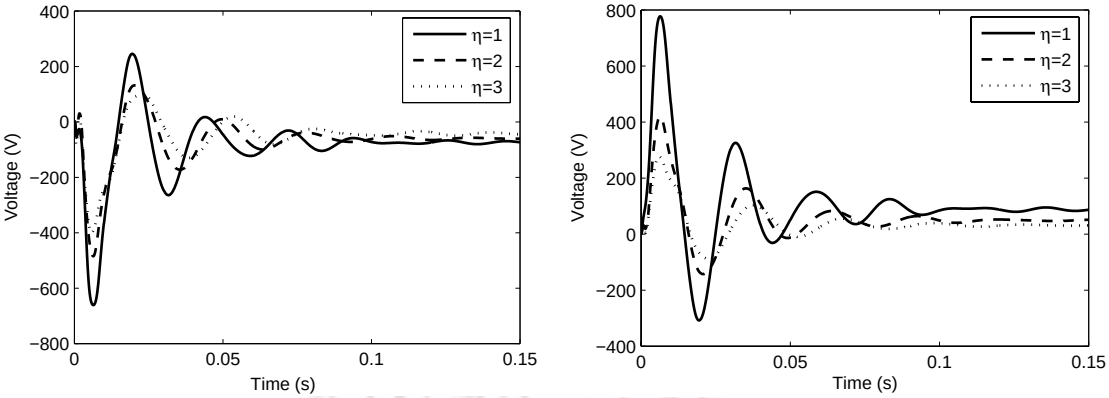

(d) Voltage on 3rd actuator

(e) Voltage on 4th actuator

Figure 5.15 Controlled time responses for various taper parameters for a 200 rad/s rotational speed for a step loading ($\theta = 30^o, \beta = 30^o, \gamma = 0^o$)

5.5.2.4 Effect of taper parameter

The effect of taper parameter on tip displacement and control voltage for a step forcing and rotational speed of 200 rad/s is presented in Figures 5.15(a) and 5.15(b)-(e) respectively. It is observed that increase in taper, decreases the maximum tip displacement and maximum voltage applied on the 1st, 3rd and 4th actuators. But, increase in taper, marginally increases applied voltage on the 2nd actuator. For the present configuration, voltages applied on the actuator are well below the upper limit of the MFC actuator voltage of 1500V.

5.5.2.5 Effect of pre-twist angle

Transient bending vibration control for 30^o, 60^o and 90^o pretwist angles is shown in Figure 5.16(a) and control voltages applied to the actuators are shown in Figures 5.16(b)-(e). It can be noticed that 30^o pretwisted beam settles a bit faster compared to 60^o and 90^o pretwisted beam. Applied peak voltages on the first three actuators for 30^o pretwisted beam are slightly higher, but settle a bit faster as compared to 60^o and 90^o pretwisted beam. However, for a fourth actuator, peak voltage for 60^o pretwisted beam is higher.

5.5.2.6 Effect of gyroscopic coupling

Figure 5.17 depicts the effect of gyroscopic coupling on the tip displacement response and actuator voltage on longitudinal vibration control of rotating beam. The difference between the results obtained by neglecting the effect of gyroscopic coupling and by including the gyroscopic coupling can be readily visualized from the graph. There is a phase lag in the time response when the gyroscopic coupling is neglected.

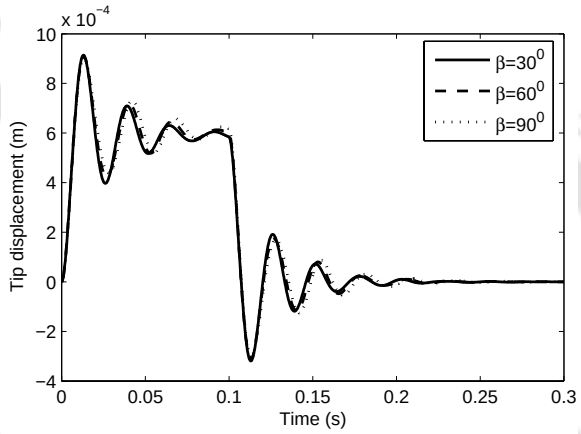

(a) Tip displacement

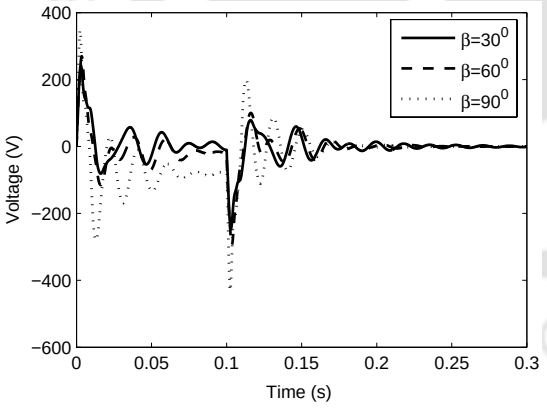

(b) Voltage on 1st actuator

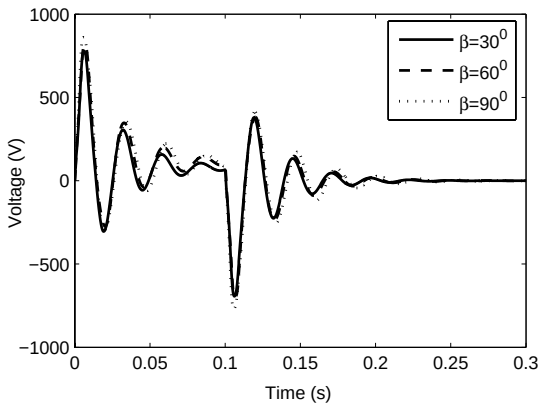

(c) Voltage on 2nd actuator

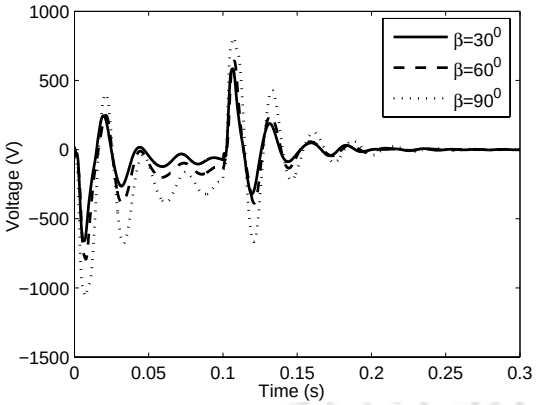

(d) Voltage on 3rd actuator

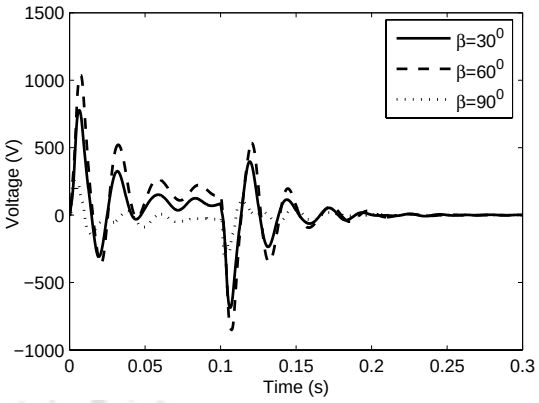

(e) Voltage on 4th actuator

Figure 5.16 Controlled time responses for three pretwist angles for a rectangular pulse ($\theta = 30^o$, $\beta = 0^o$, $\gamma = 0^o$, $\eta = 1$, $\Omega = 200$ rad/s)

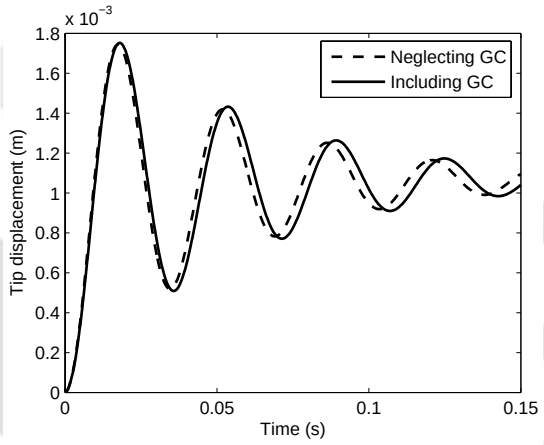

(a) Tip displacement

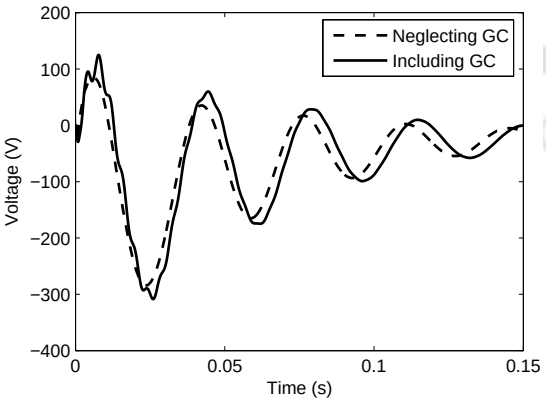

(b) Voltage on 1st actuator

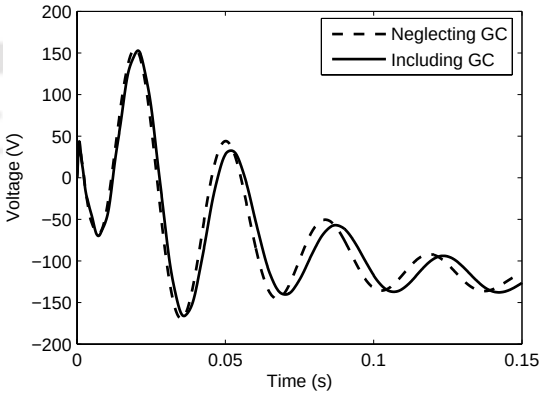

(c) Voltage on 2nd actuator

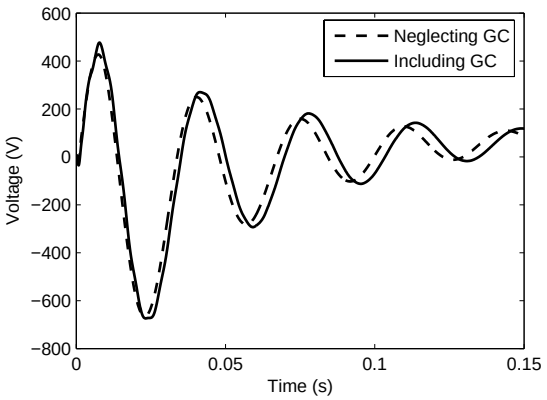

(d) Voltage on 3rd actuator

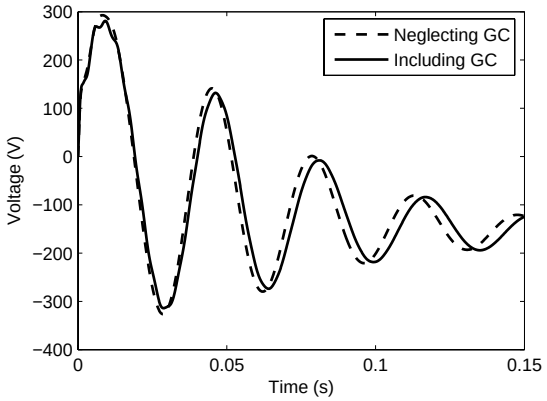

(e) Voltage on 4th actuator

Figure 5.17 Effect of gyroscopic coupling on controlled time responses for a step loading ($\theta = 0^o$, $\beta = 0^o$, $\gamma = 0^o$, $\eta = 1$)

5.6 Chapter summary

In this chapter, vibration control of rotating beams using MFC actuators and sensors is presented. First, the effects of mass and stiffness of piezoelectric actuators and sensors on the system vibration characteristics are studied. An optimal controller is designed using LQR and LQG algorithm for controlling the vibration due to external disturbances. The designed controller is then applied to a reduced order model of the rotating cantilever beam. Optimal performance of MFC actuators and sensors for vibration suppression of rotating composite beams is investigated. From the analysis, it is observed that MFC actuators and sensors can be successfully employed for vibration suppression of rotating beams.

- Inclusion of MFCs reduces the system natural frequencies significantly. Hence, passive effect of actuators and sensors cannot be neglected.
- Actuators at the tip are having negative feedback effect.
- Control effort by using MFCs is less compared to that of monolithic PVDF actuators and sensors.
- The effects of pretwist, taper and gyroscopic coupling on controlled responses are highlighted.

Chapter 6

Optimal placement of sensors and actuators

6.1 Introduction

It is important to optimize the locations of sensors and actuators so that the required control effort is minimum. In Chapter 5, the passive effects of sensors and actuators on free vibration characteristics are shown. Increase in the number of sensors and actuators changes the system mass and stiffness properties. Hence, it is important to optimize the locations of sensors and actuators so that passive effects of sensors and actuators can be reduced. The following sections describe the optimization problem statement, introduction to genetic algorithm and optimization procedure adopted in the present work.

6.2 Optimization problem statement

The optimal location of actuators in intelligent structures is an important area of research. By using optimal placement, number of actuators and sensors can be minimized or control effort can be minimized. The optimal control algorithm (LQR and LQG) minimizes the performance index defined in Eq. (5.7). The LQG control algorithm used in this chapter is discussed in Section 5.4.2 on Page No. 75. These control algorithms minimize the performance index for one set of locations of sensor and actuator arrangement. Hence, optimal locations of the actuators can be calculated by minimizing the trace identity of algebraic Riccati equation 'P' (Eq. 5.19). Similarly, optimal sensor locations can be obtained by minimizing the trace identity of filter Riccati equation 'S' (Eq. 5.21). Therefore, optimization problem for optimal actuator placement can be stated as,

Find ζ_a min $J = tr\{P\}$

Subject to (6.1)

$$\left|\zeta_a^i - \zeta_a^j\right| \geq w_{pa} \qquad i \neq j \tag{6.2}$$

$$\zeta_a^{lb} \leq \zeta_a \leq \zeta_a^{ub} \tag{6.3}$$

ζ_a is the design variable vector, superscripts lb and ub represent, lower and upper limits for design variables and w_{pa} is the width of the actuator.

Similarly, optimization problem for optimal sensor placement can be stated as,

Find ζ_s min $J = tr\{S\}$

Subject to (6.3)

$$\left|\zeta_s^i - \zeta_s^j\right| \geq w_{ps} \qquad i \neq j \tag{6.4}$$

$$\zeta_s^{lb} \leq \zeta_s \leq \zeta_s^{ub}$$

Linear constraints (Eqs. (6.2) and (6.4)) are imposed to place the actuators and sensors without overlapping. In Chapter 5, the control forces are obtained using optimal control theory by minimizing a quadratic performance index '*J*'. The considered performance index is a function of kinetic energy and potential energy of the system as well as required input control (Eq. 5.7). While determining optimal control by minimizing Eq. 5.7, the locations of sensors and actuators are fixed. Here, an attempt is made to optimize the location of sensors and actuators by minimizing the performance index.

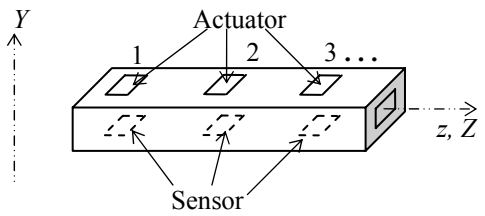

Figure 6.1 Distribution of sensors and actuators

Sensors and actuators near the tip of a cantilever beam are having negative effect on damping performance [Choi *et al.* (2006; 2007)]. Hence upper bound for sensors and actuators are considered as 70% of the length of the beam. The embedded sensors and actuators are numbered 1 to '*n*' starting from root as shown in Figure 6.1.

6.3 Genetic algorithm

Genetic algorithms are used in evolution search methods originally derived from the Darwinian evolutionary principle of ''survival-of-the-fittest''. Most traditional methods use point-by-point approach, where one solution is updated to the next in one iteration. The genetic algorithms on the other hand are parallel, guided random and adaptive search techniques. GAs have been recognized as a promising tool for numerical optimization of structural design problems. GAs as an optimization technique have been applied to optimal placement of sensors and actuators. The working principle of GAs are different from that of traditional optimization techniques. A GA starts with a random creation of population of strings and generates successive populations of strings that improve over time (Goldberg, 1989).

The steps involved in generation of new population consist of reproduction, crossover and mutation. These steps are shown in Figure 6.2.

1. Reproduction: In this process, fitness values of individual strings are evaluated. Good solutions from the population are identified based on evaluated fitness value. Strings with a higher fitness value have a probability of contributing one or more offspring in the next generation. Bad solutions from the population are eliminated so that multiple copies of good solutions can be placed in the population. Reproduction can be achieved in a number of ways such as, tournament selection, ranking selection, proportionate selection and henceforth.
2. Crossover: Crossover is the operator that produces new individuals (called as offspring) by randomly mating with the good individuals (called as parents)

generated in reproduction process. Simple crossover proceeds in two steps. First, a cutting position is chosen at random between the first and the last bit of the parents. The parents are divided into two parts using randomly selected cutting position. Then, the newly produced strings are mated at random. The two offspring are generated by each taking the first part from one parent and the second from the other. For example, in binary coding the strings 11001100 and 10001111 could be crossed over after the third bit in each of the parent to produce offspring such as 11001111 and 10001100.

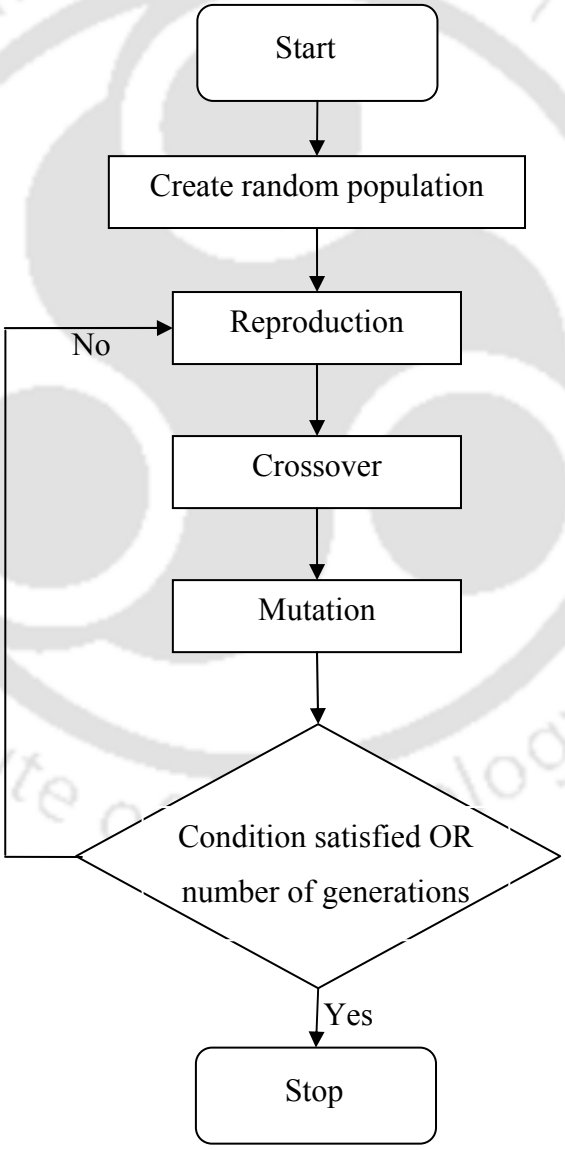

Figure 6.2 Flowchart for the Genetic algorithm operations

3. Mutation: Mutation is a random alteration of the value of a string position. It operates on a single individual with a small probability. With this process, one or more bits are chosen at random from the individual and changed into a different bit. In binary coding, this means changing 1 to 0 and vice versa. In GA, mutation probability is generally kept small, since higher occurrence rate would lead to a loss of important data.

Hence genetic algorithms do not require the evaluation of cost function derivatives. Therefore GAs can easily be applied to complex and/or discontinuous problems with a large number of parameters. Moreover, the GA simultaneously searches over a wide sampling of the search space and hence the solutions in general easily escape from a local minimum.

6.4 Optimization procedure

Since GAs are random in nature, the solution converges to the neighborhood of the global optimum. Solutions converge to an optimum number of generations or population size has to be kept very high. This increases the computation time.

The sequential quadratic programming (SQP) method uses a quadratic model for the objective function and a linear model for the constraints. Thus, SQP solves a quadratic program at each iteration. However, the minima obtained using SQP algorithm highly depends on the initial condition. Usually, this method converges to a local minima. In other words, the uniqueness of the solution obtained using SQP method has not been proved.

In the present study, the minimization problems (Eqs. (6.1) and (6.2)) are solved using the combination of genetic algorithm and sequential quadratic programming (SQP). As GAs are likely to converge closer to the global optima, the solutions obtained using GA are set as an initial condition to SQP algorithm. The flowchart of the optimal location calculations adopted in the study is shown in Figure 6.3.

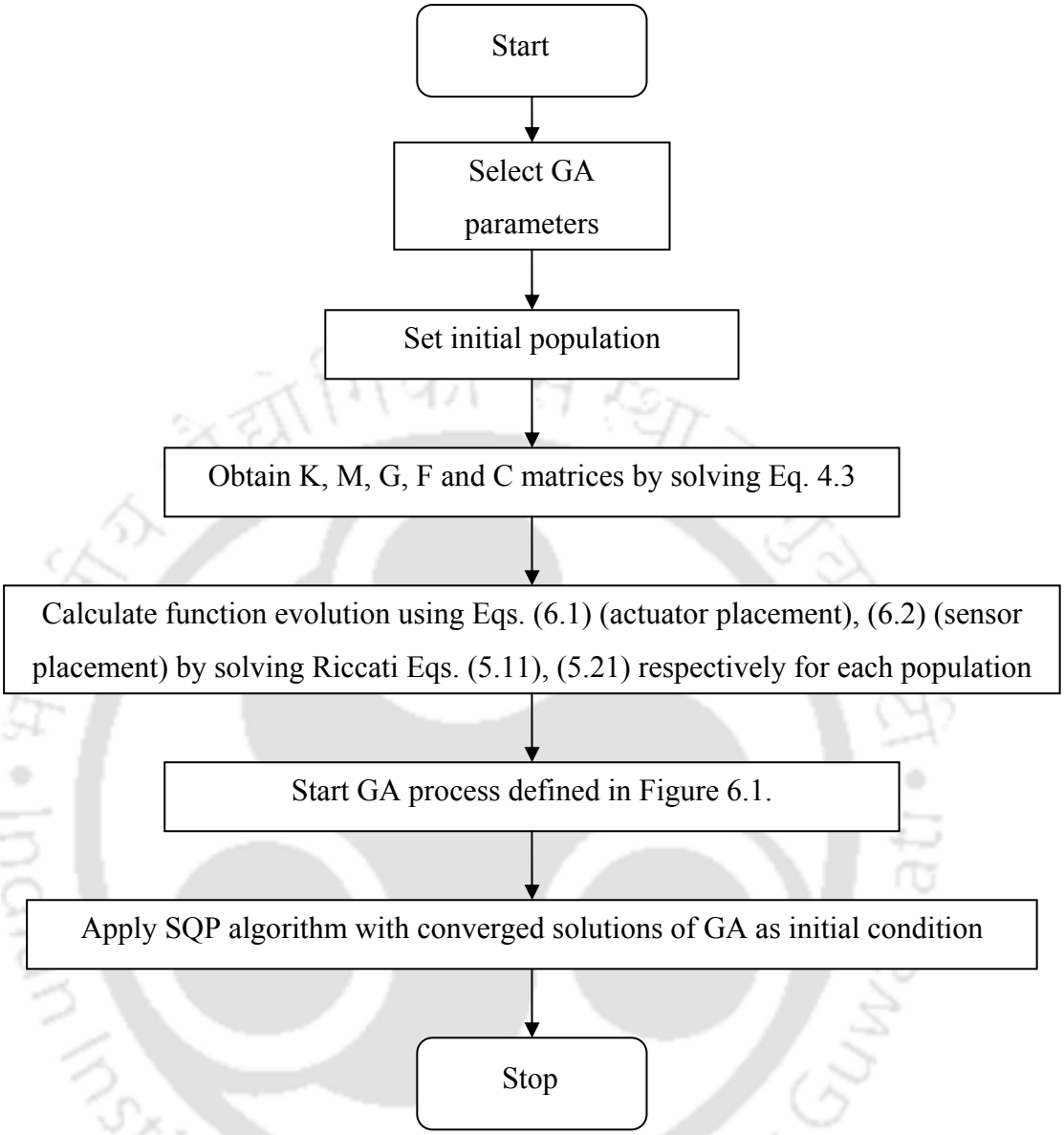

Figure 6.3 Flowchart for the optimization procedure adopted to optimize the locations of sensors and actuators

6.5 Numerical analysis

The beam considered is of graphite-epoxy material with properties $E_1 = 206.8$ GPa; $E_2 = 5.17$ GPa; $G_{12} = G_{13} = 3.1$ GPa; $G_{23} = 2.5511$ GPa; $\gamma_{12} = 0.25$; $\rho = 1528.15$ kg/m^3, with beam geometric configuration (Figure 4.1) $L = 2.023$ m; $R_o = 0.2023$ m; $h = 10.16$ mm; $c = 0.127$ m and $b = 0.0254$ m.

Properties of MFC actuators and sensors considered are: $E_1 = 30.4$ GPa; $E_2 = 15.86$ GPa; $G_{12} = G_{13} = 5.52$ GPa; $\gamma_{12} = 0.31$; $\rho = 8528$ kg/m^3; $d_{11} = 460$ pC/N; $d_{12} = -210$ pC/N; $A_p = (85\text{x}57)$ mm; $h_p = 1$ mm and $\theta^p = 0^o$.

Unless otherwise specified, numerical analysis is carried out using four actuators and four sensors with a symmetric six layers of $[\theta]_6$ ply angle lay up for passive host structure. Sensors and actuators near the tip of a cantilever beam are having negative effect on damping performance. Hence, co-located actuators and sensors are considered as equally distributed between 0 - 70% span of beam and for a rotational speed 200 rad/s. A step forcing in y-direction with magnitude of 500 kg/m and modal damping ratio ξ_i =0.01 is considered.

The evolutionary behavior of the GA is demonstrated in Figure 6.4. As the number of generations increases, the genetic algorithm produces better solutions until no improvement is observed. The final solution is therefore the optimal damper location. To reduce the computation time, the GA parameters are selected based on the convergence study of each parameter. Genetic algorithm parameters are selected by trial and error method by studying the convergence of fitness function. In Figure 6.4 convergence of optimum solution for three population sizes are shown. It is found from the study that, 30 numbers of population size is required to converge to the neighbourhood of an optimum. These parameters are

Population size	=	30,
Crossover rate	=	0.7,
Mutation rate	=	0.01,
Number of generations	=	50.

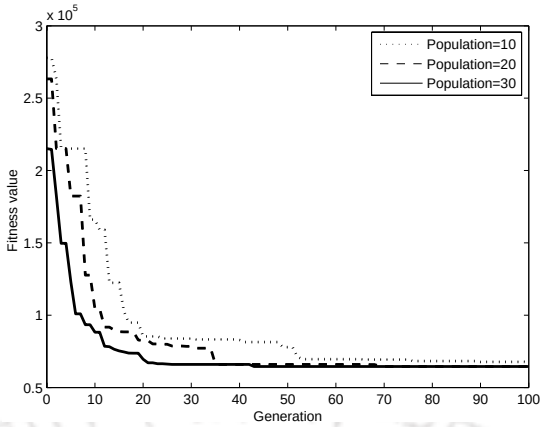

Figure 6.4. Convergence of fitness for different population sizes.

Figure 6.5(a) shows comparison of tip displacement for optimal placement and initial placement for untwisted rotating beam configuration. The beam is composed of ply angle orientation of 30^{o} with a rotational speed of 200 rad/s for an applied rectangular pulse. Genetically optimized locations of actuators and sensors for an untwisted beam configuration are listed in Tables 6.1 and 6.2 respectively and used as optimal locations in this study. Substantial reduction in settling time and tip displacement time can be observed for correctly located sensors and actuators.

Figures 6.5(b)-6.5(e) show applied voltages on the four actuators. Actuating voltage required on 1^{st}, 2^{nd} and 3^{rd} actuators which are optimally placed, requires less control effort. On the 4^{th} actuator, observed peak voltage is 468.64 volts for an optimal location as compared to 429 volts for initial placement. Later on, applied voltage reduces considerably in the case of optimal placement of actuators as time increases. Figure 6.6(a) shows comparison of tip displacement for optimal placement and initial placement for pretwisted rotating beam configuration. Genetically optimized locations of actuators and sensors for pretwisted beam configuration are listed in Tables 6.3 and 6.4 respectively and used as optimal locations in this study. Substantial reduction in settling time and tip displacement time can be observed for correctly located sensors and actuators. Figures 6.6(b)-6.6(e) show applied voltages on the four actuators. Actuating voltage required on 1^{st}, 3^{rd} and 4^{th} actuators which are optimally placed, requires less control effort. On the 2^{nd} actuator, it is observed that peak voltage is slightly higher for optimal location as

compared to initial placement. Hence, optimizing the locations of sensors and actuators plays a significant role in reducing settling time, tip displacement and control effort.

Figures 6.7(a) and 6.7(b) show closed loop poles of actuators and sensors respectively for untwisted beam configuration, with optimal and initial placement. It is found that as compared to initial placement, the optimal placement of closed loop poles are located deep inside left half plane. As the sensor and actuator location changes, closed loop poles start migrating to right half plane and thereby decreasing stability of the system. Similar nature is found in pretwisted beam configuration (Figure 6.7(c) and 6.7(d)).

Optimization of locations of sensors and actuators can be achieved by minimizing the trace identity of Riccati equation. This can be done using GA and SQP methods. Optimized locations of actuators and sensors obtained using GA are compared with SQP method. Tables 6.1 and 6.2 depict that performance of the GA is more accurate than SQP. The GA method yields minimum value of trace identity of Riccati equation as compared to SQP method. It is because the results obtained by using SQP depend on the initial guess of the objective function. Different initial guess yields different solution. In other words, optimal locations by SQP depend on initial guess. Hence, in the present study for finding optimal locations of actuators and sensors following methodology is adopted. The GA method which has been found to yield better results is used first for obtaining the optimal locations. These results are then used as initial guess for the SQP method. The results of optimal locations of actuators and sensors using GA method and SQP method with initial guess from GA are listed in Tables 6.3 and 6.4 respectively. Thus by using combination of GA and SQP, results are found to be better than results obtained by only GA. Untwisted beam with two rotational speeds and 30^{o} ply angle configuration is considered in this study. Optimal locations depend on various factors like rotational speed, pretwist angle, presetting angle and number of actuators used. It is observed from the present study that for a rotating beam, the optimally placed actuators and sensors shift towards the root of the beam as compared to their location for non-rotating beam. It has been observed that

optimized locations of sensors converge near the root of the beam (Table 6.4). It is because the strain energy of a rotating beam is maximum near the root of the beam.

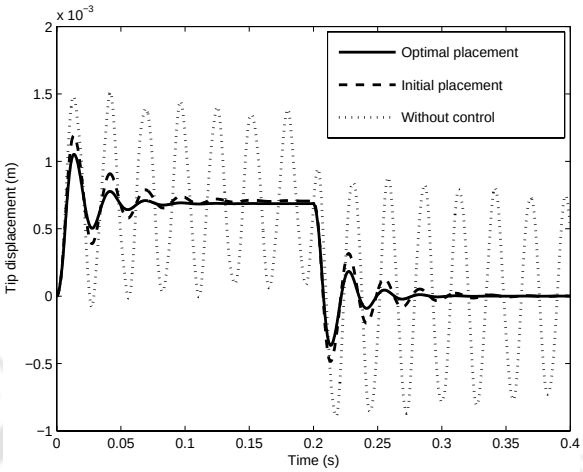

(a) Tip displacement

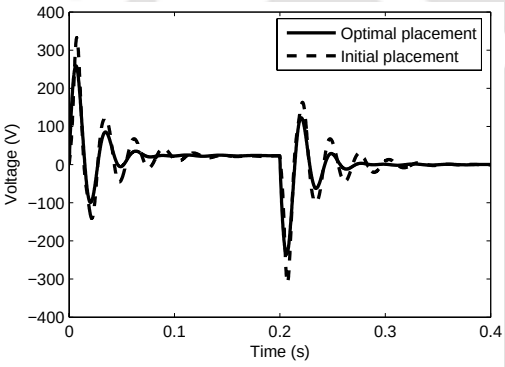

(b) Voltage on 1st actuator

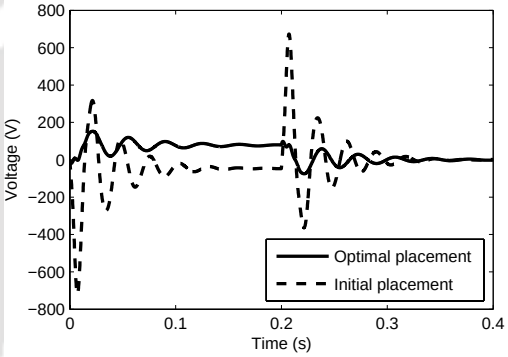

(c) Voltage on 2nd actuator

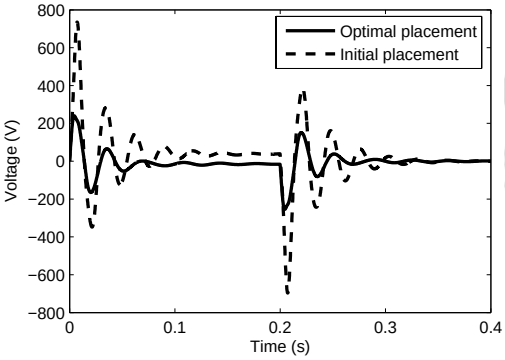

(d) Voltage on 3rd actuator

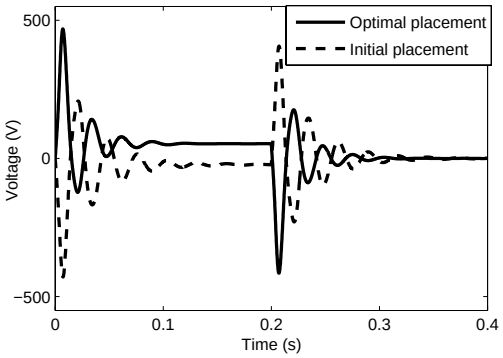

(e) Voltage on 4th actuator

Figure 6.5 Comparison of tip displacement and actuator voltage for optimal placement and initial placement for untwisted beam configuration for a rectangular loading

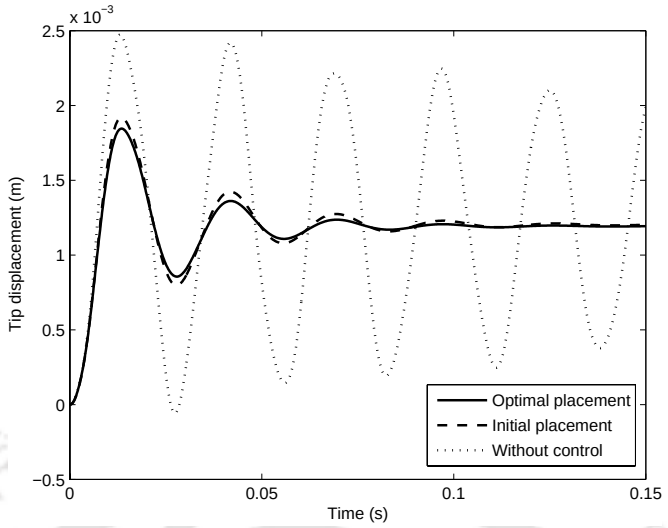

(a) Tip displacement

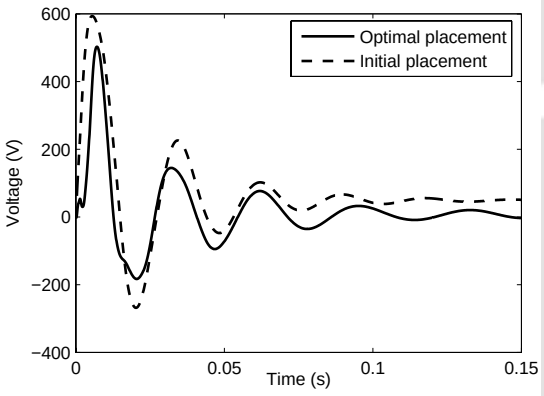

(b) Voltage on 1st actuator

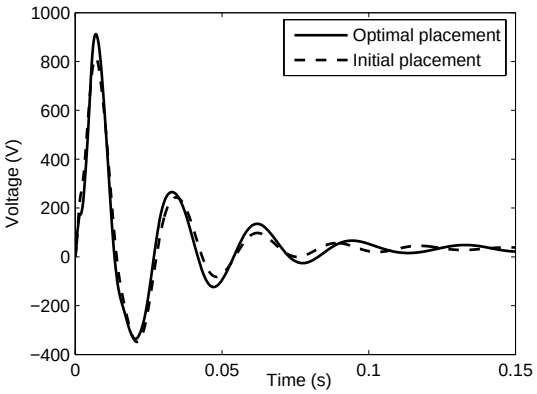

(c) Voltage on 2nd actuator

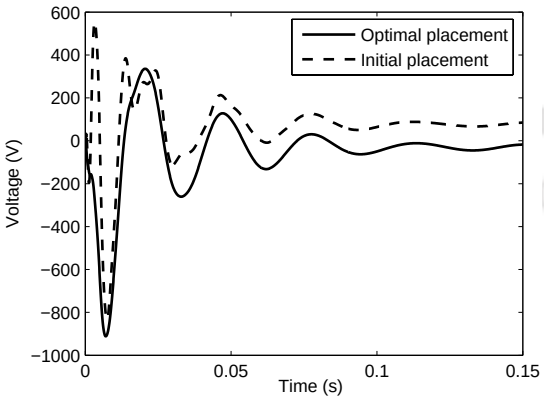

(d) Voltage on 3rd actuator

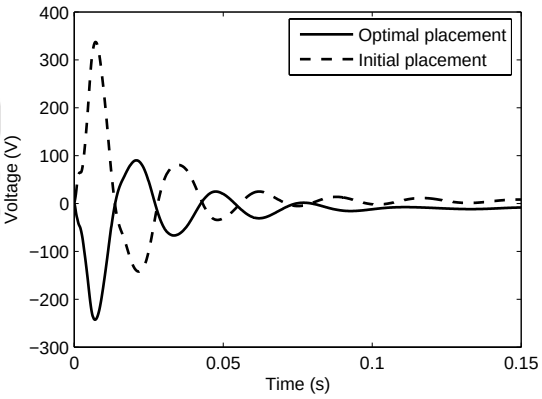

(e) Voltage on 4th actuator

Figure 6.6 Comparison of tip displacement and actuator voltage for optimal placement and initial placement for pretwisted beam configuration for a step loading ($\beta = 30^o$, $\gamma = 0^o$, $\eta = 1$, Ω=200 rad/s)

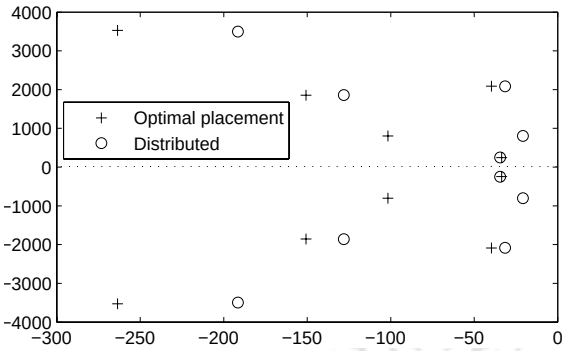

(a) Untwisted beam configuration actuator closed loop poles

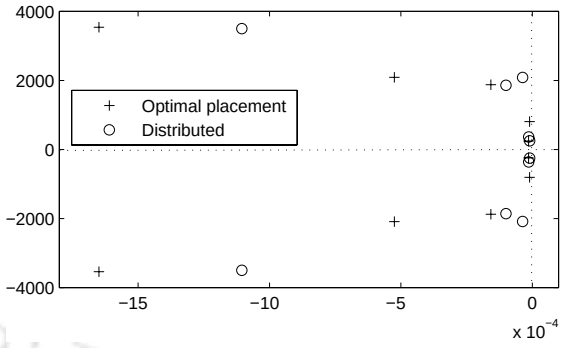

(b) Untwisted beam configuration sensor closed loop poles

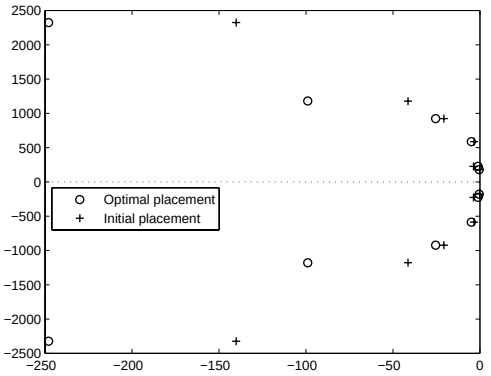

(c) Twisted beam configuration actuator closed loop poles

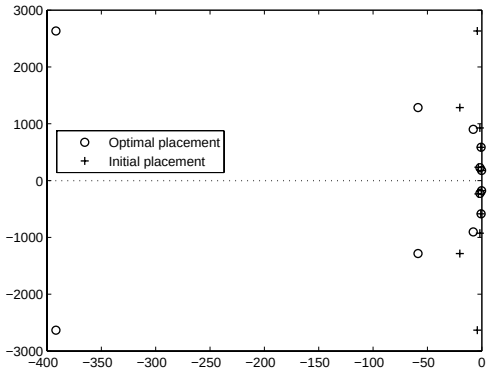

(d) Twisted beam configuration sensor closed loop poles

Figure 6.7 Controller and observer poles

Table 6.1 Comparison of converged actuator locations by GA and SQP algorithm using four actuators

Ω rad/s	GA		SQP	
	Optimal location (ζ_s) from root (in mts)	Fitness $tr(P)$	Optimal location (ζ_s) from root (in mts)	Fval $tr(P)$
0	0.06681	1.1212E+05	0.0423	2.9512e+006
	0.29322		0.2489	
	0.40208		1.0587	
	0.75989		1.1522	
200	0.06346	1.4700E+05	0.0667	1.3985e+006
	0.13075		0.8587	
	0.32191		1.0846	
	0.50643		1.1426	

Table 6.2 Comparison of converged sensor locations by GA and SQP algorithm using four sensors

Ω rad/s	GA		SQP	
	Optimal location (ζ_s) from root (in mts)	Fitness $tr(P)$	Optimal location (ζ_s) from root (in mts)	Fval $tr(P)$
0	0.04631	1.5571E+05	0.0069	2.4784e+005
	0.10642		0.4942	
	0.19911		0.7753	
	0.25941		0.8333	
200	0.00651	1.3954E+05	0.1995	3.5012e+005
	0.06617		0.2575	
	0.12418		1.1558	
	0.18248		1.2138	

Table 6.3 Converged optimal locations of actuators

No. of Actuators	Ω rad/s	Optimal Location (ζ_a) from root (in m) using GA	Fitness ($tr(P)$) using GA	Using SQP with converged GA solution as initial condition	
				Optimal Location (ζ_a) from root (in m)	Fval ($tr(P)$)
1	0	0.19412	1.1262E+05	0.09035	9.8106E+04
1	200	0.00238	1.4396E+05	0.00169	1.2352E+05
2	0	0.11622	1.1301E+05	0.00948	9.8359E+04
		0.79947		0.70742	
2	200	0.10520	1.4701E+05	0.00819	1.2857E+05
		0.19274		0.23037	
3	0	0.04476	1.1252E+05	0.00723	9.6366E+04
		0.15745		0.09537	
		0.80077		0.72871	
3	200	0.04464	1.5027E+05	0.00689	1.2775E+05
		0.17782		0.11208	
		0.29625		0.31782	
4	0	0.06681	1.1212E+05	0.00643	9.8908E+04
		0.29322		0.09705	
		0.40208		0.26906	
		0.75989		0.48163	
4	200	0.06346	1.4700E+05	0.00624	1.1972E+05
		0.13075		0.07821	
		0.32191		0.27287	
		0.50643		0.42733	

Table 6.4 Converged optimal locations of sensors

No. of Sensors	Ω rad/s	Optimal Location (ζ_a) from root (in m) using GA	Fitness ($tr(P)$) using GA	Using SQP with converged GA solution as initial condition	
				Optimal Location (ζ_a) from root (in m)	Fval ($tr(P)$)
1	0	0.18106	1.2639E+05	0.13944	1. 0836E+05
1	200	0.00603	1.3950E+05	0.00284	1. 1976E+05
2	0	0.00367	1.3816E+05	0.00166	1. 2309E+05
		0.06398		0.07777	
2	200	0.02893	1.5305E+05	0.01169	1. 3268E+05
		0.08731		0.08970	
3	0	0.00747	1.5968E+05	0.00502	1. 4483E+05
		0.06548		0.07273	
		0.20443		0.19580	
3	200	0.00130	1.3950E+05	0.00112	1. 2191E+05
		0.06217		0.05991	
		0.18200		0.17112	
4	0	0.04631	1.5571E+05	0.00938	1. 4468E+05
		0.10642		0.08163	
		0.19911		0.17236	
		0.25941		0.23492	
4	200	0.00651	1.3954E+05	0.00356	1. 2633E+05
		0.06617		0.06804	
		0.12418		0.11771	
		0.18248		0.19027	

6.6 Conclusions

In this chapter, importance of placement of sensors and actuators on the tip displacement and control effort has been studied. Results reveal that:

- Poles of correctly placed sensors and actuators shift deep inside the left half plane.
- Settling time, tip displacement and control effort can be reduced by placing the sensors and actuators at optimal locations.
- With increase in rotational speed, optimal location of sensors and actuators shifts towards the root.
- Locations of optimal sensors are found to converge near the root of the beam.
- Optimal locations depend on various factors like rotational speed, pretwist angle, presetting angle and number of actuators used.
- Optimal locations of sensors and actuators obtained by combination of GA and SQP are far superior to GA or SQP.

Chapter 7

Concluding remarks

7.1 Summary

In the present work, structural modelling of a higher order shearable rotating thin-walled composite cantilever beam using dynamic modelling method is presented. A non-Cartesian deformation variable (which represents arc length stretch) is used along with two Cartesian deformation variables. The governing system of equations is derived from Hamilton's principle and solution is obtained by extended Galerkin's method. Mathematical model includes non-classical effects generally exhibited by rotating composite beams such as anisotropy, heterogeneity, warping and transverse shear. The effects of centrifugal stiffening, centrifugal forces, rotary inertia and gyroscopic forces are also included.

Structural model of rotating pretwisted thin-walled composite beams is extended to include embedded MFC sensors and actuators. Passive effect of mass of actuators and sensors is included in the study. Optimal control problem is solved using LQR and LQG control algorithm. Optimal control for a box beam configuration is discussed in the numerical examples.

The locations of sensors and actuators are optimized using a combination of genetic algorithm and sequential quadratic programming algorithms.

Specifically, the major conclusions of this thesis include:

- In the structural part, higher order shearable structural model of rotating composite thin-walled beams using dynamic modeling method has been developed. It is clearly demonstrated that, by incorporating hybrid deformation variables gyroscopic coupling and centrifugal stiffening effects

can be captured in the mathematical model. The existing rotating thin-walled beam model is capable of providing consistent correlation with the experimental results and the available theoretical predictions. Free vibration characteristics for a box beam configuration including gyroscopic coupling are discussed in the numerical examples. The effects of pretwist, taper and presetting angle on free and forced vibration characteristics of rotating composite beams are emphasized.

- The modeling of rotating thin–walled composite beam with embedded MFC actuators is addressed in the thesis. Using LQR and LQG algorithms, it is shown that vibration reduction of the rotating beam responses can be achieved. The effects of pretwist, taper and presetting angle on controlled responses of rotating composite beams are highlighted. It is demonstrated that, control effort using MFC sensors and actuators is less compared to that of monolithic PZT sensors and actuators.
- Influence of gyroscopic coupling on free vibration, forced vibration and controlled response has been highlighted. It is found from the present study that the gyroscopic coupling between lagging – extension motion is having significant influence on vibration characteristics, hence cannot be neglected.
- Optimal locations of the actuators are calculated by minimizing the trace identity of algebraic Riccati equation '*P*'. The optimal sensor locations are obtained by minimizing the trace identity of filter Riccati equation '*S*' matrix. The optimization problems are solved using the combination of GA and SQP. Since GAs are likely to converge closer to the global optima, the solution obtained using GA is set as initial condition to SQP algorithm. An LQG control algorithm is used to suppress the transient bending vibrations. The performance of optimally placed actuators is compared with that of arbitrarily placed actuators.

7.2 Scope for future work

The emergence of new composite materials and new structural concepts has generated many significant challenges for the design and control of rotating thin–walled beams. There could be several ways in which the present research can be extended to emerging areas. Some of the issues which could be addressed for vibration and control of rotating beams are enumerated below.

- The present study focuses only on rotating thin-walled beams composed of composite material. In recent times, the functionally graded materials are attracting interest of academicians. The functionally graded materials are a kind of composites whose properties vary continuously and smoothly from a ceramic surface to a metallic surface in a specified direction of the structure. The work could be extended to vibration and control studies of rotating composite beams composed of functionally graded materials.
- Mathematical model can be generalized for arbitrary configuration, which can then be easily extended to other configurations like elliptical cross-section and airfoil cross-section beams. A finite element model can be developed for the derived equations of motion.
- The effect of temperature on free vibration, forced vibration and controlled response could be studied.
- Active vibration control problem could be studied using neural network based adaptive output feedback control.
- Nonlinearities exhibited by piezoelectric sensors and actuators, such as hysteresis could be another possible area of research.
- Optimal placement with optimal sizing of sensors and actuators could also be taken up.

Appendix

Appendix A: Global stiffness quantities for untwisted beam configuration

$$a_{11} = \oint K_{11} ds$$

$$a_{17} = \oint K_{15} \varphi ds$$

$$a_{22} = \oint \left(K_{11} x^{P^2} + 2 x^P l^P K_{12} + K_{22} l^{P^2} \right) ds$$

$$a_{25} = \oint \left(x^P l^P K_{15} + K_{25} l^{P^2} \right) ds$$

$$a_{33} = \oint \left(K_{11} y^{P^2} + 2 m^P y^P K_{12} + K_{22} m^{P^2} \right) ds$$

$$a_{34} = \oint \left(-m^P y^P K_{15} - K_{25} m^{P^2} \right) ds$$

$$a_{44} = \oint \left(m^{P^2} K_{55} + A_{44} l^{P^2} \right) ds$$

$$a_{55} = \oint \left(l^{P^2} K_{55} + A_{44} m^{P^2} \right) ds$$

$$a_{66} = \oint \left[K_{11} F_w^{P^2} + 2 K_{12} F_w^P a^P + K_{22} a^{P^2} \right] ds$$

$$a_{77} = \oint K_{55} \varphi^2 ds$$

Stiffness coefficients ($\tilde{a}_i$) arising due to higher shear deformable beam model

$$\tilde{a}_1 = \oint \left[-K_{57} \frac{8}{h^2} m^{P^2} + K_{77} \frac{16}{h^4} m^{P^2} - D_{44} \frac{8}{h^2} l^{P^2} + H_{44} \frac{16}{h^4} l^{P^2} \right] ds$$

$$\tilde{a}_2 = \oint \left[K_{71} \frac{4}{h^2} m^P y^P + \left(K_{45} \frac{4}{3h^2} + K_{72} \frac{4}{h^2} - K_{74} \frac{16}{3h^4} \right) m^{P^2} \right] ds$$

$$\tilde{a}_3 = \oint \left[K_{45} \frac{4}{3h^2} - K_{74} \frac{16}{3h^4} \right] m^{P^2} ds$$

$$\tilde{a}_4 = \oint \left[-K_{54} \frac{4}{3h^2} + K_{74} \frac{16}{3h^4} \right] l^{P^2} ds$$

$$\tilde{a}_5 = \oint \left[-K_{14} \frac{4}{3h^2} x^P l^P - \left(K_{42} \frac{4}{3h^2} - K_{44} \frac{16}{9h^4} \right) l^{P^2} \right] ds$$

$$\tilde{a}_6 = \oint \left[K_{44} \frac{16}{9h^4} \right] l^{P^2} ds$$

$$\tilde{a}_7 = \oint \left[\left(-K_{57} \frac{8}{h^2} + K_{77} \frac{16}{h^4} \right) l^{P^2} + \left(-D_{44} \frac{8}{h^2} + H_{44} \frac{16}{h^4} \right) m^{P^2} \right] ds$$

$$\tilde{a}_8 = \oint \left[-K_{71} \frac{4}{h^2} l^P x^P + \left(-K_{54} \frac{4}{3h^2} - K_{72} \frac{4}{h^2} + K_{74} \frac{16}{3h^4} \right) l^{P^2} \right] ds$$

$$\tilde{a}_9 = \oint \left[-K_{14} \frac{4}{3h^2} m^P y^P - \left(K_{42} \frac{4}{3h^2} - K_{44} \frac{16}{9h^4} \right) m^{P^2} \right] ds$$

$$\tilde{a}_{10} = \oint \left[K_{44} \frac{16}{9h^4} m^{P^2} ds \right]$$

$$\tilde{a}_{11} = \oint \left[-K_{14} \frac{8}{3h^2} l^P x^P + \left(-K_{42} \frac{8}{3h^2} + K_{44} \frac{16}{9h^4} \right) l^{P^2} \right] ds$$

$$\tilde{a}_{12} = \oint \left[-K_{14} \frac{8}{3h^2} m^P y^P + \left(-K_{42} \frac{8}{3h^2} + K_{44} \frac{16}{9h^4} \right) m^{P^2} \right] ds$$

$$\tilde{a}_{17} = a_{17} + \oint 2K_{16} ds$$

$$\tilde{a}_{77} = a_{77} + \oint \left(4K_{56}\varphi + 4K_{66} \right) ds$$

Appendix B: Global stiffness quantities for pretwisted beam configuration

$\tilde{a}_1 = \hat{a}_1 \cos^2\beta + \hat{a}_7 \sin^2\beta$; $\tilde{a}_2 = \hat{a}_2 \cos^2\beta - \hat{a}_8 \sin^2\beta$;

$\tilde{a}_3 = \hat{a}_3 \cos^2\beta - \hat{a}_4 \sin^2\beta$; $\tilde{a}_4 = \hat{a}_4 \cos^2\beta - \hat{a}_3 \sin^2\beta$;

$\tilde{a}_5 = \hat{a}_5 \cos^2\beta + \hat{a}_9 \sin^2\beta$; $\tilde{a}_6 = \hat{a}_6 \cos^2\beta + \hat{a}_{10} \sin^2\beta$;

$\tilde{a}_7 = \hat{a}_7 \cos^2\beta + \hat{a}_1 \sin^2\beta$; $\tilde{a}_8 = \hat{a}_8 \cos^2\beta - \hat{a}_2 \sin^2\beta$;

$\tilde{a}_9 = \hat{a}_9 \cos^2\beta + \hat{a}_5 \sin^2\beta$; $\tilde{a}_{10} = \hat{a}_{10} \cos^2\beta + \hat{a}_6 \sin^2\beta$;

$\tilde{a}_{11} = \hat{a}_{11} \cos^2\beta + \hat{a}_{12} \sin^2\beta$; $\tilde{a}_{12} = \hat{a}_{12} \cos^2\beta + \hat{a}_{11} \sin^2\beta$;

$\tilde{a}_{31} = \left(\hat{a}_1 - \hat{a}_7 \right) \sin\beta\cos\beta$; $\tilde{a}_{30} = \left(\hat{a}_2 + \hat{a}_8 \right) \sin\beta\cos\beta$;

$\tilde{a}_{32} = -\left(\hat{a}_3 + \hat{a}_4 \right) \sin\beta\cos\beta$; $\tilde{a}_{33} = \left(\hat{a}_{11} - \hat{a}_{12} \right) \sin\beta\cos\beta$;

$\tilde{a}_{34} = \left(\hat{a}_5 - \hat{a}_9\right)\sin\beta\cos\beta$; $\tilde{a}_{35} = \left(\hat{a}_6 - \hat{a}_{10}\right)\sin\beta\cos\beta$;

$a_{22} = a_{22}^u\cos^2\beta + a_{33}^u\sin^2\beta$; $a_{23} = \left(a_{22}^u - a_{33}^u\right)\sin\beta\cos\beta$;

$a_{33} = a_{33}^u\cos^2\beta + a_{22}^u\sin^2\beta$; $a_{34} = a_{34}^u\cos^2\beta - a_{25}^u\sin^2\beta$;

$a_{42} = -\left(a_{25}^u + a_{34}^u\right)\sin\beta\cos\beta = -a_{35}$; $a_{44} = a_{44}^u\cos^2\beta + a_{55}^u\sin^2\beta$;

$a_{45} = \left(a_{44}^u - a_{55}^u\right)\sin\beta\cos\beta$; $a_{55} = a_{55}^u\cos^2\beta + a_{44}^u\sin^2\beta$;

$a_{25} = a_{25}^u\cos^2\beta - a_{34}^u\sin^2\beta$;

where,

$m_\beta = \cos\beta$; $l_\beta = \sin\beta$; $a_{ij}^u = a_{ij}$, $\hat{a}_{ij} = \tilde{a}_{ij}$ of untwisted beam, which are defined in Appendix A

Appendix C: Inertia quantities

$$\tilde{I}_{yy}^P,\ \tilde{I}_{xx}^P,\ \tilde{I}_{mm}^P,\ \tilde{I}_{ll}^P,\ \tilde{I}_{FF}^P,\ \tilde{I}_{aa}^P = \oint\left\{x^{P^2},\ y^{P^2},\ l^{P^2},\ m^{P^2},\ F_w^{P^2},\ a^{P^2}\right\}\mathrm{d}s$$

$$\left(m_0,\ m_2,\ m_4,\ m_6\right) = \sum_{K=1}^{N}\int_{h(K)} e^{(K)}\left(1,\ n^2,\ n^4,\ n^6\right)dn$$

$\tilde{I}_P^P = \tilde{I}_{yy}^P + \tilde{I}_{xx}^P$; $I_P^P = m_0\tilde{I}_P^P$;

$\hat{I}_P^P = \dfrac{I_P^P}{\beta(z)}$; $I_{yy}^P = m_0\tilde{I}_{yy}^P + m_2\tilde{I}_{mm}^P$;

$I_{xx}^P = m_0\tilde{I}_{xx}^P + m_2\tilde{I}_{ll}^P$; $I_{xx}^{P^0} = m_0\tilde{I}_{xx}^P$;

$I_{yy}^{P^0} = m_0\tilde{I}_{yy}^P$; $I_{ww}^P = m_0\tilde{I}_{FF}^P + m_2\tilde{I}_{aa}^P$;

$\lambda = \dfrac{4}{3h^2}$; $b_1 = m_0\oint ds$;

$\bar{I} = m_\beta^2\tilde{I}_{mm}^P + l_\beta^2\tilde{I}_{ll}^P$; $\hat{I} = m_\beta l_\beta\left(\tilde{I}_{mm}^P - \tilde{I}_{ll}^P\right)$;

$I_1 = 16\dfrac{m_6}{9h^4}\bar{I}$; $I_2 = 16\dfrac{m_6}{9h^4}\left(l_\beta^2\tilde{I}_{mm}^P + m_\beta^2\tilde{I}_{ll}^P\right)$;

$$I_3 = \frac{4m_4}{3h^2}\bar{I}\,; \qquad I_4 = \frac{4m_4}{3h^2}\left(l_\beta^2 \tilde{I}_{mm}^P + m_\beta^2 \tilde{I}_{ll}^P\right);$$

$$I_5 = 16\frac{m_6}{9h^4}\hat{I}\,; \qquad I_6 = \frac{4m_4}{3h^2}\hat{I}\,;$$

$$I_7 = m_\beta^2 I^P{}_{yy} + l_\beta^2 I_{xx}^P\,; \qquad I_8 = l_\beta^2 I^P{}_{yy} + m_\beta^2 I_{xx}^P\,;$$

$$I_9 = m_\beta l_\beta \left(I_{yy}^P - I_{xx}^P\right); \qquad I_{10} = I_{yy}^P + I_{xx}^P\,;$$

for untwisted beam $m_\beta = \cos\beta = 1;\;\; l_\beta = \sin\beta = 0;$

References

Alkahe, J and Rand, O. (2000), Analytic extraction of the elastic coupling mechanisms in composite blades, *Composite Structures*, Vol. 49, pp. 399-413.

Ang, K. K., Wang, S. Y. and Quek, S. T. (2002), Weighted energy linear quadratic regulator vibration control of piezoelectric composite plates, *Smart Materials and Structures*, Vol. 11, pp. 98-106.

Azzouz, M. S., Mei, C., Bevan, J. S. and Ro, J. J. (2001), Finite element modeling of MFC/AFC actuators and performance of MFC, *Journal of Intelligent Materials Systems and Structures*, Vol. 12, pp. 601-612.

Bai, M. R. and Lin, G. M. (1996), The development of a DSP-based active small amplitude vibration control system for flexible beams by using the LQG algorithms and intelligent materials, *Journal of Sound and Vibration*, Vol. 198(4), pp. 411-427.

Bailey, T. and Hubbard, J. E. Jr (1985), Distributed piezoelectric-polymer active vibration control of a cantilever beam, *Journal of Guidance*, Vol. 8, pp. 605-611.

Bathe, K. and Wilson, E. (1976), Numerical methods in finite element analysis, *Prentice-Hall, Inc., Englewood Cliffs*, N. J.

Baz, A. and Poh, S. (1988), Performance of an active control system with piezoelectric actuators, *Journal of Sound and Vibration*, Vol. 126, No. 2, pp. 327-343.

Benjeddou, A. (2000), Advances in piezoelectric finite element modeling of adaptive structural elements: a survey, *Computers and Structures*, Vol. 76, pp. 347-363.

Bent, A. A. (1997), Active fiber composites for structural actuation, *Ph.D. Thesis, Massachusetts Institute of Technology, Cambridge, MA.*

Bent, A. A., Hagood, N. W. and Rodgers, J. P. (1995), Anisotropic actuation with piezoelectric fiber composite, *Journal of Intelligent Material Systems and Structures*, Vol. 6, No. 5, pp. 338-349.

Bielawa, R. L. (1992), Rotary wing structural dynamics and aeroelasticity, *American Institute of Aeronautics and Astronautics Education Series, Washington, D. C., American Institute of Aeronautics and Astronautics Inc.*

Brockmann, T. H. and Lammering, R. (2006), Beam finite elements for rotating piezoelectric fiber composite structures, *Journal of Intelligent Material Systems and Structures*, Vol. 17, pp. 431–447.

Brons, M., Hjorth P. G. and Kliem, W. (1996), Coriolis effects in the dynamics of a rotating elastic structure, *Acta Mechanica*, Vol. 116, pp. 223-227.

Cai, G. P., Hong, J. Z. and Yang, S. X. (2005), Dynamic analysis of a flexible hub-beam system with tip mass, *Mechanics Research Communications*, Vol. 32, pp. 173-190.

Carnegie, W. and Thomas, J. (1972), The effects of shear deformation and rotary inertia on the lateral frequencies of cantilever beams in bending, *Journal of Engineering for Industry—ASME Transactions*, Vol. 94, pp. 267–278.

Cesnik, C. E. S. and Morales, M. O. (2001), Active beam cross-sectional modeling, *Journal of Intelligent Materials Systems and Structures*, Vol. 12, pp. 483-496.

Chakraborty, A., Roy, M. D. and Gopalakrishnan, S. (2002), Finite element analysis of free vibration and wave propogation in asymmetric composite beams with structural discontinuities, *Composite Structures*, Vol. 55, pp. 23-36.

Chandiramani, N. K., Librescu, L. I. and Shete, C. D. (2002), On the free-vibration of rotating composite beams using a higher-order shear formulation, *Aerospace Science and Technology*, Vol. 6, pp. 545-561.

Chandiramani, N. K., Librescu, L. I, Saxena, V. and Kumar, A. (2004a), Optimal vibration control of a rotating composite beam with distributed piezoelectric sensing and actuation, *Smart materials and structures*, Vol. 13, pp. 1-10.

Chandiramani, N. K., Shete, C. D. and Librescu, L. I. (2003), Vibration of higher-order-shearable pretwisted rotating composite blades, *International Journal of Mechanical Sciences*, Vol. 45, No. 12, pp. 2017-2041.

Chandiramani, N. K., Shete, C. D. and Librescu, L. I. (2004b), Optimal control of pretwisted shearable smart composite rotor blades, *American Institute of Aeronautics and Astronautics Journal*, pp. 01-10.

Chandra, R. and Chopra, I. (1992), Experimental-theoretical investigation of the vibration characteristics of rotating composite box beams, *Journal of Aircraft*, Vol. 29, No. 4, pp. 657-663.

Chandra, R., Stemple, A. D. and Chopra, I. (1990), Thin-walled composite beams under bending, torsional, and extensional loads, *Journal of Aircraft*, Vol. 27, No. 7, pp. 619-625.

Chen, X. and Kareem, A. (2003), Curve veering of eigenvalue loci of bridges with aeroelastic effects, *Journal of Engineering Mechanics*, Vol. 129, No. 2, pp. 146-159.

Choi, S. B. (1994), Alleviation of chattering in flexible beam control via piezofilm actuator and sensor, *American Institute of Aeronautics and Astronautics Journal*, Vol. 33, No. 3, pp. 564-567.

Choi, S. C., Park, J. S and Kim, J. H. (2006), Active damping of rotating composite thin walled beams using MFC actuators and PVDF sensors, *Composite Structures*, Vol. 76, pp. 362-374.

Choi, S. C., Park, J. S. and Kim, J. H. (2007), Vibration control of pretwisted rotating composite thin walled beams with piezoelectric fiber composites, *Journal of Sound and Vibration*, Vol. 300, pp. 176-196.

Chung, J. and Yoo, H. H. (2002), Dynamic analysis of a rotating cantilever beam by using the finite element method, *Journal of Sound and Vibration*, Vol. 249, No. 1, pp. 147-64.

Demetriou, M. A. (2000), A numerical algorithm for the optimal placement of actuators and sensors for flexible structures, *Proceedings of the American Control Conference, Chicago, pp. 2290-2294.*

Denoyer, K. K. and Kwak, M. K. (1996), Dynamic modeling and vibration suppression of a slewing structure utilizing piezoelectric sensors and actuators, *Journal of Sound and Vibration*, Vol. 189, No. 1, pp. 13-31.

Du, H., Lim, M. K and Liew, K. M. (1994), A power series solution for vibration of a rotating Timoshenko beam, *Journal of Sound and Vibration*, Vol. 175, No. 4, pp. 505-523.

Ekel'chik, V. S. and Ryabov, V. M. (1996), Various methods of determining the natural frequencies and damping of composite cantilever plates, *Mechanics of Composite Materials*, Vol. 32, No. 6, pp. 524-530.

Frank, L. L. and Vassilis, L. S. (1995), Optimal control. *John Wiley & Sons, Inc., Second Edition*.

Ganesan, R. and Zabihollah, A (2007), Vibration analysis of tapered composite beams using a higher-order finite element. Part I: Formulation, *Composite Structures*, Vol. 77, pp. 306-318.

Hagood, N. W., and Bent, A. A. (1993), Development of piezoelectric fiber composites for structural actuation, *Proceedings 34th AIAA/ASME/ASCE/AHS/ASC Structures, Structural Dynamics, and Materials Conferences, American Institute of Aeronautics and Astronautics Paper 93-1717, La Jolla, CA.*

Han, J. H. and Lee, I. (1999), Optimal placement of piezoelectric sensors and actuators for vibration control of a composite plate using genetic algorithms, *Smart Materials and Structures*, Vol. 8, pp. 257-267.

Hashemi, S. M. and M. J. Richard (2001), Natural frequencies of rotating uniform beams with Coriolis effects, *Transactions of the ASME*, Vol. 123, pp. 444-455.

Henry, A. S, Gyuhae, P. and Daniel, J. I. (2004), An investigation into the performance of macro fiber composites for sensing and structural vibration applications, *Mechanical Systems and Signal Processing*, Vol. 18, pp. 683–697.

Hiramoto, K., Doki, H. and Obinata, G. (2000), Optimal sensor\actuator placement for active vibration control using explicit solution of algebraic Riccati equation, *Journal of Sound and Vibration*, Vol. 229, No.5, pp. 1057-1075.

Hodges, D. H. and Rutkowski, M. J. (1981), Free-vibration analysis of rotating beams by a variable-order finite-element method, *American Institute of Aeronautics and Astronautics Journal*, Vol. 19, No. 11, pp. 1459-1466.

Hu, Q. and Ma, G. (2005), Maneuvers and vibration suppression of flexible spacecraft with input nonlinearities, *Aircraft Engineering and Aerospace Technology, An International Journal*, Vol. 77/5, pp. 388-400.

Hwu, C., Chang, W. C. and Gai, H. S. (2004), Vibration suppression of composite sandwich beams, *Journal of Sound and Vibration*, Vol. 272, pp. 01-20.

Jha, A. K. (2002), Vibration analysis and control of an inflatable toroidal satellite component using piezoelectric actuators and sensors, *Ph.D thesis, Department of Mechanical Engineering, Virginia Polytechnic Institute and State University*.

Jung, S. N., Nagaraj, V. T. and Chopra, I. (1999), Assessment of composite rotor blade modeling techniques, *AHS International Meeting on Advanced Rotorcraft Technology and Diaster Relief, Japan*, pp. 188-205.

Jung, S. N., Nagaraj, V. T. and Chopra, I. (2001), Refined structural dynamics model for composite rotor blades, *American Institute of Aeronautics and Astronautics Journal*, Vol. 39, No. 2, pp. 339-348.

Kane, T. R., Ryan, R. R. and Banerjee, A. K. (1987), Dynamics of a cantilever beam attached to a moving base, *Journal of Guidance*, Vol. 10, No. 2, pp. 139-151

Kar, R. C. and Neogy, S. (1989), Stability of a rotating, pre-twisted, non-uniform cantilever beam with tip mass and thermal gradient subjected to a non-conservative force, *Computers & Structures*, Vol. 33. No. 2, pp. 499-507.

Kar, R. C. and Sujata, T. (I992), Dynamic stability of a rotating, pretwisted and preconed cantilever beam including Coriolis effects, *Computers & Structures*, Vol. 42, No. 5, pp. 741-750.

Karagulle, H., Malgaca, L and Oktem, H. F. (2004), Analysis of active vibration control in smart structures by ANSYS, *Smart Materials and Structures*, Vol. 13, pp. 661-667.

Lam, K. Y., Peng, X. Q., Liu, G. R. and Reddy, J. N. (1997), A finite element model for piezoelectric composite laminates, *Smart Materials and Structures*, Vol. 6, pp. 583-591.

Lammering, R., Jia, J. and Rogers, C. A. (1994), Optimal placement of piezoelectric actuators in adaptive truss structures, *Journal of Sound and Vibration*, Vol. 171(1), pp. 67-85.

Liu, W., Hou, Z. and Demetriou, M. A. (2006), A computational scheme for the optimal sensor\actuator placement of flexible structures using spatial H2 measures, *Mechanical Systems and Signal Processing*, Vol. 20, pp. 881-895.

Liu, D. K., Yang, Y. L. and Li, Q. S. (2003), Optimum positioning of actuators in tall buildings using genetic algorithm, *Computers and Structures*, Vol. 81, pp. 2823-2827.

Lee, H. K., Chen, S. T. and Lee, A. C. (1996), Optimal control of vibration suppression in flexible systems via dislocated sensor\actuator positioning, *The Franklin Institute*, Vol. 333(B), No. 5, pp. 789-802.

Lee, S. J., Reddy, J. N. and Rostam-Abadi, F. (2004), Transient analysis of laminated composite plates with embedded smart-material layers, *Finite Elements in Analysis and Design*, Vol. 40, pp. 463-483.

Lee, S. Y. and Lin, S. M. (1994), Bending vibrations of rotating non-uniform Timoshenko beams with an elastically restrained root, *Journal of Applied Mechanics*, Vol. 61, pp. 949-955.

Li, J., Shen, R., Hua, H. and Jin, X. (2004), Bending-torsional coupled dynamic response of axially loaded composite Timosenko thin-walled beam with closed cross-section, *Composite Structures*, Vol. 64, pp. 23-35.

Librescu, L. I. and Na, S (2001), Active vibration control of doubly tapered thin-walled beams using piezoelectric actuation, *Thin-walled Structures*, Vol. 39, pp. 65-82.

Librescu, L. I. and Na, S. (2005), Comparative study on vibration control methodologies applied to adaptive thin-walled anisotropic cantilevers, *European Journal of Mechanics A/Solids*, Vol. 24, pp. 661-675.

Mallik, N. and Ray, M. C. (2004), Exact solutions for the analysis of piezoelectric fibre reinforced composites as distributed actuators for smart composite plates, *International Journal of Mechanics and Materials in Design*, Vol. 1, pp. 347-364.

McGee, O. G. (1987), Finite element analysis of flexible rotating blades, *NASA Technical Memorandum 89906.*

Mitra, M. and Gopalakrishnan, S. (2006), Wavelet based spectral finite element for analysis of coupled wave propagation in higher order composite beams, *Composite Structures*, Vol. 73, pp. 263-277.

Mitra, M., Gopalakrishnan, S. and Bhat, M. S. (2004a), A new super convergent thin walled composite beam element for analysis of box beam structures, *International Journal of Solids and Structures*, Vol. 41, pp. 1491-1518.

Mitra, M., Gopalakrishnan, S. and Bhat, M. S (2004b), Vibration control in a composite box beam with piezoelectric actuators, *Smart Materials and Structures*, Vol. 13, No. 4, pp. 676-690.

Mota, S. D., Ribeiro, R., Rodrigues, J. D. and Monteiro, V. M. A. P. (2004), The application of genetic algorithms for shape control with piezoelectric patches-an experimental comparison, *Smart Materials and Structures*, Vol. 13, pp. 220-226.

Na, S. and Librescu, L. I. (2000), Optimal vibration control of thin-walled anisotropic cantilevers exposed to blast loadings, *Journal of Guidance, Control and Dynamics*, Vol. No. 3, pp. 491-500.

Na, S., Librescu, L. I. and Shim, J. K. (2003), Modeling and bending vibration control of non-uniform thin-walled rotating beams incorporating adaptive capabilities, *International Journal of Mechanical Sciences*, Vol. 45, pp. 1347-1367.

Na, S., Librescu, L. I., Rim, S. N. and Yoon, G. C. (2005), Vibration and dynamic response control of non-uniform composite rotating blades, *International Journal of Rotating Machinery, Article 13807*, pp. 01-09.

Na, S., Yoon, H. and Librescu, L. I. (2006), Effect of taper ratio on vibration and stability of a composite thin-walled spinning shaft, *Thin-walled Structures*, Vol. 44, pp. 362-371.

Nam, C., Kim, Y. and Weisshaar, T. A. (1996), Optimal sizing and placement of piezo-actuators for active flutter suppression, *Smart Materials and Structures*, Vol. 5, pp. 216-224.

Narayanan, S. and Balamurugan, V. (2003), Finite element modeling of piezolaminated smart structures for active vibration control with distributed sensors and actuators, *Journal of Sound and Vibration*, Vol. 262, pp. 529-562.

Nguyen, C. H and Kornmann, X. (2006), A comparison of dynamic piezoactuation of fibre-based actuators and conventional PZT patches, *Journal of Intelligent Materials Systems and Structures*, Vol., pp. 45-55.

Ning, H. H. (2004), Optimal number and placements of piezoelectric patch actuators in structural active vibration control, *Engineering Computations*, Vol. 21, No. 6, pp. 651-665.

Oh, S. Y, Song, O. and Librescu, L. I. (2003), Effects of pretwist and presetting on coupled bending vibrations of rotating thin-walled composite beams, *International Journal of Solids and Structures*, Vol. 40, pp. 1203-1224.

Park, J. S. and Kim, J. H. (2004), Suppression of aero-thermal large deflections and snap-through behaviors of composite panels using macro fibre composite actuators, *Smart Materials and Structures*, Vol. 13, pp. 1448-1459.

Park, J. E. and Kim, J. H. (2005), Analytical development of single crystal macro fibre composites actuators for active twist rotor blades, *Smart Materials and Structures*, Vol. 14, pp. 745-753.

Rao, J. N., Lentzen, S. and Schmidt, R. (2006), Genetically optimised placement of piezoelectric sensor arrays: linear and nonlinear transient analysis, *High-Performance Structures and Materials III, Edited by: C.A. Brebbia, WIT Press, Southampton-Boston*, pp. 653-661.

Rao, J. S. and Gupta, K. (1987), Free vibrations of rotating small aspect ratio pretwisted blades, *Mechanics and Machine Theory*, Vol. 22, No. 2, pp. 159-167.

Rao, S. R. and Ganesan, N. (1997), Dynamic response of non-uniform composite beams, *Journal of Sound and Vibration*, Vol. 200, No. 5, pp. 563-577.

Rao, S. S and Sunar, M. (1999), Recent advances in sensing and control of flexible structures via piezoelectric material technology, *Applied Mechanics Review*, Vol. 52, pp. 1–16.

Ray, M. C. (1998), Optimal control of laminated plate with piezoelectric sensor and actuator layers, *American Institute of Aeronautics and Astronautics Journal*, Vol. 36, No. 12, pp. 2204-2208.

Reddy, J. N., (1999), On laminated composite plates with integrated sensors and actuators, *Engineering Structures*, Vol. 21, pp. 568-593.

Rehfield, L. W., Atilgan, A. R. and Hodges, D. H. (1990), Nonclassical behavior of thin-walled composite beams with closed cross sections, *Journal of the American Helicopter Society*, Vol. 35, pp. 42-50.

Rosen, A. (1991), Structural and dynamic behavior of pretwisted rods and beams, *ASME Applied Mechanics Review*, Vol. 44, No. 12, pp. 483–515.

Sabuncu, M. (1985), Coupled vibration analysis of blades with angular pretwist of cubic distribution, *American Institute of Aeronautics and Astronautics Journal*, Vol. 23, No. 9, pp. 1424-1430.

Shete, C. D., Chandiramani, N. K. and Librescu, L. I. (2007), Optimal control of a pretwisted shearable smart composite rotating beam, *Acta Mechanica*, Vol. 191, pp. 37-58.

Shi, G. and Lam, K. Y. (1999), Finite element vibration analysis of composite beams based on higher-order beam theory, *Journal of Sound and Vibration*, Vol. 219, No. 4, pp. 707-721.

Smith, E. C. and Chopra, I. (1993), Aeroelastic response, loads and stability of a composite rotor in forward flight, *American Institute of Aeronautics and Astronautics Journal*, Vol. 31, No. 7, pp. 1265–1273.

Song, O. and Librescu, L. I. (1997), Structural modeling and free vibration analysis of rotating composite thin-walled beams, *Journal of the American Helicopter Society*, Vol. 42, No. 4, pp. 358-369.

Song, O., Jeong, N. H. and Librescu, L. I. (2000), Vibration and stability of pretwisted spinning thin-walled composite beams featuring bending-bending elastic coupling, *Journal of Sound and Vibration*, Vol. 237, No. 3, pp. 513-533.

Song, O., Kwon, H. D. and Librescu, L. I. (2001), Modeling, vibration and stability of elastically tailored composite thin-walled beams carrying a spinning tip rotor, *Journal of Acoustical Society of America*, Vol. 110, No. 2, pp. 877-885.

Song, O., Librescu, L. I. and Oh, S. Y. (2001), Vibration of pretwisted Adaptive rotating blades modeled as anisotropic thin-walled beams, *American Institute of Aeronautics and Astronautics Journal*, Vol. 39, No. 2, pp. 285-295.

Stemple, A. D. and Lee, S. W. (1988), A finite element model for composite beams with arbitrary cross-sectional warping, *American Institute of Aeronautics and Astronautics Journal*, Vol. 26, No. 12, pp. 619-627.

Subrahmanyam, K. B. (1982), Coupled bending-bending vibrations of pretwisted tapered cantilever beams treated by the reissner method, *Journal of Sound and Vibration*, Vol. 82, No. 4, pp. 577-592.

Subrahmanyam, K. B. and Kaza, K. R. V. (1985), Finite difference analysis of torsional vibrations of pretwisted, rotating, cantilever beams with effects of warping, *Journal of Sound and Vibration*, Vol. 99, No. 2, pp. 213-224.

Suresh, J. K. and Nagaraj, V. T. (1996), Higher-order shear deformation theory for thin-walled composite beams, *Journal of Aircraft*, Vol. 33, No. 5, pp. 978-986.

Swaminathan, M. and Rao, J. S. (1977), Vibrations of rotating, pretwisted and tapered blades, *Mechanism and Machine Theory*, Vol. 12, pp. 331-33.

Trindade, M. A., Benjeddou, A. and Ohayon, R. (2001), Piezoelectric active vibration control of damped sandwich beams, *Journal of Sound and Vibration*, Vol. 246(4), pp. 653-677.

Vasques, C. M. A. and Rodrigues, D. J. (2006), Active vibration control of smart piezoelectric beams: Comparison of classical and optimal feedback control strategies, *Computers and Structures*, Vol. 84, pp. 1402-1414.

Vidoli, S. and Vestroni, F. (2005), Veering phenomena in systems with gyroscopic coupling, *Journal of Applied Mechanics*, Vol. 72, pp. 641-647.

Vinod, K. G., Gopalakrishnan, S. and Ganguli, R. (2006), Wave propagation characteristics of rotating uniform Euler-Bernoulli beams, *Computer Modeling in Engineering and Science*, Vol. 16, No. 3, pp. 197-208.

Vinod, K. G., Gopalakrishnan, S. and Ganguli, R. (2007), Free vibration and wave propogation analysis of uniform and tapered rotating beams using spectrally formulated finite elements, *International Journal of Solids and Structures*, Vol. 44, pp. 5875-5893.

Wang, D. A. and Huang, Y. M. (2002), Modal space vibration control of a beam by using the feedforward and feedback control loops, *International Journal of Mechanical Sciences*, Vol. 44, pp. 01-19.

Wang, Q. and Wang, C. M. (2000), Optimal placement and size of piezoelectric patches on beams from the controllability perspective, *Smart Materials and Structures*, Vol. 9, pp. 558-567.

Wilkie, W. K., Belvin, W. K. and Park, K. C. (1996), Aeroelastic analysis of helicopter rotor blades incorporating anisotropic piezoelectric twist actuation. *Proceedings of ASME 1996 World Congress and Exposition, Adaptive Structures Symposium, November.*

Wilkie, W. K. and Park, K. C. (1996), An aeroelastic analysis of helicopter rotor blades incorporating piezoelectric fiber composite twist actuation. *NASA TM-110252, ARL-MR-328, May – 96.*

Wilkie, W. K., Park, K. C., and Belvin, W. K. (1998), Helicopter dynamic stall suppression using piezoelectric active fiber composite rotor blades, *American Institute of Aeronautics and Astronautics 98-2002,* pp. 2458-2472.

Wu, X. X. and Sun, C. T. (1992), Simplified theory for composite thin-walled beams, *American Institute of Aeronautics and Astronautics Journal,* Vol. 30, No. 12, pp. 2945-2951.

Yang, J. B., Jiang, L. J. and Chen, D. CH. (2004), Dynamic modeling and control of a rotating Euler-Bernoulli beam, *Journal of Sound and Vibration,* Vol. 274, pp. 863-875.

Yang, Y., Jin, Z. and Soh, C. K. (2005), Integrated optimal design of vibration control system for smart beams using genetic algorithms, *Journal of Sound and Vibration,* Vol. 282, pp. 1293-1307.

Yang, S. M. and Lee, Y. J. (1993), Vibration suppression with optimal sensor\actuator location and feedback gain, *Smart Materials and Structures*, Vol. 2, pp. 232-239.

Yildirim, V. and Kiral, E. (2000), Investigation of the rotary inertia and shear deformation effects on the out-of plane bending and torsional natural frequencies of laminated beams, *Composite Structures*, Vol. 49, pp. 313-320.

Yokoyama T. (1988), Free vibration characteristics of rotating Timoshenko beams, *International Journal of Mechanical Science*, Vol. 30, No. 10, pp. 743-755.

Yoo, H. H., Kwak, J. Y. and Chung, J. (2001a), Vibration analysis of rotating pre-twisted blades with a concentrated mass, *Journal of Sound and Vibration*, Vol. 240,No. 5, pp. 891-908.

Yoo, H. H., Lee, S. H. and Shin, S. H. (2005), Flapwise bending vibration analysis of rotating multi-layered composite beams, *Journal of Sound and Vibration*, Vol. 286, No. 4-5, pp. 745-761.

Yoo, H. H., Park, J. H. and Park, J. (2001b), Vibration analysis of rotating pre-twisted blades, *Computers and Structures*, Vol. 79, pp. 1811-1819.

Yoo, H. H., Ryan, R. R. and Scott, R. A. (1995), Dynamics of flexible beams undergoing overall motions, *Journal of Sound and Vibration*, Vol. 181, No. 2, pp. 261-278.

List of Publications

International Journals

1. Vadiraja D. N. and A. D. Sahasrabudhe, (2009) "Vibration and control of rotating tapered thin-walled composite beam using macro fiber composite actuator", *CMES: Computer Modeling in Engineering & Sciences,* Vol. 27, No. 1, pp. 49-62.

2. Vadiraja D. N. and A. D. Sahasrabudhe, "Optimal placement of MFC sensors and actuators on rotating composite cantilever beams using genetic algorithms", Provisionally accepted by the *International Journal of Modelling, Identification and Control*.

3. Vadiraja D. N. and A. D. Sahasrabudhe, (2009) "Vibration analysis and optimal control of rotating pre-twisted thin-walled beams using MFC actuators and sensors", *Thin Walled Structures,* Vol. 47, No. 5, pp. 555 – 567.

International Conference Proceedings

1. Vadiraja D. N. and A. D. Sahasrabudhe, "Vibration analysis of rotating tapered thin-walled composite cantilever beams including gyroscopic coupling", *Proceedings of 2nd International Congress on Computational Mechanics and Simulation, Dec 2006, IIT Guwahati.*

2. Vadiraja D. N. and A. D. Sahasrabudhe, "Free and forced vibration analysis of higher shear deformable rotating thin-walled composite cantilever beams using FEM", *Proceedings of International Conference on Computer Aided Engineering, Dec 2007,IIT Chennai.*

3. Vadiraja D. N. and A. D. Sahasrabudhe, "Optimal control of rotating cantilever beam using MFC actuators and sensors", *Proceedings of International Conference on Theoretical, Applied, Computational and Experimental Mechanics, Dec 2007,IIT Kharagpur.*

4. Vadiraja D. N. and A. D. Sahasrabudhe, "Comparison of optimal control performances of PVDF and MFC actuators in rotating composite beams", *IISc Centenary – International Conference on Advances in Mechanical Engineering* (*IC-ICAME*), *July 2008, Bangalore.*